PERFORMANCE OF RANS MODELS FOR SIMULATING TURBULENT SWIRLING AND FREE JET FLOWS

BY

Keivan Khademi Shamami

A Thesis
Presented to the Faculty of Graduate Studies
In Partial Fulfillment of the Requirements for the Degree of

MASTER OF SCIENCE

Department of Mechanical and Manufacturing Engineering
University of Manitoba
Winnipeg, Manitoba

© Keivan Khademi Shamami, 2008

THE UNIVERSITY OF MANITOBA

FACULTY OF GRADUATE STUDIES

*****

COPYRIGHT PERMISSION

PERFORMANCE OF RANS MODELS FOR SIMULATING TURBULENT SWIRLING AND FREE JET FLOWS

BY

Keivan Khademi Shamami

A Thesis/Practicum submitted to the Faculty of Graduate Studies of The University of Manitoba in partial fulfillment of the requirement of the degree

MASTER OF SCIENCE

Keivan Khademi Shamami © 2008

Permission has been granted to the University of Manitoba Libraries to lend a copy of this thesis/practicum, to Library and Archives Canada (LAC) to lend a copy of this thesis/practicum, and to LAC's agent (UMI/ProQuest) to microfilm, sell copies and to publish an abstract of this thesis/practicum.

This reproduction or copy of this thesis has been made available by authority of the copyright owner solely for the purpose of private study and research, and may only be reproduced and copied as permitted by copyright laws or with express written authorization from the copyright owner.

ABSTRACT

The present work aims at assessing the performances of RANS turbulence models for simulating turbulent swirling and free jet flows, using the commercial software FLUENT version 6.1.22. The RANS turbulence models examined are grouped into two families: (*i*) the two-equation eddy-viscosity models, which are the *k-ε*, *RNG k-ε*, *realizable k-ε*, and the *SST k-ω*, and (*ii*) the Reynolds stress models, which are the standard *RSM* and the *SSG*.

The first flow case simulated in this thesis is a turbulent swirling flow in a can-combustor, in which two inlet swirl intensities (i.e. S=0.4 and S=0.81) are considered. The predictions compared against published experimental data revealed that the eddy-viscosity models are unable to capture the central recirculation zone in the case of the weakly swirling flow (S=0.4). However, although they revealed the existence of this feature for the strongly swirling flow (S=0.81), they were incapable of predicting its correct size. On the other hand, the Reynolds stress models were able to predict the corner and the central recirculation zones for both swirl intensities. The predictions of turbulence intensities by using the *realizable k-ε* and the *SST k-ω* were comparable to those of the Reynolds stress closures. The shear stresses were not well predicted by all the tested models. Both the eddy-viscosity and the Reynolds stress closures showed relatively less approximation errors in the weakly swirling flow.

The second flow case examined is a turbulent free jet issuing from a sharp-edged equilateral triangular orifice in still air surrounding. The numerical simulations revealed that among the eddy-viscosity models, the performance of the *realizable k-ε* model is comparable to that of the Reynolds stress models with the exception of the predictions of

the turbulence intensities. The vena contracta effect was predicted by all the tested models. The *k-ε* and the *RNG k-ε* models showed faster and slower mixing than that of the experiment, respectively. On the other hand, the Reynolds stress models, especially the standard *RSM*, appeared to produce better predictions than the eddy-viscosity models. However, the standard *RSM* seemed unable to capture accurately enough the flatness of the streamwise velocity profiles (top-hat profile) near the centreline in the near-field.

The third and last flow case examined in the present thesis is a turbulent free jet issuing from a circular nozzle with a triangular collar. In this exercise, only the standard *RSM* and the standard *k-ε* model are employed. This is because the trends seen in the combustor and the triangular orifice studies suggested that in these geometries the standard *RSM* has the potential of producing results that agree remarkably well with experimental data. Whereas the standard *k-ε* model is used as a simple representative of the two-equation eddy-viscosity models. This flow case, a circular nozzle which is connected to a triangular collar with a step, may be regarded as a combination of the previous geometries. This is because it encompasses both confinement and sudden expansion. The predictions revealed that the standard *RSM*, which requires more computational time than does the standard *k-ε* model, is capable of reproducing remarkably well the experimental results.

ACKNOWLEDGEMENTS

I would like to thank all of those without whom the completion of this thesis would have not been possible. First of all, I would like to express my deep appreciation for my advisor, Dr. Madjid Birouk, for his continued invaluable guidance, advice and support throughout the M.Sc. program. I would like to greatly acknowledge the financial support for this research by Manitoba Hydro, Project Monitor Mr. Nick Read. I would also like to thank the committee members, Dr. Scott Ormiston, professor of mechanical engineering, and Dr. Behzad Kordi, professor of electrical and computer engineering, for their efforts in reviewing this thesis and providing useful comments.

Lastly but certainly not least, I would like to thank my parents, Heidar and Beizadeh, my sisters, Mitra and Manijeh, and my friend, Asfia Gulrukh Kamal, for their continued support.

TABLE OF CONTENTS

LIST OF TABLES

LIST OF FIGURES

NOMENCLATURE

$\alpha_0, \alpha_1, \alpha_\infty, \alpha^*_\infty$	*SST* k-ω model constants
A	surface area
b_{ij}	Reynolds stress anisotropic tensor
B_e	geometric mean of the jet half-velocity widths
C_1, C_2	Reynolds stress models constants
C_3, C_4, C_5	*SSG* model constants
C_1^*, C_3^*	*SSG* model constants
C_1', C_2'	standard Reynolds stress model constants
$C_{1\varepsilon}, C_{2\varepsilon}, C_\mu$	k-ε based models constants and Reynolds stress models constants
D	diameter of the combustor
D_e	equivalent diameter
D_{ij}	diffusion term of Reynolds stress transport equation
E	empirical constant in non-equilibrium wall function
H	step height
k	turbulence kinetic energy
k_p	turbulence kinetic energy at point p
l	turbulence length scale
L_c	length of the equilateral triangular collar
M_{t0}	*SST* k-ω model constant
P	pressure
P_{ij}	production term of Reynolds stress transport equation
R	radius of the circular nozzle
Re	Reynolds number
$R_{1/2,min}$	jet half-velocity width in the planes of minimum step-height in triangular collar
$R_{1/2,max}$	jet half-velocity width in the planes of maximum step-height in triangular collar
R_β	*SST* k-ω model constant
S	swirl number ($S = \int_0^R UWr^2 dr \,/\, \int_0^R RU^2 r dr$)
S_{ij}	mean rate of strain tensor
u'_i, u'_j, u'_k	velocity fluctuation components
$\overline{u'_i u'_j}$	Reynolds stresses
U_{cl}	streamwise mean velocity on the jet centerline
U_e	streamwise mean velocity on the jet centerline at the circular nozzle exit
U_i, U_j, U_k	mean velocity components
U_{max}	maximum of the streamwise mean velocity on the jet centerline
U_o	mean axial velocity upstream of the swirler
U_{ref}	mean axial velocity on the centerline at the inlet
U_τ	friction velocity
x	axial distance to the orifice exit plane
y, z	lateral distances from jet centerline

y_v	dimensional thickness of the viscous sublayer
$Y_{1/2}$	jet half-velocity width in the central *x-y* plane; triangular orifice
$Z_{1/2}$	jet half-velocity width in the central *x-z* plane; triangular orifice

Greek Letters

Ω_{ij}	mean vorticity tensor
$\beta_{i,1}, \beta_{i,2}, \beta^*_\infty$	*SST* k-ω model constants
δ_{ij}	Kronecker operator
κ	von Karman constant (= 0.4187)
ε	rate of dissipation of k
ε_{ij}	dissipation term of Reynolds stress transport equation
Φ_{ij}	pressure strain term of Reynolds stress transport equation
$\phi_{ij,1}$	return-to-isotropy term in the pressure-strain term (Φ_{ij})
$\phi_{ij,2}$	rapid pressure-strain term in the pressure-strain term (Φ_{ij})
$\phi_{ij,w}$	wall-reflection term in the pressure-strain term (Φ_{ij})
μ	dynamic viscosity
μ_t	eddy viscosity
ρ	density
ς^*	*SST* k-ω model constant
σ_k, σ_ε	k-ε based models constants and Reynolds stress models constants
$\sigma_{k,1}$, $\sigma_{k,2}$	*SST* k-ω model constants
$\sigma_{\omega,1}$, $\sigma_{\omega,2}$	*SST* k-ω model constants
τ_w	wall shear stress
ν	kinematic viscosity
ω	specific dissipation rate

Acronyms

CRR	central reverse flow region
CRZ	corner recirculation zone
CTRZ	central toroidal recirculation zone
DNS	direct numerical simulation
KEM	standard k-ε model
LDV	laser Doppler velocimeter
RANS	Reynods-averaged Navier-Stokes
RKEM	realizable k-ε model
RNG	*RNG* (renormalization group) k-ε model
RSM	Reynolds stress model
SSG	quadratic Reynolds stress model (quadratic pressure-strain model)
SST	shear-stress transport (*SST*) k-ω model

Chapter 1

LITERATURE REVIEW

1.1 Introduction

Turbulent jet flows have several engineering applications, such as in the combustion chamber of a gas turbine and an industrial burner. To improve the performance of such power systems, an accurate insight into the flow structure is required. Physical experimentation can be difficult and costly due to the complexity of the jet flow's enclosure. Therefore, numerical simulations of these flows are attractive alternatives. Although several numerical approaches are available, the simplest and cheapest is the one based on RANS closures. However, the accuracy of these numerical approaches depends very much on the reliability of turbulence closure models. The turbulence closure models are needed to model the turbulent stress terms in the mathematical equations that describe the flow dynamics.

In the present work the performances of RANS turbulence models are assessed for simulating turbulent flows in three different flow situations. The first case study concerns a swirling jet in a gas turbine's can-combustor, the second and third flow situations are simply a turbulent free jet issuing from a triangular orifice, and from a circular pipe with a triangular collar, respectively.

The turbulence RANS models tested here are grouped under two categories:

(*i*) The two-equation eddy-viscosity models:

- The standard k-ε model
- The *RNG* k-ε model
- The *realizable* k-ε model

- The *SST* k-ω model

(*ii*) The Reynolds stress models:

- The standard *RSM* model
- The *SSG* model.

A review of the pertinent literature is reported below for each flow situation.

1.2 Turbulent Swirling Flow in a Confined Geometry with a Sudden Expansion

Swirling flows are used in a wide variety of engineering applications, such as furnaces and gas turbine combustors. The use of swirl in these power systems has several benefits. It is recognized that a swirling flow produces an adverse pressure gradient that can cause flow reversal or vortex breakdown. The swirling flow's central recirculation zone may result in decreasing pollutants emission by bringing hot species back to the combustion zone as well as lowering the possibility of flame blow-off. Moreover, swirl causes further mixing between the fuel and the oxidant which improves the overall combustor performance.

Numerous studies have been reported on the mathematical calculations of swirling flows in a combustor. It is shown that the standard k-ε model [1-2] and its different versions (e.g. Refs. [3-5]) which can perform reasonably well for simulating simple turbulent flows, appear inadequate for simulating swirling flows [6-28]. Using different versions of the k-ε turbulence model, Hogg et *al.* [6], Jones et *al.* [7], Sharif et *al.* [8], Chen et *al.* [9], Yaras et *al.* [10], and Yang et *al.* [11], carried out numerical simulation of a highly swirling flow (S=2.25) in a cylindrical combustor characterized experimentaly by So et *al.* [29]. It is reported that the k-ε model exhibits an excessive level of turbulent diffusion and its predictions for the mean flowfield of the studied case are not satisfactory

[29]. The deficiency of the k-ε model in predicting the turbulent diffusion is well recognized in the simulation of other swirling flows in different combustor geometries and in a wide range of swirl numbers [12-28, 30]. For example, Tsao et *al.* [28] simulated a can-type gas turbine combustor for two swirl numbers (S=0.74, and 0.85) and showed that the k-ε model predicted a relatively higher level of deceleration of the axial velocity in the centerline region of the combustor which is a sign of excessive diffusion and hence higher level of swirl entrainment. However, later versions of the k-ε model showed improvement over the standard k-ε model in predicting the characteristics of swirling flows but still less accurate as compared to experimental data [16, 19, 26, 31-34]. The persistent deficiency of these models is believed to be a result of their use of isotropic eddy-viscosity concept, while the structure of turbulent swirling flows is mostly anisotropic [35]. In addition, the eddy-viscosity models have difficulties in accounting properly for turbulence-swirl interactions. For instance, the *RNG* k-ε model [36] has been employed to simulate several configurations of confined swirling flows [16, 19, 37]. It is well-known that the *RNG* k-ε and the standard k-ε differ mainly in the expression of the dissipation rate (ε) equation. In the *RNG* k-ε model a new term is introduced into the dissipation rate (ε) equation which results in an apparent success of this version of k-ε models in predicting the length of recirculation zones of several separating flows [37-39]. However, in some cases predictions of the *RNG* k-ε and the k-ε are not much different. For example, Xia et *al.* [19] examined both the standard k-ε and the *RNG* k-ε models for predicting a strongly swirling flow (S=1.68) in a water model combustion chamber, and found that both of the models gave fairly accurate results near the inlet region but failed to reproduce accurately the downstream flow characteristics, although the *RNG* k-ε model

was found to make a slightly improved prediction near the flow inlet. A major weakness of the standard k-ε model or other traditional k-ε models, such as *RNG* k-ε model, lies in their way of modeling the dissipation rate (ε) equation. The *realizable* k-ε model [40] is intended to address the deficiencies of these k-ε models by introducing a new eddy-viscosity formula and a new dissipation equation that is based on the dynamic equation of the mean-square vorticity fluctuation [40-41]. Zhu et al. [16] employed the standard k-ε, the *RNG* k-ε, and the *realizable* k-ε model in the simulation of coflow jets in a cylindrical combustor. They found that the *realizable* k-ε model worked better than did the standard k-ε model, while the *RNG* k-ε model did not give improvements over the standard k-ε model. In the shear-stress transport (*SST*) k-ω model [42], the definition of the turbulent viscosity is re-defined along with the addition of a cross-diffusion term in the ω-equation. These modifications of the *SST* k-ω model show better performance over both the standard k-ε and *RNG* k-ε models [41-42]. Nonetheless, it has been reported that the *SST* k-ω model yields excessive radial diffusive transport in both upstream and downstream of a strongly swirling flow [10]. Engdar et *al.* [21] investigated the performance of the standard k-ε model and the *SST* k-ω model in the simulation of a confined swirling flow. They found that in a swirling flow with S=0.58, the standard k-ε model was not able to predict the central recirculation zone, while the *SST* k-ω model showed this region.

Other turbulence closure models, such as algebraic Reynolds stress model (*ASM*), have been used for simulating swirling turbulent flows [8, 13, 20, 25, 43-46]. It has been shown [44-45] that the *ASM* is not able to simulate properly axisymmetric swirling flows, because of significant stress transport processes present in this type of flows. However, new modified versions of the *ASM* have been employed to simulate several swirling flow configurations [13, 20, 25, 45-46], which appear to produce better predictions over the standard k-ε model. Zhang et *al.* [46] simulated a confined coaxial swirling jet using a new *ASM* and compared their results with those obtained via the k-ε model. They reported that the mean and fluctuating velocities predicted by the *ASM* were superior to those of the k-ε model. The k-ε model was reported to be incapable of showing the central reverse flow, while the *ASM* revealed the existence of this region [46].

The standard Reynolds stress model (*RSM*) [47], and its different versions have also been tested for several swirling flow configurations and satisfactory predictions has been achieved [6-9, 13, 17-19, 23, 28, 48-53]. However, the *RSM* model has been found incapable of resolving all the deficiencies of the two-equation models for simulating turbulent swirling flows [7-8, 17-18, 48-50, 54-56]. For example, Tsai et *al.* [18] found that for a weakly swirling flow (S=0.3) the k-ε model predicted a faster axial velocity recovery, while the *RSM* model showed a relatively slow axial velocity development, though the stress closure (*RSM*) performed better in general. It has also been reported that the intensity of turbulence is underpredicted by the stress model along the centerline [18, 49-50]. Hanjalic [39, 57] reported that both the equations for the dissipation rate of k and the pressure-strain term were the main source of inaccuracy in predicting turbulence quantities. Modified versions of the *RSM* have been proposed [50, 58-59]. For example, Lumley et *al.* [58] modeled the source term of the transport ε-equation in a new way. However, their work is not very helpful in simulating complex swirling flows [50]. Speziale et *al.* [59] proposed a new quadratic model for the pressure-strain term (*SSG*) which appears to produce accurate results of various types of flows [9, 50-51, 60-61]. For example, Chen et *al.* [9] employed the *SSG* model in simulating confined swirling flows

(S=0.85, and 2.25) and reported that the *SSG* model predicted the flow adequately in both of the cases. Lu et *al.* [50] introduced a modified source term of the transport ε-equation based on physical reasoning in that anisotropy is responsible for the turbulent transfer from large- to small-scale eddies in regions of predominantly anisotropic turbulence, and that isotropy controls the turbulent kinetic energy transfer in flow regions where turbulence is predominantly isotropic. They found that their new ε-equation together with the *SSG* model exhibited a strong improvement in the prediction of a weakly (S=0.5) swirling flow. It has also been reported that the *SSG* model performed well in the vicinity of a wall, in spite of the fact that its formulation does not contain wall-reflection correction terms [50].

The literature reviewed above show that confined swirling flows have been studied experimentally and numerically. Mainly, the confinement is either a dump (can) combustor or a straight pipe (cylinder). It has been demonstrated experimentally that the inlet swirl intensity can alter significantly the swirling flow field characteristics [12, 62]. It can, for example, drastically change the position and size of different regions of the flow, e.g. the central toroidal recirculation zone (CTRZ) and the corner recirculation zone (CRZ) [11-12, 17, 62-66]. In a dump combustor, the CRZ always exists, whereas the CTRZ may not occur at low inlet swirl intensities. On the other hand, in a straight pipe (cylinder), the CRZ does not exist; however, the CTRZ may occur at high swirl intensities. Therefore, both the inlet swirl intensity and type of confinement geometry have an impact on the overall characteristics of a swirling flowfield. It has also been shown that the swirler design (inlet velocity profile) can change the flowfield of a combustor [62]. Although there are numerous studies in which some of RANS models are employed to simulate swirling flows with different inlet swirl intensities (e.g. Ref. [50]: S=0.5, S=2.25), a comprehensive parametric study that enables examining the performance of these numerical models appears to be lacking. For example, two different geometries (i.e. a straight pipe and a dump combustor) have been used in [50], but for each geometry only one single inlet swirl intensity was tested. In addition, the swirler design (inlet swirling flow profile) was also different in both geometries. For instance, the corner recirculation zone does exist only in the dump combustor geometry. Moreover, in some other numerical works (such as Ref. [14]) although it is claimed that only the inlet swirl intensity is varied, the literature shows that either the inlet swirl intensity range is not wide enough to alter the main features of the flow field or there is a lack of comprehensive comparative examinations of the performance of different RANS models. Another issue that arises while reviewing the literature is the fact that some of the two-equation models (i.e. *RNG* k-ε, *realizable* k-ε, and *SST* k-ω) have been rarely tested in predicting the mean and turbulence quantities of swirling flows in a can-combustor with different inlet swirl numbers.

Therefore, the numerical simulation of this flow case attempts to provide a comprehensive assessment of the performance of the most recognized RANS turbulence models for predicting the main characteristics of a can-combustor swirling flow with different inlet swirl intensities (i.e. S=0.4 and S=0.81). In contrast to published studies, only the swirl intensity is varied in the present work, as both the swirler design and combustor geometry are kept the same. The adopted two inlet swirl intensities are thought to be representative of the weak and strong swirling flow characteristics. Also, it is important to note that the choice of this particular geometry is driven by the fact that the experimental data are readily available for various inlet swirl numbers [63, 67], and also due to its industrial pertinence.

1.3 Turbulent Free Jet Issuing From an Equilateral Triangular Orifice

Jets issuing from non-circular nozzles have advantages over conventional axisymmetric ones. The use of nozzles with triangular, rectangular, and square shape in combustion systems has several benefits. For example, these types of nozzles promote large-scale mixing, which enhances bulk mixing of reactants, and small-scale mixing at molecular level to initiate the chemical reactions. Therefore, passive mixing enhancement can be accomplished by using asymmetric fuel nozzles. It has been shown that these types of nozzles (or orifices) generate large-scale mixing at the flat sides of the nozzle and small-scale mixing at the corners [68-70].

A review of the up to date literature revealed that numerous experimental studies have been performed on jets issuing from non-circular nozzles or orifices with sharp edges, e.g. [68-103]. However, numerical works are not as many. Rectangular and square jets have received most of the attention [104-125], while only very few numerical studies have been devoted to triangular jets [104, 124-125]. Gutmark et al. [126] reviewed published studies of non-circular jets up to 1997, and Quinn [68-69] reported a short review of the experimental and numerical works on triangular jets up to 2005.

Miller et al. [104] used direct numerical simulation to study three-dimensional jets issuing from circular and non-circular nozzles of identical equivalent diameters at a Reynolds number of 800, based on the nozzle equivalent diameter and the difference between the co-flowing free stream velocity and the jet exit velocity. Their study included elliptic, square, rectangular, equilateral triangular and isosceles triangular nozzles. They reported that the triangular jets showed markedly different characteristics than the other jets. It has been found that coherent large scale structures are quickly masked by the small scale structures formed at the corners [104]. It was reported that all the non-circular jets promote more efficient mixing than does a circular jet. The isosceles triangular nozzle was found to be the most efficient [104], however, these numerical results lacked experimental verification.

Abdel-Hameed et al. [124] also performed direct numerical simulations to study the characteristics of three-dimensional, laminar free jets issuing from different inlet geometric configurations; circular, elliptic, rectangular, square, and triangular. In their simulation, both single-phase and two-phase flows were considered, however, only the laminar regime was examined. For both single-phase and two-phase flows, it was shown that the square geometry appeared to enhance only marginally the entrainment rate compared with the circular one. On the other hand, the rectangular, elliptic, and triangular jets exhibited substantial enhancement in entrainment. It is also reported that the triangular jet displayed the largest fine-scale production at the vertices.

Imine et al. [125] investigated numerically the effects of jet's geometry on the process of mixing, in which rectangular, elliptic and triangular nozzles with an aspect ratio of 1.33 were considered. A second-order Reynolds stress model was used to investigate the flowfield of asymmetric turbulent free jets. It is reported that the asymmetric geometries enhanced the mixing in comparison with the axisymmetric counterpart. The rectangular jet showed the fastest centerline streamwise mean velocity decay rate, followed by the elliptic and the triangular jet. However, their numerical examination lacked experimental validation.

The literature reviewed above shows that there is a lack of a three-dimensional numerical simulation of a turbulent free jet issuing from a triangular orifice. Therefore, the aim of the present study is to provide an analysis of the performance of the most familiar *RANS* turbulence closure models for predicting the main characteristics of a turbulent free jet issuing from a sharp-edged equilateral triangular orifice. The predictions are compared with their experimental counterparts, as reported in chapter 4.

1.4 Turbulent Free Jet Issuing From a Pipe with a Triangular Collar

A review of the literature revealed that *passive* control methods different than those shown in the previous section aimed at increasing mixing and spreading of a jet have recently been reported. For example, a *lobed* nozzle which is a more complex asymmetric geometry was examined for its potential to stretch the mixing layer exposed to the ambient so that more entrainment would take place [80, 85, 116, 127-128]. Also, *tabs*, which are small protrusions placed at the nozzle exit, were investigated to assess their ability to produce counter-rotating streamwise vortex pairs [80, 84-85, 112, 115-116, 129-133]. It was reported that these vortex pairs can have a significant impact on jet spreading [116]. A recently proposed passive method for increasing jet mixing and spreading is by using a *collar* which is a sudden expansion of the nozzle [134-137]. Therefore, by changing the collar expansion-ratio and its length, various flow phenomena can be generated.

Husain et al. [134] studied an elliptic whistler (i.e. self-excited) air jet with an aspect ratio of 2:1 which, in contrast to an elliptic jet issuing from a contoured nozzle, displays no axis switching, but significantly increases jet spreading in the major-axis plane. It was reported in this study that the vortices roll up from the lip of the elliptic pipe and impinge onto the collar, producing secondary vortices. It was shown that the near-field mass entrainment was considerably higher (by as much as 70%) than that of a non-whistling jet.

A triangular orifice jet with collars of expansion-ratios ranging between 2.1 and 3.5 was studied by Lee et al. [135]. Their experimental set-up consisted of a triangular inlet orifice expanding into a short axisymmetric chamber with an exit lip. It was shown that maximum spreading angle and maximum decay rate increased with the expansion ratio of the orifice.

Mi et al. [136] studied a rectangular orifice jet with a square collar. They found that while the jet spreading and entrainment rates increased, the absolute volume of entrained fluid was lower due to the confining effects of the collar. They also reported that the increased turbulence intensities persisted even in the far-field region.

New et al. [137] examined collared-jets with relatively small expansion-ratios. They studied the influence of non-circular collars on an axisymmetric jet. In their experimental work, circular, square, and triangular collars with expansion ratios of 1.20, 1.35, and 1.54, respectively, with collar lengths of up to two jet diameters were tested. They reported that a pair of counter-rotating vortex-pairs on each side of the collar wall was formed in the square and triangular collars. It was shown that to achieve a maximum centerline velocity decay, the circular collar required the shortest collar length, followed by square and triangular collars. The triangular collar produced the widest overall jet-spread.

To the best knowledge of the author, there is no three-dimensional numerical simulation of collared-jets that employs turbulence RANS closures to solve the flow's governing equations. In the present work, the jet flow of a pipe with a triangular collar measured by New et al. [137] is simulated numerically. Results are reported only for the standard *RSM* and the standard k-ε model.

Chapter 2

MATHEMATICAL FORMULATION

2.1 Governing Equations

The mass and momentum Reynolds-averaged equations for a turbulent steady-state flow can be written in tensor notation as follows

$$\frac{\partial(\rho U_i)}{\partial x_i} = 0 \tag{2.1}$$

$$\frac{\partial(\rho U_i U_j)}{\partial x_j} = -\frac{\partial P}{\partial x_i} + \frac{\partial}{\partial x_i}\left(\mu \frac{\partial U_i}{\partial x_j} - \rho \overline{u_i u_j}\right) \tag{2.2}$$

The time-averaged values of the velocity fluctuating tensors, $\overline{u_i u_j}$, in Eq. (2.2) are unknown. They are generally identified as Reynolds stresses. These equations contain other correlations of higher order which have to be modeled in order to close the system of Reynolds-averaged equations (i.e. Eq. (2.2)). Therefore, a solution of Eqs. (2.1) and (2.2) for a turbulent flow can be obtained only by introducing additional equations for the Reynolds stresses. The turbulence closure models employed in the present work are summarized briefly below.

2.2 Two-Equation Eddy-Viscosity Models

2.2.1 The *k*-ε Model

In the k-ε model, the Reynolds stresses are linearly related to the mean rate of strain by a scalar eddy viscosity as follows [138]

$$-\rho \overline{u_i u_j} = 2\mu_t S_{ij} - \frac{2}{3}\rho k \delta_{ij} \tag{2.3}$$

where S_{ij} and μ_t are the mean rate of strain tensor and the eddy viscosity which are given, respectively, as

$$S_{ij} = \frac{1}{2}\left(\frac{\partial U_i}{\partial x_j} + \frac{\partial U_j}{\partial x_i}\right) \tag{2.4}$$

$$\mu_t = C_\mu \rho \frac{k^2}{\varepsilon} \tag{2.5}$$

where k and ε are the turbulent kinetic energy and dissipation rate, respectively, which are expressed as

$$k = \frac{1}{2}\overline{u_i u_i} \tag{2.6}$$

$$\varepsilon = \nu \overline{\frac{\partial u_i}{\partial x_j}\frac{\partial u_i}{\partial x_j}} \tag{2.7}$$

The k-ε model (referred to as *KEM* in the present study), consists of two transport equations, i.e. for k and ε, respectively, which are given as follows

$$\frac{\partial(\rho U_j k)}{\partial x_j} = \frac{\partial}{\partial x_j}\left((\mu + \frac{\mu_t}{\sigma_k})\frac{\partial k}{\partial x_j}\right) + 2\mu_t S_{ij} S_{ij} - \rho\varepsilon \tag{2.8}$$

$$\frac{\partial(\rho U_j \varepsilon)}{\partial x_j} = \frac{\partial}{\partial x_j}\left((\mu + \frac{\mu_t}{\sigma_\varepsilon})\frac{\partial \varepsilon}{\partial x_j}\right) + 2C_{1\varepsilon}\frac{\varepsilon}{k}\mu_t S_{ij} S_{ij} - C_{2\varepsilon}\rho\frac{\varepsilon^2}{k} \tag{2.9}$$

The model constants, which are summarized in Table 2.1, are determined from experiments for homogeneous shear flows and isotropic grid turbulence [1].

Table 2.1: k-ε based models coefficients

	C_μ	$C_{1\varepsilon}$	$C_{2\varepsilon}$	σ_k	σ_ε
KEM	0.09	1.44	1.92	1	1.3
RNG	0.0845	1.42	1.68	0.7179	0.7179
RKEM	-	1.44	1.9	1	1.2

2.2.2 The *RNG k-ε* Model

The *RNG*-based k-ε model (referred to as *RNG* in the present study), is derived by using a mathematical technique called "renormalization group" (*RNG*) method [139]. It has a similar form to the *KEM*. The model constants, which are summarized in Table 2.1, are obtained analytically [36]. It is shown that in regions of weak to moderate strain rate, the *RNG* model yields results comparable to the standard *k*-ε model [41]. On the other hand, in regions of large strain rate the *RNG* model shows a lower turbulent viscosity than the standard *k*-ε model. Therefore, the *RNG* model is more responsive to the effects of rapid strain and streamline curvature than the standard *k*-ε model [41]. A more comprehensive description of the *RNG* can be found in [41, 140].

2.2.3 The *realizable k-ε* Model

The *realizable k*-ε model (referred to as *RKEM* in the present study), which is proposed by Shih et *al.* [40] has a new eddy viscosity equation with a variable C_μ, as well as a new dissipation equation. The *k*-equation in the *RKEM* model has the same form as that in the *KEM* and *RNG* models; however, the ε-equation is different, which is given as

$$\frac{\partial(\rho\varepsilon)}{\partial t}+\frac{\partial(\rho U_j\varepsilon)}{\partial x_j}=\frac{\partial}{\partial x_j}\left((\mu+\frac{\mu_t}{\sigma_\varepsilon})\frac{\partial\varepsilon}{\partial x_j}\right)+\rho C_1 S\varepsilon-\rho C_2\frac{\varepsilon^2}{k+\sqrt{\varepsilon\upsilon}}+C_{1\varepsilon}\frac{\varepsilon}{k}C_{3\varepsilon}G_b \quad (2.10)$$

where:

$$C_1=\max\left[0.43,\frac{\eta}{\eta+5}\right] \quad , \quad \eta=S\frac{k}{\varepsilon} \quad , \quad S=\sqrt{2S_{ij}S_{ij}} \quad (2.11)$$

Similarly to the *KEM*, the turbulent viscosity is computed using Eq. (2.5), however, C_μ is not a constant and is calculated using the following equation

$$C_\mu=\frac{1}{A_0+A_s(kU^*/\varepsilon)} \quad (2.12)$$

where:

$$U^*=\sqrt{S_{ij}S_{ij}+\vec{\Omega}_{ij}\vec{\Omega}_{ij}} \quad (2.13)$$

$$\vec{\Omega}_{ij}=\Omega_{ij}-2\varepsilon_{ijk}\omega_k\,, \quad \Omega_{ij}=\frac{1}{2}\left(\frac{\partial\bar{u}_i}{\partial x_j}-\frac{\partial\bar{u}_j}{\partial x_i}\right) \quad (2.14)$$

$$A_0 = \text{Constant}, \quad A_s = \sqrt{6}\cos\phi \tag{2.15}$$

$$\phi = \frac{1}{3}\cos^{-1}(\sqrt{6}W), \quad W = \frac{S_{ij}S_{jk}S_{ki}}{\vec{S}^3}, \quad \vec{S} = \sqrt{S_{ij}S_{ij}} \tag{2.16}$$

In contrast to the standard *k-ε* model and the *RNG k-ε* model, the *realizable k-ε* model satisfies certain mathematical constraints for the normal stresses which are consistent with the physics of turbulent flows [41]. The model constants are given in Table 2.1.

2.2.4 The *SST k-ω* Model

The shear-stress transport *k-ω* model (referred to as *SST* in the present study), which is developed by Menter [42], is a modification of the standard *k-ω* model where the equation for the turbulent viscosity is modified to account for the transport of the principal turbulent shear stress [41].

The *SST* model consists of the following transport equations for the turbulence kinetic energy, *k*, and the specific dissipation rate, *ω*

$$\frac{\partial(\rho U_i k)}{\partial x_i} = \frac{\partial}{\partial x_j}\left((\mu + \frac{\mu_t}{\sigma_k})\frac{\partial k}{\partial x_j}\right) + \overline{G}_k - Y_k \tag{2.17}$$

$$\frac{\partial(\rho U_i \omega)}{\partial x_i} = \frac{\partial}{\partial x_j}\left((\mu + \frac{\mu_t}{\sigma_\omega})\frac{\partial \omega}{\partial x_j}\right) + \overline{G}_\omega - Y_\omega + D_\omega \tag{2.18}$$

where the turbulent viscosity, μ_t, is computed as follows

$$\mu_t = \frac{\rho k}{\omega}\frac{1}{\max[\frac{1}{\alpha^*}, \frac{SF_2}{a_1\omega}]} \tag{2.19}$$

The turbulent Prandtl numbers for k and ω, σ_k and σ_ω, are given as

$$\sigma_k = \frac{1}{F_1/\sigma_{k,1} + (1-F_1)/\sigma_{k,2}} \tag{2.20}$$

$$\sigma_\omega = \frac{1}{F_1/\sigma_{\omega,1} + (1-F_1)/\sigma_{\omega,2}} \tag{2.21}$$

The coefficient α^* damps the turbulent viscosity causing a low-Reynolds-number correction and is given as [41]

$$\alpha^* = \alpha^*_\infty \left(\frac{\alpha^*_0 + \mathrm{Re}_t / R_k}{1 + \mathrm{Re}_t / R_k} \right) \tag{2.22}$$

where

$$\mathrm{Re}_t = \frac{\rho k}{\mu \omega}, \quad R_k = 6, \quad \alpha^*_0 = \frac{\beta_i}{3}, \quad \beta_i = 0.072 \tag{2.23}$$

The functions F_1 and F_2 in Eqs. (2.19)-(2.21) are given by

$$F_1 = \tanh(\phi_1^4), \quad \phi_1 = \min\left[\max\left(\frac{\sqrt{k}}{0.09\omega y}, \frac{500\mu}{\rho y^2 \omega} \right), \frac{4\rho k}{\sigma_{\omega,2} D^+_\omega y^2} \right] \tag{2.24}$$

$$F_2 = \tanh(\phi_2^2), \quad \phi_2 = \max\left(2\frac{\sqrt{k}}{0.09\omega y}, \frac{500\mu}{\rho y^2 \omega} \right) \tag{2.25}$$

$$D^+_\omega = \max\left[2\rho \frac{1}{\sigma_{\omega,2}} \frac{1}{\omega} \frac{\partial k}{\partial x_j} \frac{\partial \omega}{\partial x_j}, 10^{-10} \right] \tag{2.26}$$

where y is the distance to the next surface and D^+_ω is the positive portion of the cross-diffusion term, D_ω, which is defined as

$$D_\omega = 2(1-F_1)\rho \sigma_{\omega,2} \frac{1}{\omega} \frac{\partial k}{\partial x_j} \frac{\partial \omega}{\partial x_j} \tag{2.27}$$

The terms $\overline{G}_k$, $\overline{G}_\omega$ in Eqs. (2.17) and (2.18) represent the production of k and ω, respectively, and are given by

$$\overline{G}_k = \min(G_k, 10\rho\beta^* k\omega), \quad \overline{G}_\omega = \frac{\alpha_\infty}{\nu_t} G_k \tag{2.28}$$

where

$$G_k = \mu_t S^2, \quad \alpha_\infty = F_1 \alpha_{\infty,1} + (1-F_1)\alpha_{\infty,2} \tag{2.29}$$

$$\alpha_{\infty,1}=\frac{\beta_{i,1}}{\beta_{\infty}^{*}}-\frac{\kappa^{2}}{\sigma_{w,1}\sqrt{\beta_{\infty}^{*}}},\quad \alpha_{\infty,2}=\frac{\beta_{i,2}}{\beta_{\infty}^{*}}-\frac{\kappa^{2}}{\sigma_{w,2}\sqrt{\beta_{\infty}^{*}}} \tag{2.30}$$

and $\kappa=0.41$. The terms Y_k and Y_ω in Eqs. (2.17) and (2.18) are the dissipation of k and ω, respectively, and are given by

$$Y_k=\rho\beta^{*}k\omega,\quad Y_\omega=\rho\beta_i\omega^{2} \tag{2.31}$$

$$\beta_i=F_1\beta_{i,1}+(1-F_1)\beta_{i,2} \tag{2.32}$$

where $\beta_{i,1}$ and $\beta_{i,2}$ are constants and F_1 is obtained by Eq. (2.24). The model constants are tabulated in Table 2.2 [141].

Table 2.2: *SST k-ω* model coefficients

α^{*}_{∞}	α_{∞}	α_0	α_1	R_β	ς^{*}	M_{t0}	β^{*}_{∞}	$\beta_{i,1}$	$\beta_{i,2}$	$\sigma_{k,1}$	$\sigma_{k,2}$	$\sigma_{\omega,1}$	$\sigma_{\omega,2}$
1.0	0.52	1/9	0.31	8.0	1.5	0.25	0.09	0.075	0.0828	1.176	1.0	2.0	1.168

2.3 Reynolds Stress Models

2.3.1 The Standard *RSM* Model

The Reynolds stresses are calculated from their transport equations [47]. Closure for Reynolds stresses require six equations for the six independent Reynolds stresses, $\overline{u_iu_j}$, and another equation for the isotropic turbulence energy dissipation rate, ε. The Reynolds stress transport equations are expressed as

$$\frac{\partial}{\partial t}(\rho\overline{u_iu_j})+\frac{\partial}{\partial x_k}(\rho U_k\overline{u_iu_j})=D_{ij}+P_{ij}+\phi_{ij}-\varepsilon_{ij} \tag{2.33}$$

where D_{ij}, P_{ij}, ϕ_{ij} and ε_{ij} represent, respectively, the diffusion, production, pressure-strain, and viscous dissipation.

The diffusion term can be modeled by the generalized gradient-diffusion model of Daly and Harlow [142]

$$D_{ij} = C_s \frac{\partial}{\partial x_k}\left(\rho \frac{k\overline{u_k u_l}}{\varepsilon} \frac{\partial \overline{u_i u_j}}{\partial x_l} \right) \tag{2.34}$$

It should be noted that in the present study, instead of using the generalized gradient-diffusion model of Daly and Harlow [142] for the D_{ij} term, the simplified model equation, which is reported in [143], is used. It is expressed as

$$D_{ij} = \frac{\partial}{\partial x_k}\left(\frac{\mu_t}{\sigma_k} \frac{\partial \overline{u_i u_j}}{\partial x_k} \right) \tag{2.35}$$

where μ_t, the turbulent viscosity, is defined as in Eq. (2.5);

P_{ij} is the stress production term which is given as

$$P_{ij} = -\rho \overline{u_i u_k} \frac{\partial U_j}{\partial x_k} - \rho \overline{u_j u_k} \frac{\partial U_i}{\partial x_k} \tag{2.36}$$

ε_{ij} is the stress dissipation term which is given as

$$\varepsilon_{ij} = -\frac{2}{3} \rho \delta_{ij} \varepsilon \tag{2.37}$$

The pressure-strain term has been modeled by Gibson and Launder [144], Fu et al. [145], and Launder [146-147] using the following three-term model

$$\phi_{ij} = \phi_{ij,1} + \phi_{ij,2} + \phi_{ij,w} \tag{2.38}$$

where $\phi_{ij,1}$ is the *return-to-isotropy* term, $\phi_{ij,2}$ is the *rapid pressure-strain* term, and $\phi_{ij,w}$ is the *wall-reflection* term. The three components of the pressure-strain term are modeled as

$$\phi_{ij,1} = -C_1 \rho \frac{\varepsilon}{k}\left[\overline{u_i u_j} - \frac{2}{3}\delta_{ij} k \right] \tag{2.39}$$

$$\phi_{ij,2} = -C_2 \left[(P_{ij} - C_{ij}) - \frac{1}{3}\delta_{ij}(P_{kk} - C_{kk}) \right] \tag{2.40}$$

$$\phi_{ij,w} = C_1' \frac{\varepsilon}{k}\left[\overline{u_k u_m} n_k n_m \delta_{ij} - \frac{3}{2}\overline{u_i u_k} n_j n_k - \frac{3}{2}\overline{u_j u_k} n_i n_k\right]\frac{k^{3/2}}{C_l \varepsilon d}$$
$$+ C_2'\left[\phi_{km,2} n_k n_m \delta_{ij} - \frac{3}{2}\phi_{ik,2} n_j n_k - \frac{3}{2}\phi_{jk,2} n_i n_k\right]\frac{k^{3/2}}{C_l \varepsilon d} \tag{2.41}$$

where

$$P_{ij} = -\rho\overline{u_i u_k}\frac{\partial U_j}{\partial x_k} - \rho\overline{u_j u_k}\frac{\partial U_i}{\partial x_k}, \quad C_{ij} = \frac{\partial \rho U_k \overline{u_i u_j}}{\partial x_k} \tag{2.42}$$

and n_k is the x_k component of the unit normal to the wall, d is the normal distance to the wall, $C_l = C_\mu^{3/4}/\kappa$, and κ is the von Karman constant (= 0.4187). The turbulence energy dissipation rate, ε, is obtained by solving the transport equation shown below. The model constants are provided in Table 2.3.

$$\frac{\partial(\rho\varepsilon)}{\partial t} + \frac{\partial(\rho\varepsilon U_i)}{\partial x_i} = \frac{\partial}{\partial x_j}\left[(\mu + \frac{\mu_t}{\sigma_\varepsilon})\frac{\partial \varepsilon}{\partial x_j}\right] + \frac{1}{2}C_{\varepsilon 1}\frac{\varepsilon}{k}P_{ii} - C_{\varepsilon 2}\rho\frac{\varepsilon^2}{k} \tag{2.43}$$

Table 2.3: Reynolds stress models coefficients

	C_μ	C_1	C_1^*	C_2	C_3	C_3^*	C_4	C_5	$C_{1\varepsilon}$	$C_{2\varepsilon}$	C_1'	C_2'	σ_k	σ_ε
RSM	0.09	1.8	-	0.6	-	-	-	-	1.44	1.92	0.5	0.3	1	1.3
SSG	0.09	3.4	1.8	4.2	0.8	1.3	1.25	0.4	1.44	1.83	-	-	1	1.3

2.3.2 The *SSG* Model

The *SSG* model uses a quadratic pressure-strain model instead of a linear pressure-strain model [59]. It is expressed as

$$\phi_{ij} = -(C_1\varepsilon + C_1^* P)b_{ij} + C_2\varepsilon(b_{ik}b_{kj} - \frac{1}{3}b_{mn}b_{mn}\delta_{ij}) + (C_3 - C_3^*\sqrt{b_{ij}b_{ij}})kS_{ij}$$
$$+ C_4 k(b_{ik}S_{jk} + b_{jk}S_{ik} - \frac{2}{3}b_{mn}S_{mn}\delta_{ij}) + C_5 k(b_{ik}\Omega_{jk} + b_{jk}\Omega_{ik}) \tag{2.44}$$

where b_{ij} is the Reynolds stress anisotropy tensor given as

$$b_{ij} = \frac{\overline{u_i u_j}}{2k} - \frac{1}{3}\delta_{ij} \tag{2.45}$$

with S_{ij} and Ω_{ij} are the mean rate of the strain tensor and the mean vorticity tensor, respectively, which are defined as

$$S_{ij} = \frac{1}{2}\left(\frac{\partial u_j}{\partial x_i} + \frac{\partial u_i}{\partial x_j}\right), \quad \Omega_{ij} = \frac{1}{2}\left(\frac{\partial u_i}{\partial x_j} - \frac{\partial u_j}{\partial x_i}\right) \tag{2.46}$$

The model constants are tabulated in Table 2.3.

Chapter 3

TWO-DIMENSIONAL SIMULATION OF A TURBULENT SWIRLING FLOW IN A CONFINED CYLINDER WITH A SUDDEN EXPANSION

3.1 Problem Definition and Solution Procedure

The set of governing equations, which result from Eqs. (2.1) and (2.2), is solved by the aid of the turbulence closure models described in the previous section. Their solution is applied for simulating swirling flows in a can combustor. The geometry of the combustor is shown in Figure 3.1, which is simply a cylinder with sudden expansion.

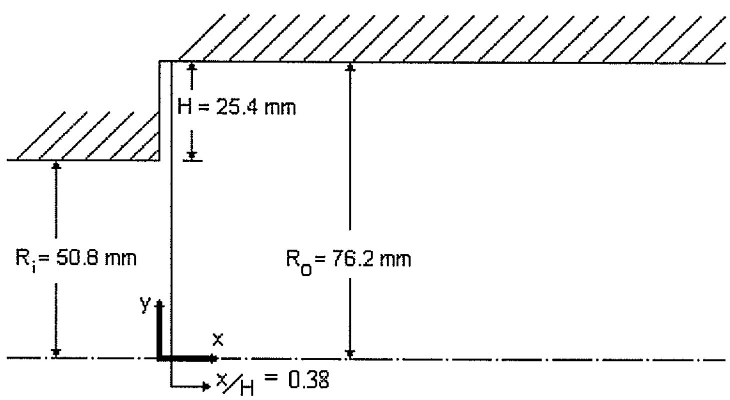

Figure 3.1: Schematic of the combustor geometry

In the present study, two flow configurations are simulated; referred to in the present thesis as flow configuration with low and high swirl numbers, respectively. The first one is airflow with an inlet centerline velocity of 19.2 ± 0.4 m/s, which corresponds to a Reynolds number of 1.25×10^5 based on the combustor inlet diameter (see Fig. 3.1). The swirl number, defined as $S = \int_0^R UWr^2 dr \,/\, \int_0^R RU^2 r dr$, in this configuration is 0.4 [63]. The second configuration is an airflow with an inlet average velocity of 30.4 ± 0.3 m/s, which corresponds to a Reynolds number of 1.98×10^5 based on the combustor inlet diameter. The swirl number in this case is 0.81. Note that the Reynolds and swirl numbers in the second flow configuration are about 1.6 and 2 times those in the first one, respectively, which provide a wide range of flow conditions (see Table 3.1).

Table 3.1: Inlet flow test conditions

	Inlet Centerline velocity	Inlet average velocity	Reynolds number	Swirl number
Case 1	19.2±0.4 m/s	-	1.25×10^5	0.4
Case 2	-	30.4±0.3 m/s	1.98×10^5	0.81

Experimental data for these two flow configurations are obtained from [63, 67]. Note that experimental data are available starting from *x/H=0.38* downstream of the combustion sudden expansion. In the simulation exercise, the experimental data at this location are used as the inlet boundary conditions. The experimental data for the turbulent kinetic energy (k) at the inlet is used in the simulation. In order to calculate the dissipation rate of the turbulent kinetic energy at the inlet, the following equation is used [41]

$$\varepsilon = C_\mu^{3/4} k^{3/2} / l \tag{3.1}$$

where C_μ is a constant (=0.09), k is the turbulent kinetic energy, and l is the turbulence length scale which can be approximated as *0.07D*, where D is the combustor diameter. The flow is assumed steady, axisymmetric and isothermal. Because of the symmetry, only the upper half of the combustor is simulated. The computational domain is chosen to be long enough to ensure complete development of the flow; that is, up to *x/H=18* in the first flow configuration and up to *x/H=24* in the second one. A zero normal-gradient boundary condition is chosen at the outlet. A two-layer-based, non-equilibrium wall function [148] is used near the wall. In this model, the Launder and Spalding's [138] log-law for the mean velocity is sensitized to the effects of pressure-gradient, and it is also assumed that the wall-neighboring cells consist of a viscous sublayer and a fully turbulent layer [41]. Details of the wall function used in the simulation of this flow case are presented in Appendix B. In both flow cases, the wall-adjacent cell's centroid is located at $y^+ \approx 45$.

The numerical mesh in the first flow configuration is chosen to be 64×128 in the axial and radial directions, respectively, while in the second case a mesh of 64×160 is employed. A non-uniform mesh is made finer near the inlet as well as close to both the combustor axis and the wall, whereas a coarser grid is used elsewhere. Grid independency is verified by doubling the number of mesh points in both cases.

To solve the governing equations, the FLUENT code, which is based on finite volume formulation, is employed. The PISO [149] method is applied for the pressure-velocity coupling. QUICK [150] scheme is used for the convection terms in all transport equations, and the PRESTO [41] method is used for the pressure discretization. An overview of the numerical methods used in the present study is provided in Appendix A. The solution convergence is assumed when all of the residuals fall below 5×10^{-6}.

The mean and fluctuating velocity components as well as the Reynolds shear stresses are compared against published measured data. Also, the velocity vectors and streamline contours are plotted for both low and high swirl intensity flow configurations.

3.2 Low Swirl Number Flow Configuration

3.2.1 Mean Velocity Field

Computational results of the normalized axial velocity are compared against their counterpart's published experimental data in Figures 3.2(a) and 3.2(b) at typical planes/stations in the near-, mid- and relatively far-fields of the flow. U_{ref} in these figures is the mean axial velocity on the centerline at the inlet. Three distinct regions can be observed; (*i*) a core region near the centerline of the combustor, (*ii*) a near wall region, and (*iii*) a mixing layer between these two regions. It can be seen that the size of each of these regions varies from one axial plane (or station) to another.

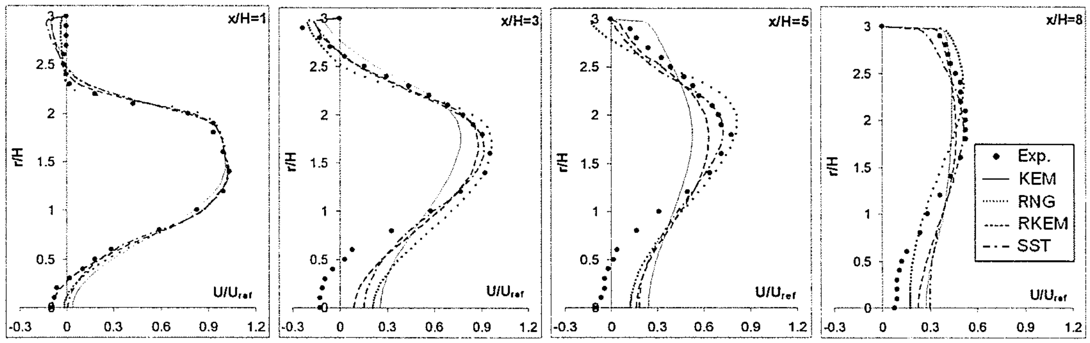

Figure 3.2(a): Radial profiles of normalized axial velocity (S=0.4); Eddy-viscosity models

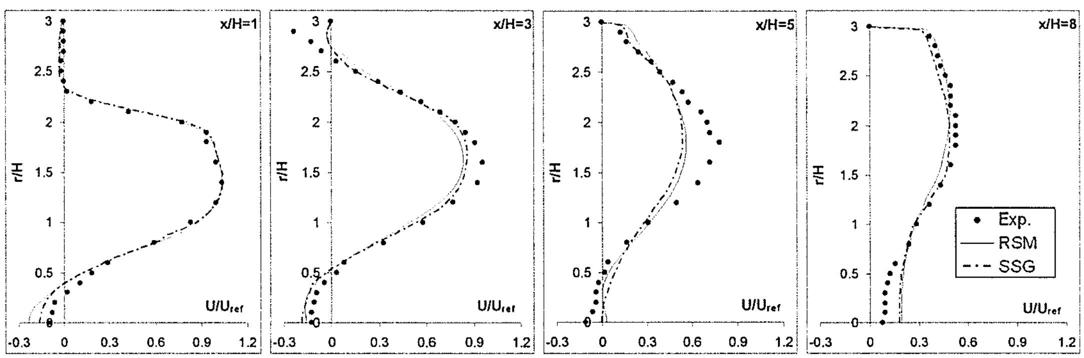

Figure 3.2(b): Radial profiles of normalized axial velocity (S=0.4); Reynolds stress closures

Note that in the experiment [63] a two-component Laser Doppler Velocimeter system has been used to measure the flowfield. It was reported that the maximum uncertainty in the measurement of the mean quantities was 0.4% of the upstream centerline velocity [63]. Figures 3.2(a) and 3.2(b) show that due to the small value of the measurement uncertainty in comparison with the numerical prediction errors, the measurement error can not be assumed to be responsible for the poor numerical predictions. As we can see in Figure 3.2(a), the maximum axial velocity at the inlet station occurs approximately halfway between the centreline (i.e. the axis of symmetry where $y = 0$ in Fig. 3.1) and the wall. However, as the flow progresses axially (downstream), the maximum axial velocity decays and shifts slightly towards the wall of the combustor. For example, at $x/H=1$, the maximum velocity is almost equal to the U_{ref}, which occurs halfway radially (i.e. $r/H \sim 1.5$). However, at $x/H = 8$, the maximum velocity is only $0.5U_{ref}$ and it is shifted towards the wall (i.e. $r/H \sim 2$). More importantly, these figures show clearly that the two-equation models predict a faster recovery of the axial velocity along the centerline. This characteristic of these types of models is also reported by Tsai et *al.* [18] and Lin et *al.* [151]. On the other hand, Figure 3.2(b) indicates that the stress models produce more accurate predictions than their counterparts' two-equation eddy-viscosity models. For instance, in all the axial stations presented in Figure 3.2(a), the two-equation eddy viscosity models predict poorly the axial velocity near the centerline. Whereas, Figure 3.2(b) shows that the Reynolds stress models produce satisfactory predictions (with respect to the experimental data) everywhere including near the centreline. It can be concluded from Figures 3.2(a) and 3.2(b) that the axial mean velocity at low swirl numbers in a cylindrical combustor with sudden expansion can be reasonably predicted by the Reynolds stress models. Among the two-equation eddy-viscosity models, the *SST* model shows adequate predictions except near the axis of symmetry.

Computational results of the normalized tangential velocity are compared against published experimental data, as shown in Figures 3.2(c)-(d), for several axial stations representing the near, mid, and far-fields of the flow development in the combustor.

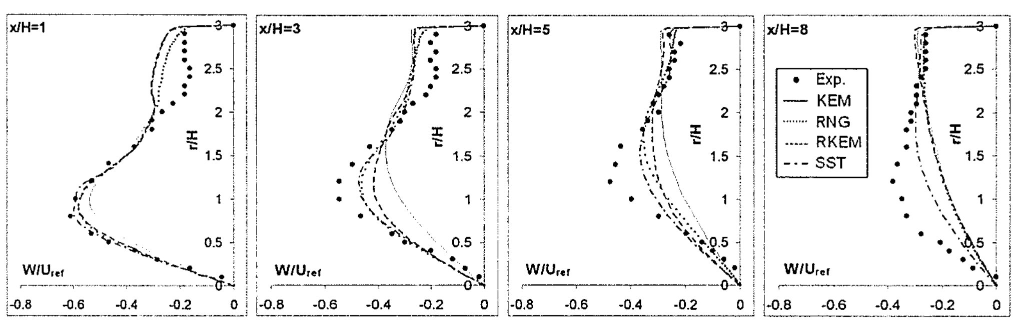

Figure 3.2(c): Radial profiles of normalized swirl velocity (S=0.4); Eddy-viscosity models

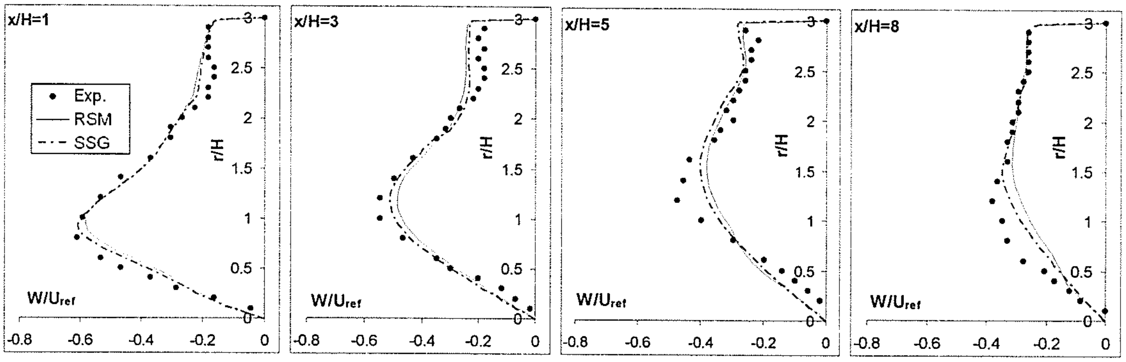

Figure 3.2(d): Radial profiles of normalized swirl velocity (S=0.4); Reynolds stress closures

One can say that the maximum tangential velocity occurs at the first measurement station, which is near the flow onset. At subsequent stations beyond *x/H=10* (not shown in this paper), the swirl profile for all the models becomes relatively flat, which is a characteristic of a tangential velocity profile generated by a constant-angle swirler [63]. Overall, the predictions beyond *x/H~10* are in good agreement with the experimental data of [63]. As can be seen in Figure 3.2(c) at stations close to the dump plane (i.e. *x/H=1*), all the two-equation eddy-viscosity models predict poorly the tangential flow velocity especially near the wall. However as the flow develops downstream the dump plane, the same models do not perform well in the inner flow region (i.e. for *r/H<1.5*). On the other hand, the Reynolds stress models show reasonably satisfactory predictions of the tangential velocity profiles despite the fact that they slightly underpredict the maximum tangential velocity in the region between *r/H=0.5* and *r/H=1.5*. For this weakly swirling flow, *S=0.4*, one may conclude that among the two-equation eddy-viscosity models, the *KEM* and *SST* show the worst and best predictions of the mean swirl velocity profiles, respectively. But the predictions of *SST* are still poor as compared to the experimental data. The predictions of the Reynolds stress models (e.g. *RSM* and *SSG*), on the other hand, are much closer to the experimental data.

3.2.2 Visualization of the Flowfield

The velocity vectors and streamline contours in the *UV* plane at several typical locations representing the near-, mid- and far-fields of the flow development in the combustor are presented in Figures 3.3 and 3.4, respectively.

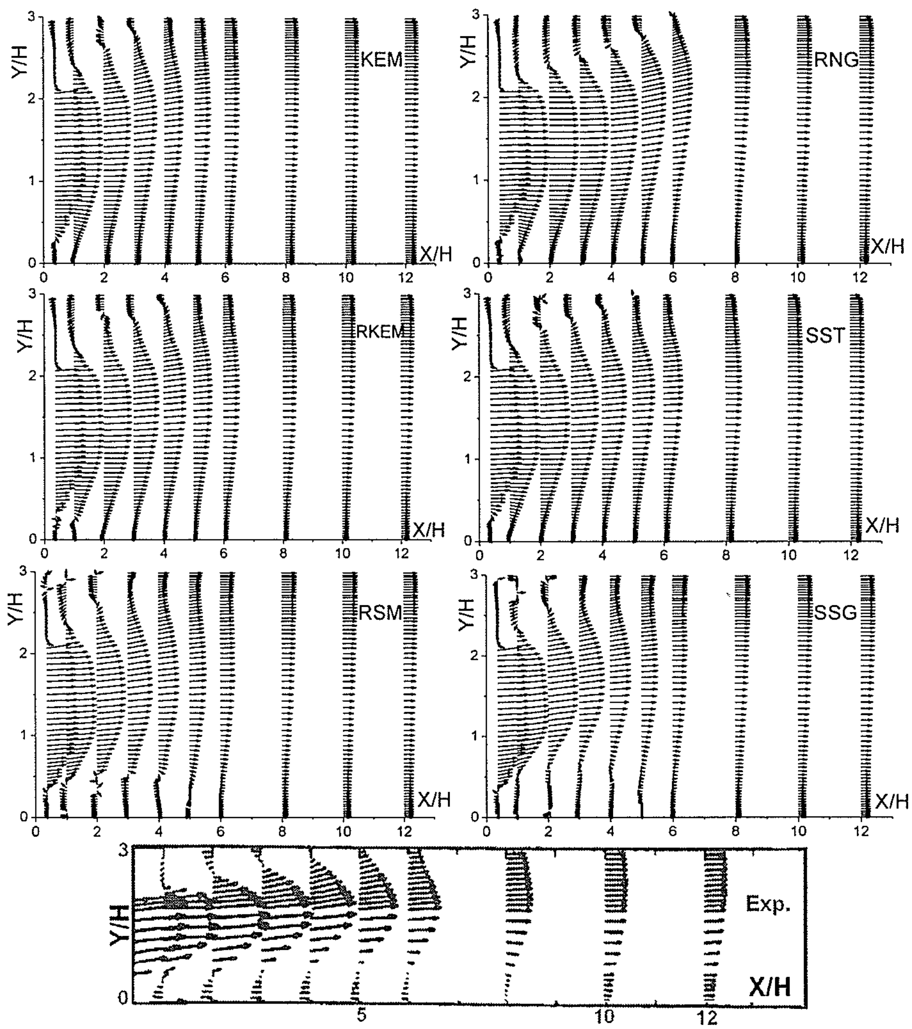

Figure 3.3: Predicted and measured velocity vectors ($S = 0.4$)

The predictions in Figure 3.4 indicate that the flowfield of a turbulent swirling flow in a dump combustor can be characterized by two distinct regions: (*i*) a corner recirculation zone (CRZ) that is caused by the sudden expansion of the cylindrical combustor, and (*ii*) a central toroidal recirculation zone (CTRZ) which is caused by an increase in the swirl intensity of the swirling flow. According to the experimental data [63], the CRZ starts in the dump plane and extends to roughly 4 step heights downstream of the dump plane. Figures 3.3 and 3.4 show that all the tested models are able to predict the CRZ.

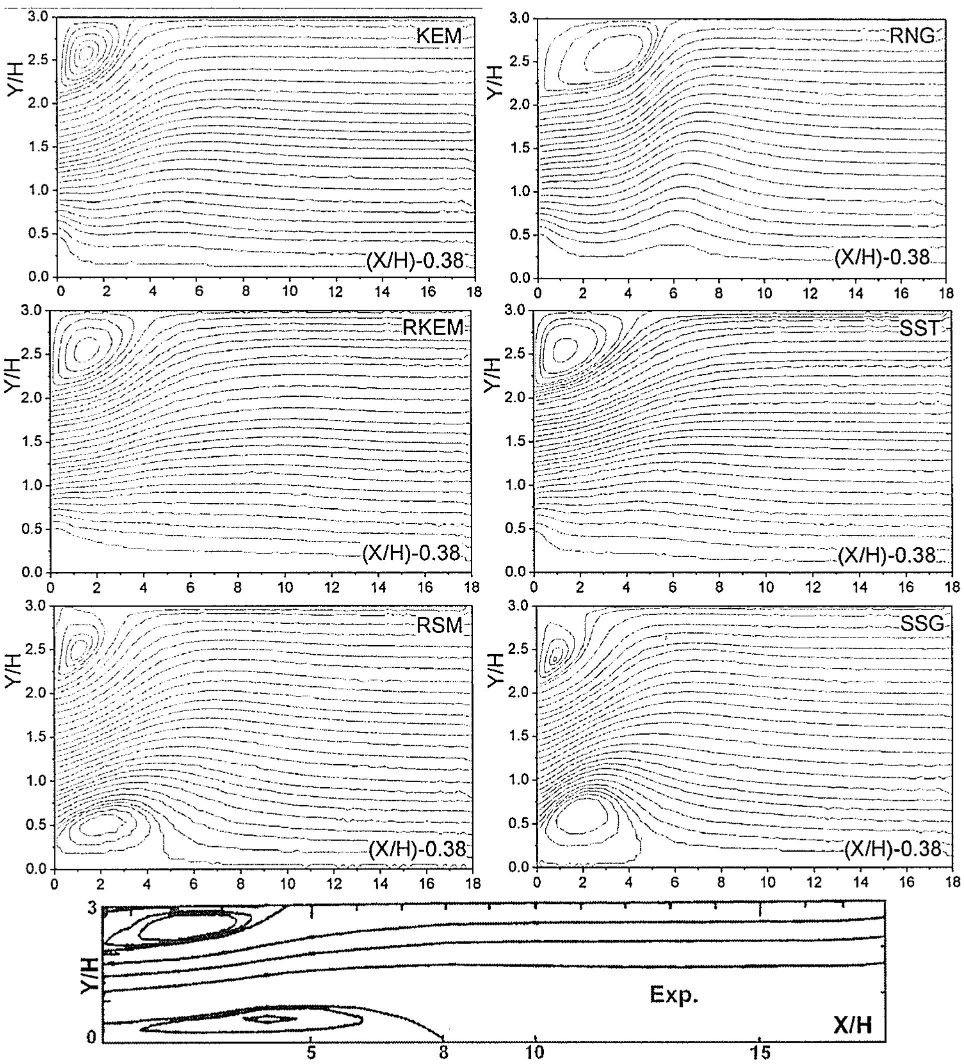

Figure 3.4: Predicted and measured contours of streamline ($S = 0.4$)

The predicted length of the CRZ by these models is summarized in Table 3.2. This Table shows that the predicted length of the CRZ by the *KEM* is the best one when compared with its experimental counterpart. The predicted CRZs by the *RNG*, *RKEM* and the *SST* are longer than the one found experimentally, while the predicted CRZs by the *RSM* and *SSG* are shorter than their experimental counterpart.

Table 3.2: Measured and predicted length of the *CRZ* for $S = 0.4$

	Experiment	KEM	RNG	RKEM	SST	RSM	SSG
$(x/H)_{max}$	4	3.7	6	5	5	2.7	2.5

It is found experimentally that the CTRZ starts in the inlet pipe upstream of the dump plane and extends to roughly 7.9 step heights downstream of the dump plane, with a maximum radius of *r/H=0.6* at *x/H=5.0* [63]. Figures 3.3 and 3.4 show that the *KEM*, *RNG*, *RKEM* and the *SST* cannot predict this important feature of the flow, while the *RSM* and the *SSG* models are able of capturing this feature. The predicted CTRZ by the *RSM* extends to approximately 5 step heights downstream of the dump plane, with a maximum radius of *r/H=0.75* at *x/H=3.5* while that predicted by the *SSG* extends to approximately 5 step heights downstream of the dump plane with a maximum radius of *r/H=0.9* at *x/H=3*. This indicates that both the RSM and the *SSG* predict shorter (in axial direction) and wider (in the radial direction) CTRZ, as compared to the experiments (see Table 3.3).

Table 3.3: Measured and predicted length and width of the *CTRZ* for $S = 0.4$

	Experiment	KEM	RNG	RKEM	SST	RSM	SSG
$(x/H)_{max}$	7.9	-	-	-	-	5	5
$(y/H)_{max}$	0.6	-	-	-	-	0.75	0.9

In conclusion, all the employed turbulence models can predict the CRZ, whereas only the Reynolds stress closures reveal the existence of the CTRZ. The size of the CRZ is reasonably well predicted by the *KEM* model, while the *RSM* model produces slightly smaller CRZ. The *RSM* shows better predictions of the size of the CTRZ than that of the *SSG*, although the predicted size of the CTRZ is still around 40% shorter in length than its experimental counterpart.

3.2.3 Turbulence Quantities

Figures 3.5(a)-(d) show the radial profiles of the measured and predicted turbulence intensity components and two of the Reynolds shear stress components (i.e. $\overline{u'v'}$, and $\overline{u'w'}$) at different axial locations (i.e. near- mid- and far-field).

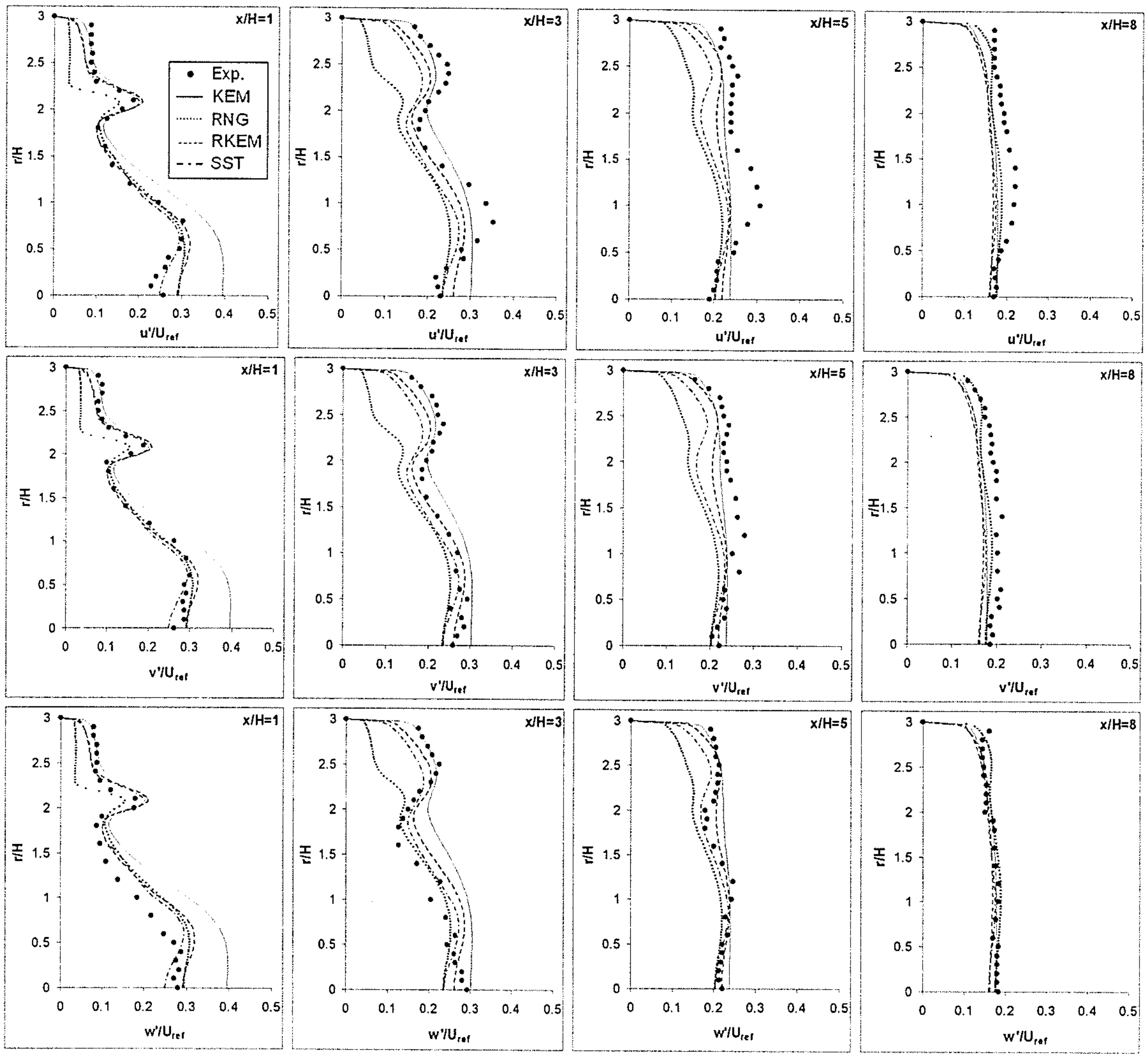

Figure 3.5(a): Radial profiles of normalized turbulence intensities ($S = 0.4$); Eddy-viscosity models

The experimental data of the normalized u' shown in Figures 3.5(a) and 3.5(b) reveal two peaks at each axial location in the near- and mid-field. One peak is located in the shear layer between the main flow and the CTRZ, and the other one can be seen in the shear layer between the main flow and the CRZ. Comparing the values of these two peaks, it can be noted that the turbulent activity in the central shear layer is stronger than the activity in the outer shear layer. This characteristic of the flow is captured by all the models.

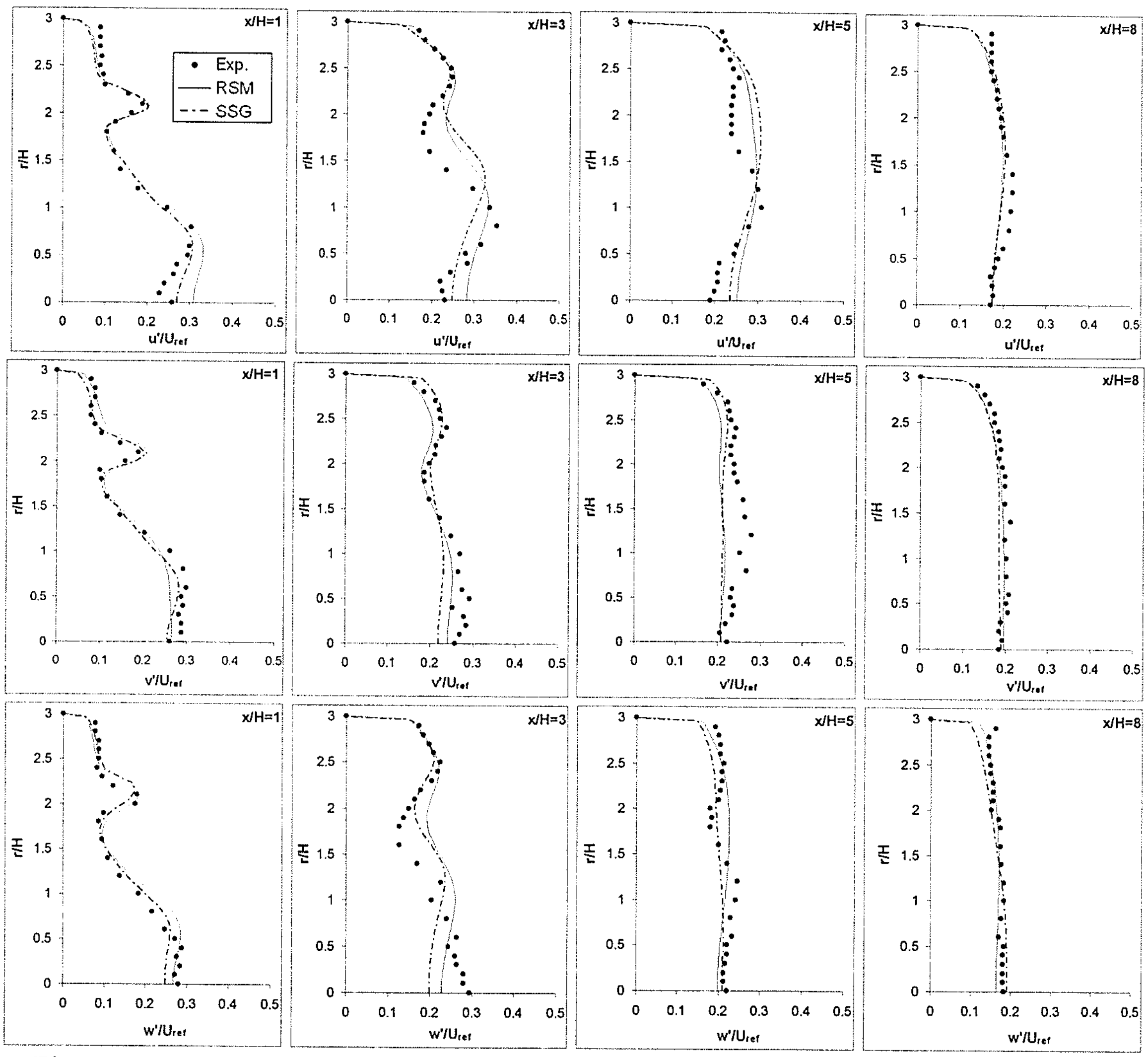

Figure 3.5(b): Radial profiles of normalized turbulence intensities (S=0.4); Reynolds stress closures

The experimental data show a maximum turbulence intensity at $x/H=3$, while all the tested models predict a maximum turbulence intensity at $x/H=1$, except the *SSG* which shows almost the same level of turbulence at $x/H=1$ and $x/H=3$. The *KEM* overpredicts the turbulence intensities in the inner region at *x/H=1*. In the near- and mid-filed, the *RNG* shows very poor results in the region *r/H>2*.

A similar trend is observed for the radial and tangential turbulence intensity profiles. The *KEM* overpredicts v' and w' in the inner region at *x/H=1*, and *x/H=3*, while the *RNG* underpredicts these components of the turbulence intensity in the region *r/H>2* for the near- and mid-field. Between the Reynolds stress closures, the *SSG* performs better at *x/H=1*, while the predictions of *RSM* are competitive with those of the SSG in the mid- and far-field. As reported by other authors [50], the value of v' and w' is under-predicted by the Reynolds stress closures near the centerline in the mid-field. In the far field, all the numerical predictions of the turbulence intensities are in good agreement with the relatively flat experimental trends (profiles). Similar to the numerical results for the mean velocity components, the predictions of the Reynolds stress models for the turbulence intensities are more accurate than those obtained by the eddy-viscosity models.

Profiles of the Reynolds shear stresses presented in Figures 3.5(c) and 3.5(d) show that $\overline{u'v'}$ changes sign across the combustor. The shear stresses in the far-field are insignificant indicating full recovery of the flow inside the combustor. At *x/H=1*, in the region *r/H<1.5*, $\overline{u'v'}$ is overpredicted by a factor of 3 or more by all the eddy-viscosity models, except the *SST*. In the mid-field the *SST* shows good results, especially in the outer region, while the predictions of the *KEM* and the *RKEM* in the far-field are very close to that of the experiment. On the other hand, the Reynolds stress models are in fairly good agreement with the measured $\overline{u'v'}$ data, except at *x/H=3* where they show the same trend as the measured data, but with different magnitude. The second component of the Reynolds shear stresses, $\overline{u'w'}$, shows one peak close to the CTRZ boundary, at *x/H=1* and *x/H=3* after which it rapidly loses its strength and becomes insignificant.

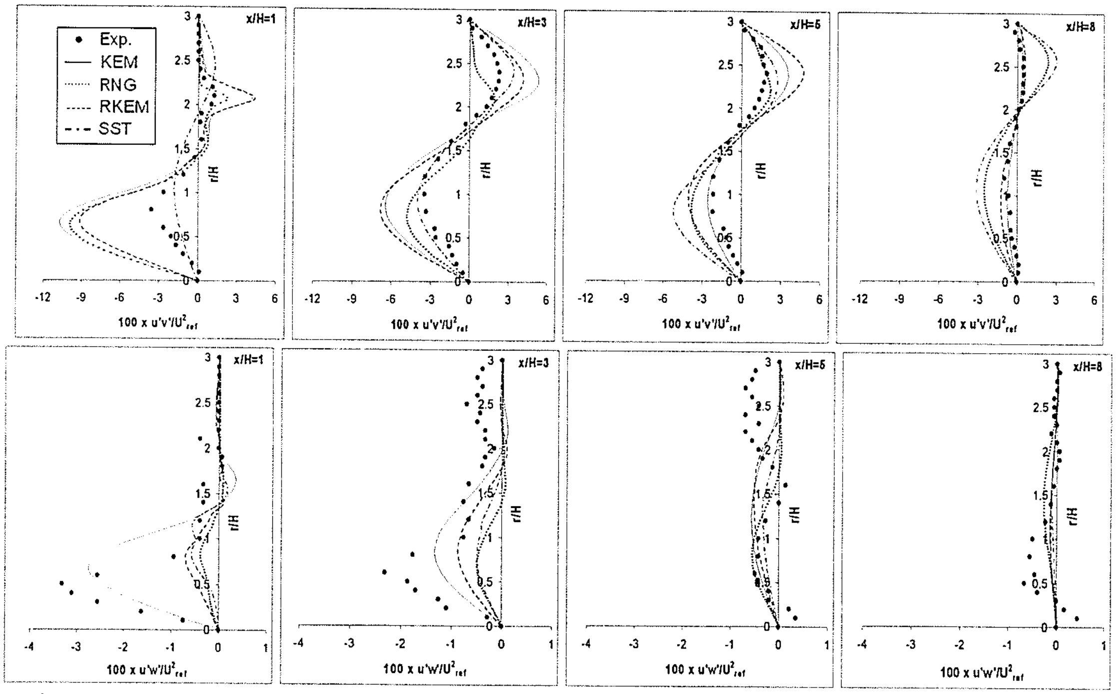

Figure 3.5(c): Radial profiles of normalized shear stresses ($S = 0.4$); Eddy-viscosity models

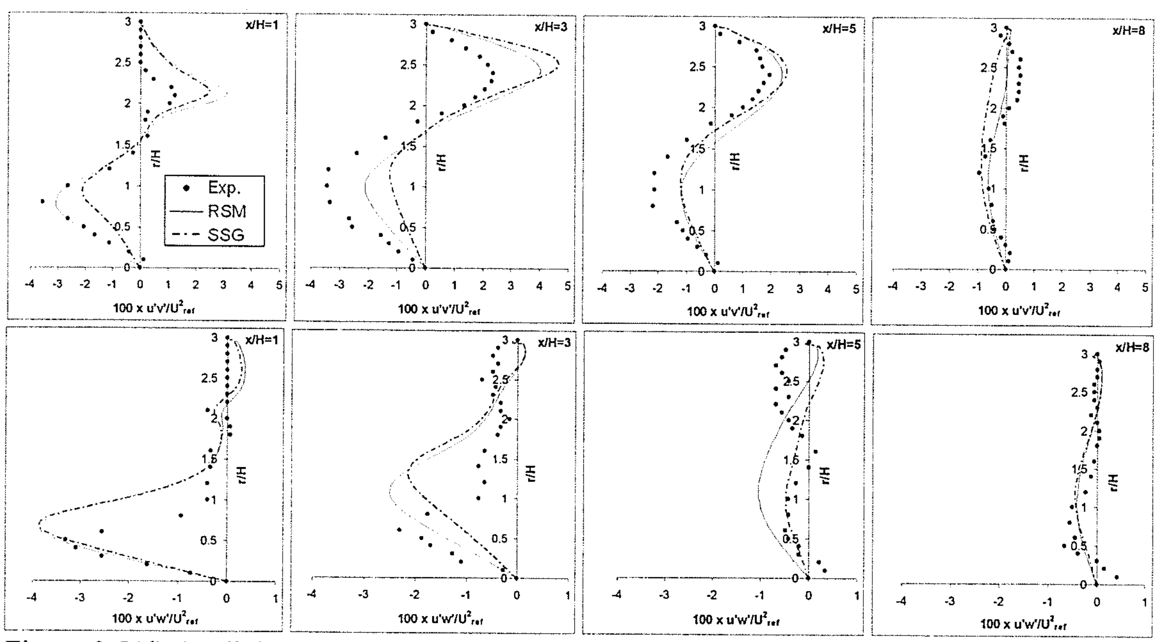

Figure 3.5(d): Radial profiles of normalized shear stresses ($S = 0.4$); Reynolds stress closures

In the near-field, all the eddy viscosity models underpredict $\overline{u'w'}$ by a factor of 5 in the inner region, except the *KEM* which shows much more accurate results. At *x/H=1* there is no visible difference between the Reynolds stress models predictions. At this axial location, the RSM and the *SSG* show accurate enough results except near the wall. In the mid-field, none of the models shows satisfactory results, while in the far-field, the magnitude of $\overline{u'w'}$ is so low that there is not much difference between the predictions and experiments.

In conclusion, among the eddy-viscosity models, the *RKEM* is the best model in predicting the turbulence intensity components, while more accurate results of the Reynolds shear stresses can be obtained by employing the *KEM*. On the other hand, the Reynolds stress closures show superior results in predicting the turbulence flowfield in this case study. The performance of the *RSM* and the *SSG* is competitive.

3.3 High Swirl Number Flow Configuration

3.3.1 Mean Velocity Field

Figures 3.6(a)-(d) present a comparison of the predicted profiles of the normalized axial and tangential velocities with their counterparts' experimental data at typical stations representative of the near-, mid- and far-fields of the flow. U_o in these figures is the mean axial velocity upstream of the swirler.

Similar to the weakly swirling flow, it is clear from Figure 3.6(a) that the evolution size of the three radial regions (i.e. a core area near the axis, a near wall region and a mixing layer in between) of the axial velocity profiles, which varies as the flow develops downstream the onset point, is generally captured by all the two-equation eddy-viscosity models. This figure shows that the maximum axial velocity is located approximately halfway between the centerline and the wall in the near-field, and shifts towards the wall in the mid- and far-fields. In addition, Figure 3.6(a) shows that there are two reverse flow regions that can be seen at *x/H=1*, which is an indication of the existence of the CRZ and the CTRZ. The maximum axial velocity at *x/H=1* is located at *r/H=1.7* according to both the measurements and the stress models predictions.

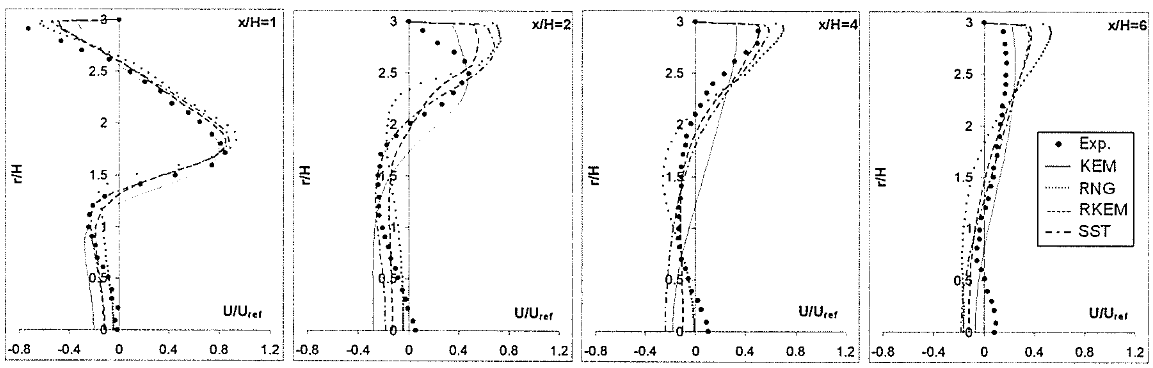

Figure 3.6(a): Radial profiles of normalized axial velocity (*S*=0.81); Eddy-viscosity models

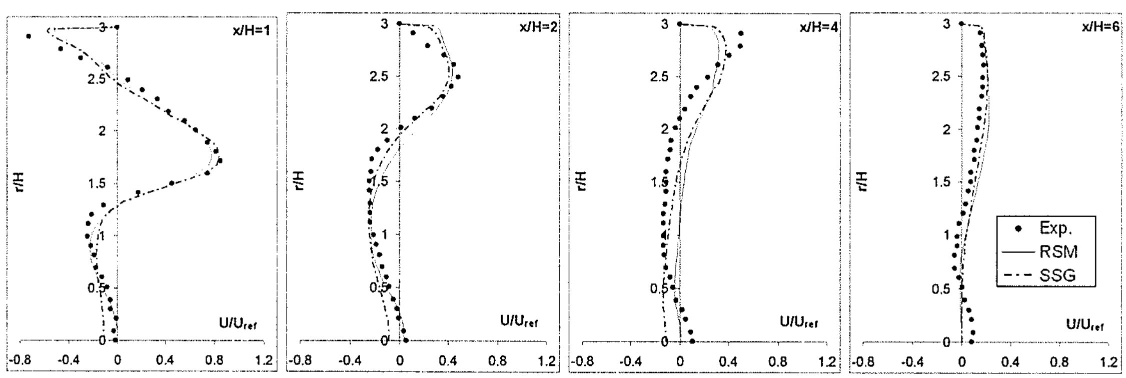

Figure 3.6(b): Radial profiles of normalized axial velocity (*S*=0.81); Reynolds stress closures

In the experiment [67] a two-component Laser Doppler Velocimeter (LDV) system has been used to measure the flowfield. It was reported that the maximum uncertainty in the measurement of the mean quantities was 1.8% of the mean axial velocity upstream of the swirler [67]. Figures 3.6(a) and 3.6(b) show that due to the small value of the measurement uncertainty in comparison with the numerical prediction errors, the measurement error can not be assumed to be responsible for the poor numerical predictions.

All the two-equation eddy-viscosity models underpredict the value of the maximum axial velocity, and only the *KEM* predicts accurately the maximum axial velocity. In the near-field, that is at $x/H=1$, the *KEM* shows the worst results in the core region and the wall region. On the other hand, Figure 3.6(b) shows that the Reynolds stress models produce good agreement with the measurements.

In the mid- and far-field regions, the *RNG* shows poor predictions, especially in predicting the size of the reverse flow regions and the axial velocity profiles near the wall. The Reynolds stress models produce more accurate predictions than the two-equation eddy-viscosity models in the mid-field and far-field of the flow. It can be observed that in the far-field region, as shown in Figures 3.6(a) and 3.6(b), that the strength of the flow is near the wall region, $r/H>2$. In this particular region, the *RNG*, the *RKEM* and the *SST* show very poor predictions, whereas the predictions of the *KEM*, the *RSM* and the *SSG* are in good agreement with the measurements.

The predictions of the normalized tangential velocity profiles and their comparison with the experimental data are presented in Figures 3.6(c) and 3.6(d) at typical stations representative of the near-, mid- and far-fields of the flow. It can be seen from these figures that the swirl maximum velocity is at $r/H=1$ and remains almost unchanged beyond $x/H=2$. The exception occurs in the far-field near the wall region where small changes in the swirl velocity are observed as a result of wall friction. At $x/H=1$, the swirl velocity has two local maxima, one at $r/H=1$, and another at $r/H=1.75$. In the experimental work [67], it is reported that at *x/H=0.38*, the flow behaves in a swirling jet-like fashion with a weak solid body rotation around the combustor axis. Also, it is mentioned that the forced vortex rotation near the combustor axis increases in strength due to mixing as it is demonstrated by the increasing swirl velocity gradient. Outside the core region, swirl velocity decreases in a fashion similar to free vortex behaviour.

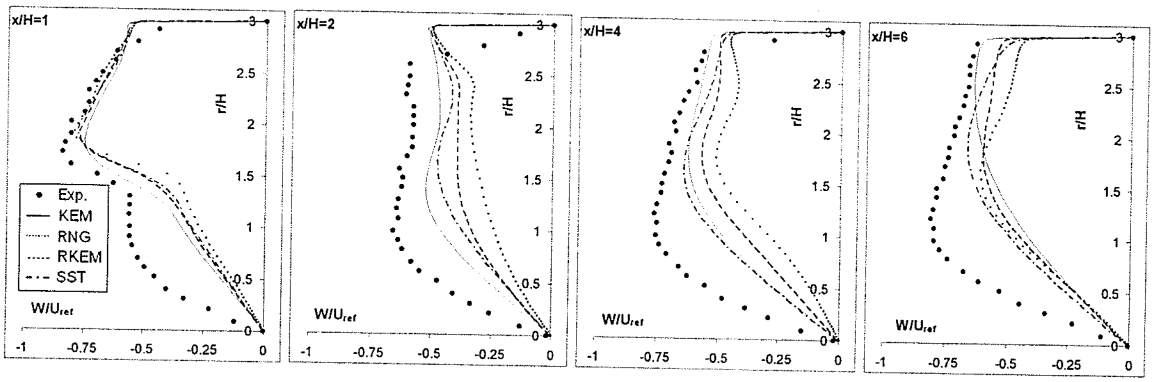

Figure 3.6(c): Radial profiles of normalized swirl velocity (S=0.81); Eddy-viscosity models

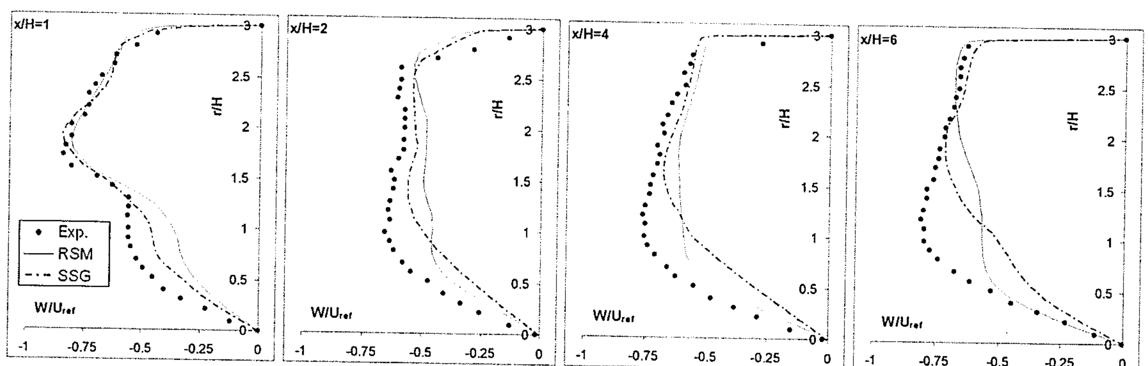

Figure3.6(d): Radial profiles of normalized swirl velocity (S=0.81); Reynolds stress closures

Figure 3.6(c) shows clearly that none of the two-equation models can predict properly the tangential velocity profiles, in which the *RNG* and the *KEM* show the worst and the best predictions, respectively. Whereas the stress models exhibit more accurate predictions than the two-equation models. In particular, the *SSG* performs better in the near-field and also at r/H >1.2 in the mid-field and far-field, while the *RSM* shows better predictions at r/H <1.2 in the mid-field and far-field.

3.3.2 Visualization of the Flowfield

The velocity vectors and streamline contours are presented in Figures 3.7 and 3.8 at different locations along the combustor length. From the experimental data [67], the following reverse flow regions can be observed: (*i*) a counter-clockwise rotating corner recirculation zone (CRZ), and (*ii*) a clockwise rotating central toroidal recirculation zone (CTRZ) which is connected with a central reverse flow region (CRR).

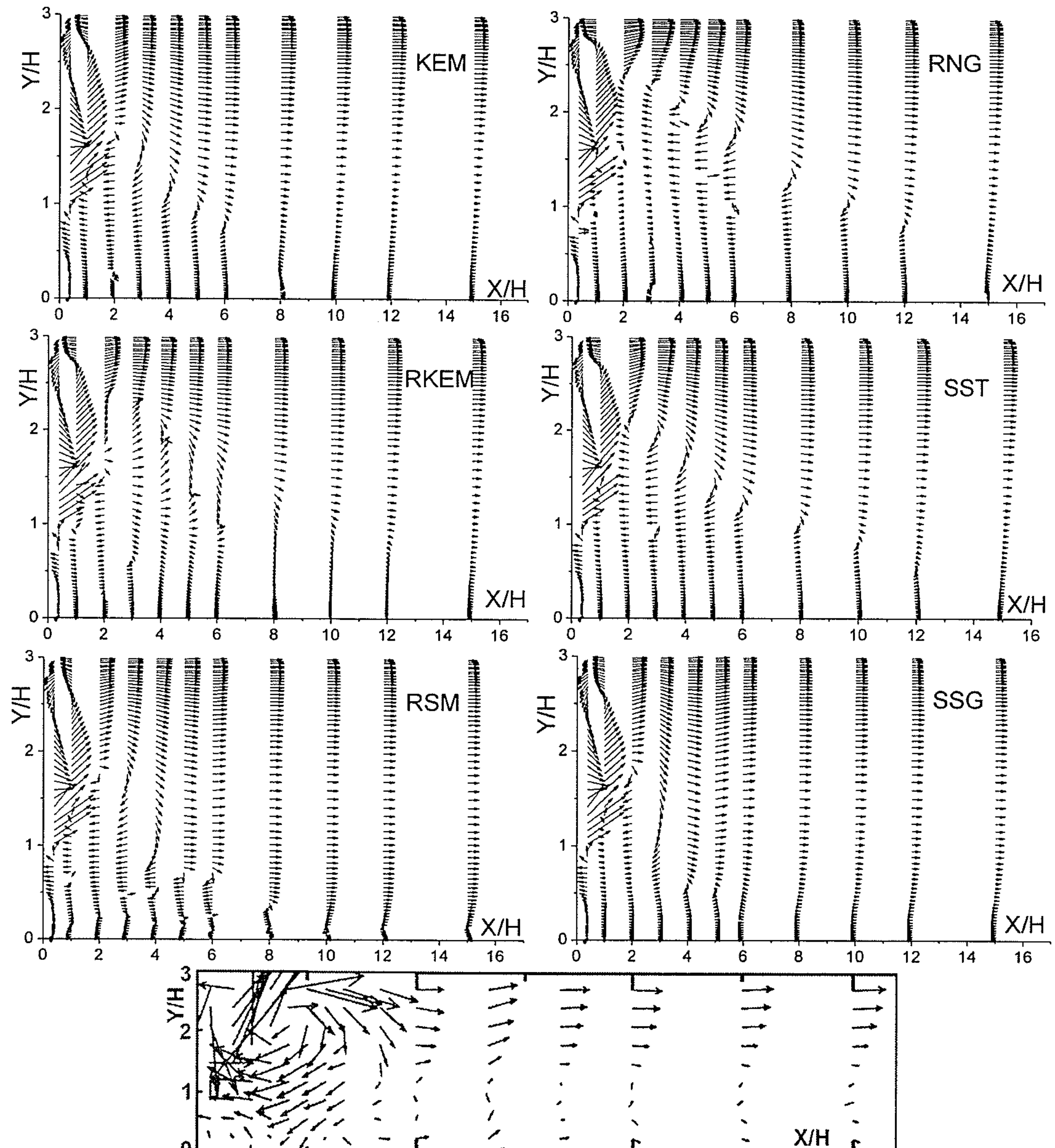

Figure 3.7: Predicted and measured velocity vectors ($S = 0.81$)

It is reported in the experiment [67] that the size of the CRZ is 1.8 step heights. As we can see in Figures 3.7 and 3.8, all the tested models can predict the existence of the CRZ in the flowfield. The predicted size of the corner reverse flow region (CRR) is in good agreement with the experiment data for all the turbulence models. Measurements show that after the corner flow reattachment point, the near wall flow adjusts itself to be approximately parallel to the combustor centerline in the far-field. From the predicted streamline contours which are shown in Figure 3.8, it is demonstrated clearly that this phenomenon is captured by all the turbulence models tested here, except the *RNG* which shows streamlines non-parallel to the combustor axis in the far-field near the wall region.

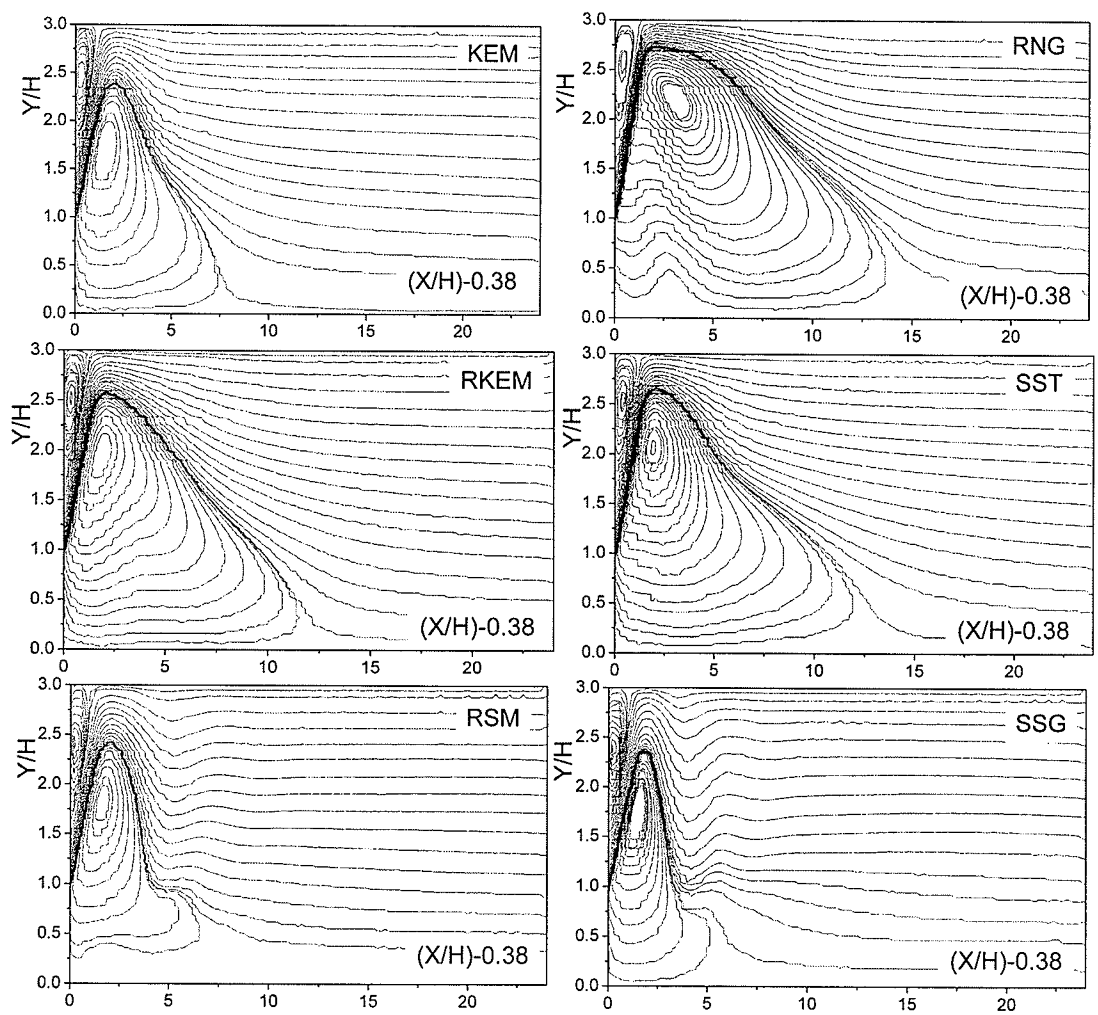

Figure 3.8: Predicted streamline contours ($S = 0.81$)

Also, experimental data [67] show that the CTRZ starts upstream of the dump plane and extends to roughly 6 step heights downstream of the dump plane with a maximum radius of $r/H=2.4$ at $x/H=2.5$. The centre of this recirculation zone is located approximately at $r/H=2.1$ and $x/H=2.4$. It can also be seen in the experimental data that the CTRZ is connected with the CRR which extends all the way downstream up to the outlet of the combustion chamber. Figures 3.7 and 3.8 show that all the employed models can predict the CTRZ, but with different shapes and sizes. The predicted length (in x-direction) and width (in y-direction) of the CTRZ by these models is summarized in Table 3.4.

Table 3.4: Measured and predicted length and width of the CTRZ for $S = 0.81$

	Experiment	KEM	RNG	RKEM	SST	RSM	SSG
$(x/H)_{max}$	6	7.5	14	12	12.5	7	5.5
$(y/H)_{max}$	2.4	2.4	2.75	2.6	2.7	2.4	2.35

The predicted sizes of the CTRZ by the stress models are better than those of the two-equation models. The predictions of the CTRZs by the *RNG*, the *RKEM* and the *SST* are much longer than the experimental value. Inadequacy of the two-equation models to accurately predict the size of the CTRZ is mainly due to the isotropic eddy viscosity assumption, while the flowfield is highly anisotropic, especially in the near-field.

As mentioned previously, the experimental velocity profiles show that a region of reverse flow (CRR) exists even far downstream of the dump plane. Therefore, one can say that the axial flow does not recover and the velocity distribution is far from the fully developed turbulent pipe flow. From the predictions of the velocity vectors in the *UV* plane, shown in Figure 3.7, it is clear that only the *RNG* and the *RSM* can capture this phenomenon all the way up to the outlet of the combustor. All the other models predict a fast recovery of the axial velocity near the combustor axis. The turbulence models *KEM*, *RKEM*, *SST* and *SSG* predict no reverse flow beyond $x/H=10$, 12, 12, and 8, respectively.

In conclusion, for the flow configuration with high Swirl numbers, that is for $S=0.81$, it is found that the two-equation eddy viscosity models predict reasonably well the axial velocity only in the near flow-field and poorly elsewhere. However, the same axial velocity profiles are generally reasonably predicted by the Reynolds stress models. As for the tangential velocity profiles, the two-equation eddy-viscosity models show poor predictions, whereas the combination of the two *RSM* and *SSG* models produce good predictions. Indeed, in the near-field, the *SSG* model produce the best profiles everywhere except near the centreline where the tangential velocity is underpredicted to less than 10% as compared to their experimental counterparts. In the mid and far fields, the *RSM* model shows superior predictions than the *SSG* model, although the tangential velocity is underpredicted, especially near the centreline, to less than 15% in the mid field and less than 25% in the far-field. It is also found that the predicted size of the CRZ by all the two-equation as well as the Reynolds stress models is in good agreement with the experimental data. In addition, all these models can predict the CTRZ, though with different sizes. The predicted length and width of the CTRZ by the *KEM* is the best when compared to the predictions of the other two-equation models. On the other hand, the size of the CTRZ is much better predicted by the stress closures in comparison with the experimental values.

3.3.3 Turbulence Quantities

The measured and predicted turbulence intensities and Reynolds shear stresses for the strongly swirling flow are shown in Figures 3.9(a)-(d). Comparing the measured values of the three turbulence intensity components in Figures 3.9(a)-(b), it can easily be seen that the flow is anisotropic.

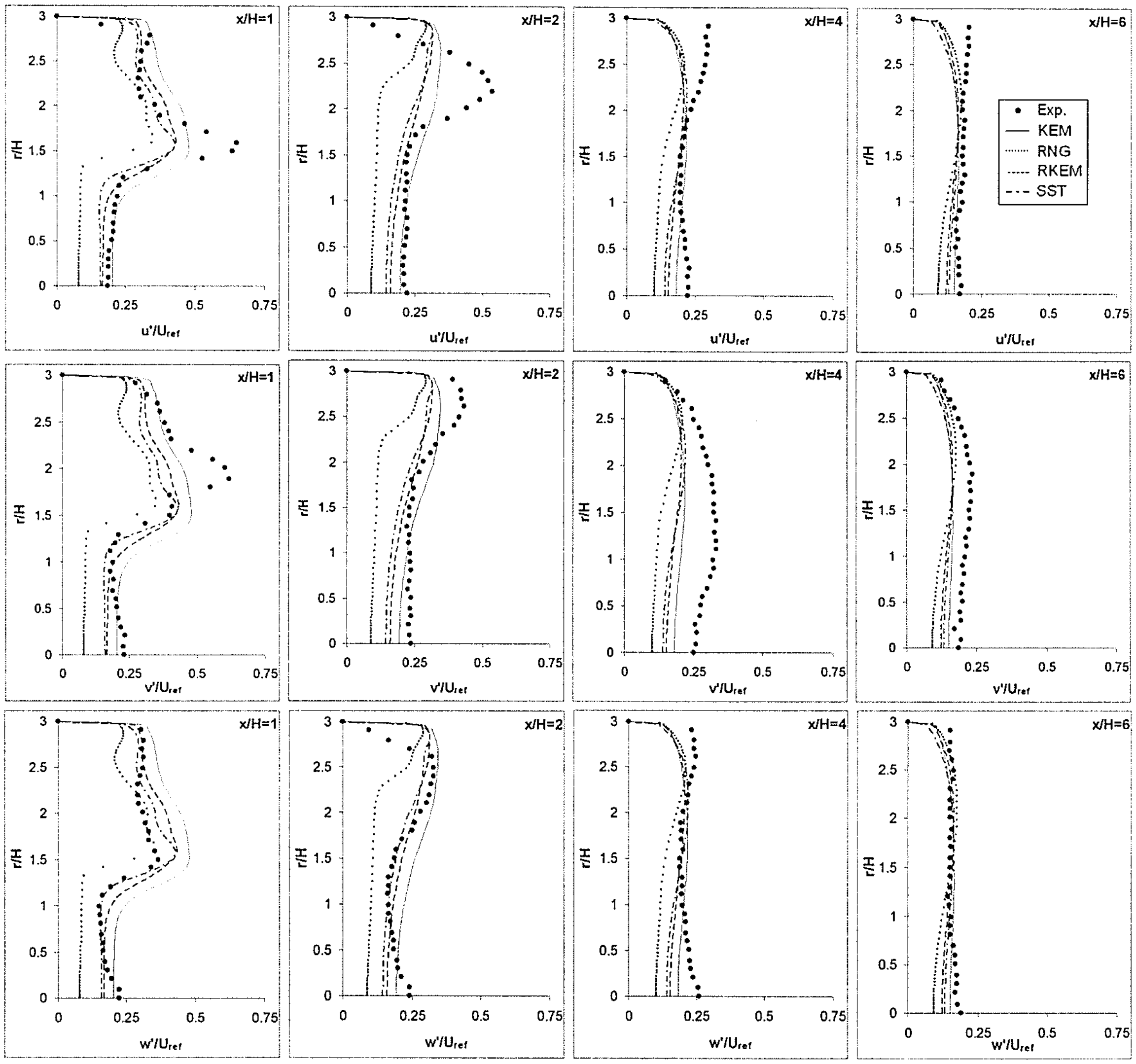

Figure 3.9(a): Radial profiles of normalized turbulence intensities (S=0.81); Eddy-viscosity models

Normal stresses reveal one peak at $r/H \approx 1.5$ as shown in the near-field regions of Figures 3.9(a) and 3.9(b). Turbulence activities decrease in the mid- and far-field. The peak value of axial normal stresses moves toward the wall as it decays in strength and grows in size, indicating a progressive development of the jet flow [67]. In the near-field, the *RNG* shows the worst results in the prediction of the axial turbulence intensity, while the performance of the other eddy-viscosity models is satisfactory, though still less accurate when compared to the predictions of the stress closures. The peak values of the normal stresses in the mid-field occur near the walls where most of the flow is located. In the mid-field, again the *RNG* shows very poor results in predicting u'. The performance of the *KEM* is comparable to those of the *RSM* and the *SSG*.

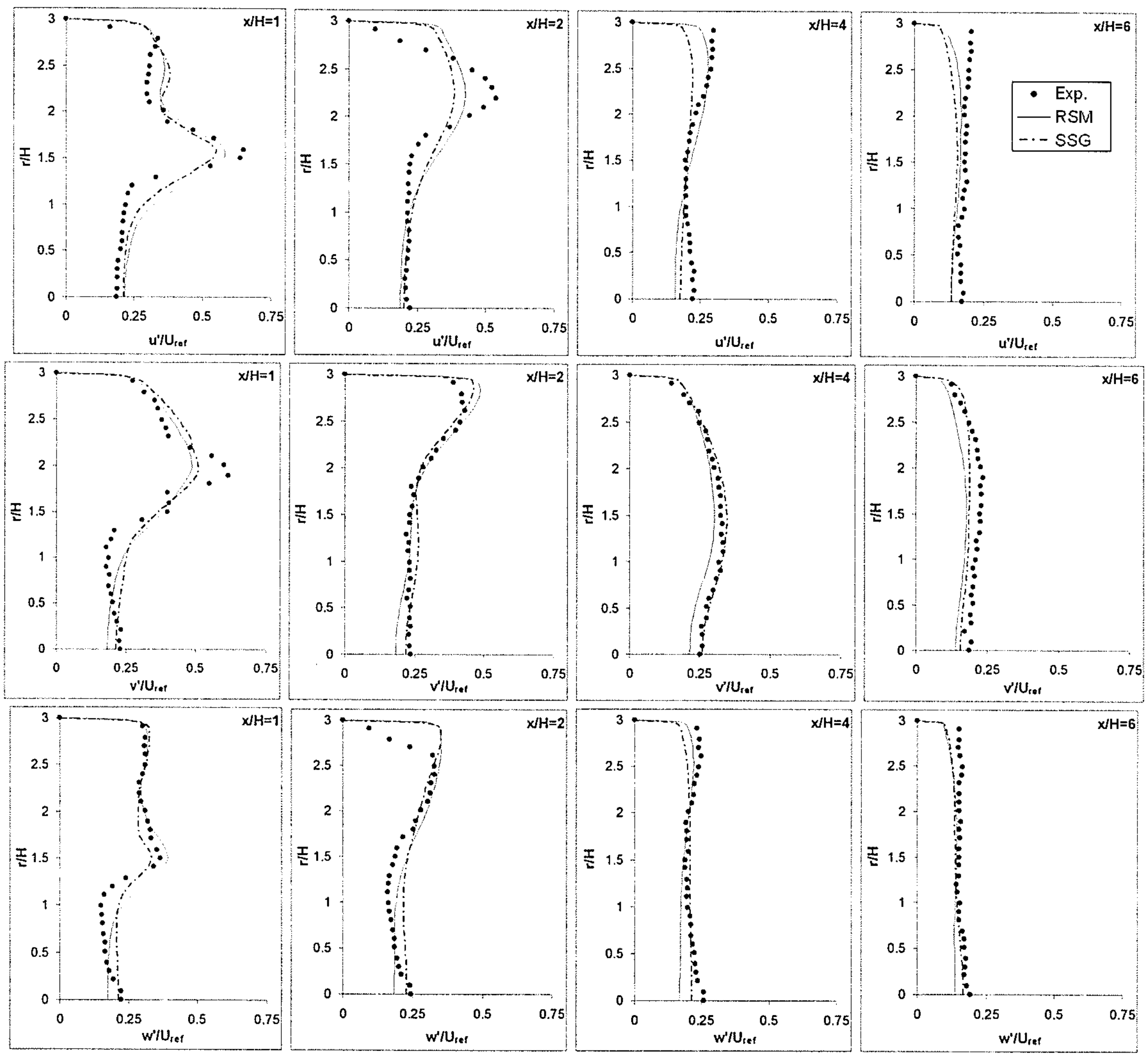

Figure 3.9(b): Radial profiles of normalized turbulence intensities (S=0.81); Reynolds stress closures

In the far- and very far-field regions, turbulence activity is weak except for the reverse flow regions near the centerline. In the experimental paper [67], it is mentioned, and not shown, that in the very far-field, $x/H>6$, the peaks occur at the centerline since the mixing near the wall disappears and the reverse flow is located only near the centerline. All the employed models underpredict the values of the turbulence intensities near the centerline in the far-filed; however the *SSG* shows more accurate results in this region. The features of the radial and tangential turbulent normal stresses are similar to those of the axial normal stresses, except in the mid-field of v' where the peak occurs at $r/H \approx 1.5$. The *RNG* shows the worst results in the prediction of these two components of the turbulence intensity, while the results of the other eddy-viscosity models are in fairly good agreement with the measured data. Similar to the predictions of the Reynolds stress closures for the axial turbulence intensity, the results of the *RSM* and the *SSG* for v' and w' are superior to those of the eddy-viscosity models.

Profiles of the Reynolds shear stresses presented in Figures 3.9(c)-(d) show that the swirling jet flow is thin near the dump plane and then expands to fill the entire combustor in the far-field [67]. Since the magnitude of the Reynolds shear stresses in the mid- and far-field is small, the differences between the results obtained by using different models are not very large.

In the near-field, the eddy-viscosity models do not depict the experimental trends of $\overline{u'v'}$. On the other hand, the stress closures show the same trends as those of the experiment with different magnitudes. In the prediction of the second Reynolds shear stress, $\overline{u'w'}$, all the models show fairly good results in the near-field, except in the near-wall region. In the mid-field, none of the models are able to predict $\overline{u'w'}$ accurately.

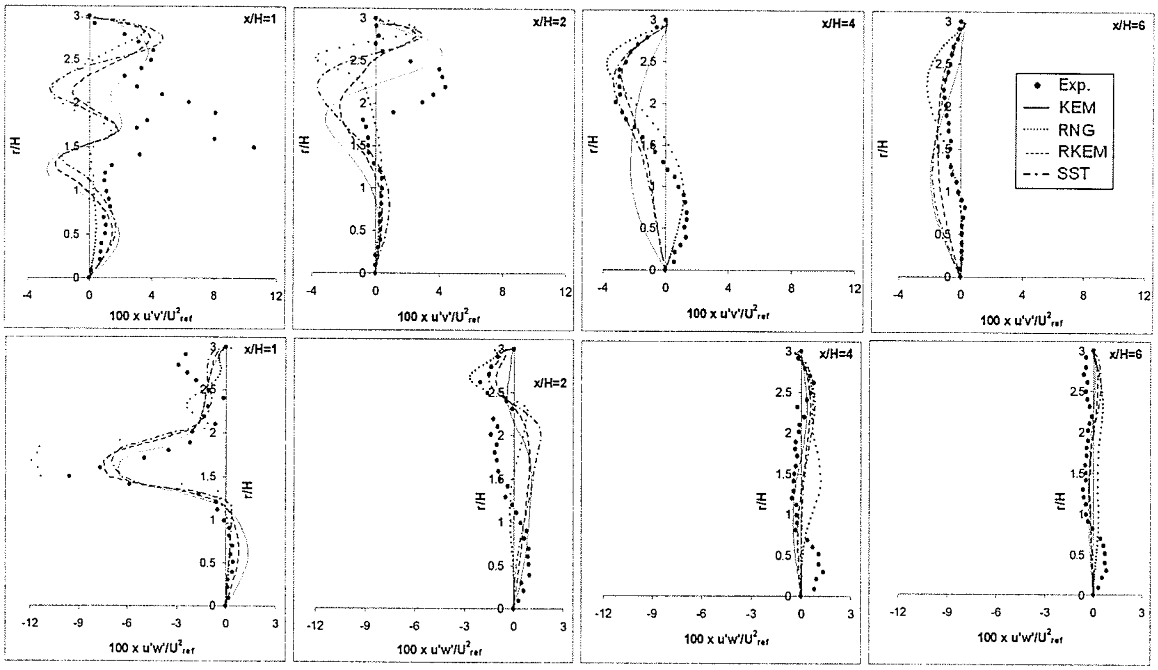

Figure 3.9(c): Radial profiles of normalized shear stresses (S=0.81); Eddy-viscosity models

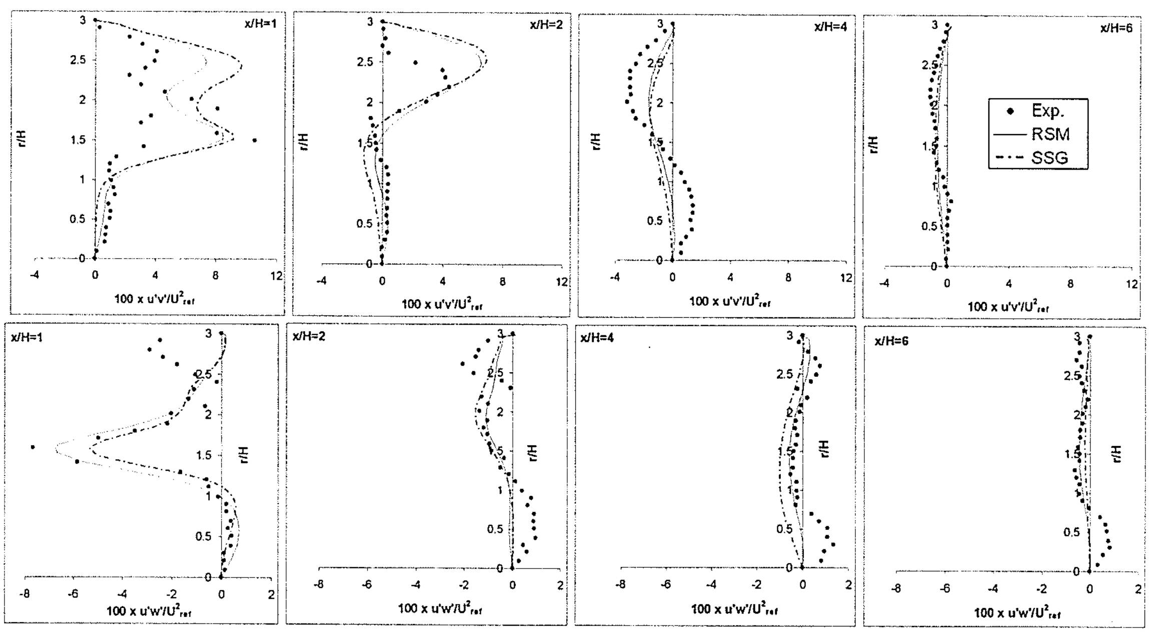

Figure 3.9(d): Radial profiles of normalized shear stresses (S=0.81); Reynolds stress closures

In conclusion, among the eddy-viscosity models, the *RKEM* shows better predictions of the turbulence field. The numerical results based on the two Reynolds stress closures are all better than those obtained by the eddy-viscosity models, especially in the near-field region where the flow is highly anisotropic. However, even the *RSM* and the *SSG* fail to reproduce accurate enough results in the near wall region at some axial locations (e.g. at $x/H=2$) and also, as mentioned before, near the centerline in the far-field.

Chapter 4

THREE-DIMENSIONAL SIMULATION OF TURBULENT FREE JETS ISSUING FROM NON-CIRCULAR GEOMETRIES WITH CORNERS

4.1 Turbulent Free Jet Issuing from an Equilateral Triangular Orifice

4.1.1 Problem Definition and Solution Procedure

The physical problem consists of a free jet of air injected into still atmosphere of air from an equilateral triangular orifice. The jet, which is assumed steady and incompressible, and its surrounding air are considered having the same (room) temperature. Therefore, the flow is governed by Eqs. (2.1) and (2.2) mentioned in the previous chapter. Because the flow is turbulent, the Reynolds stresses in Eq. (2.2) are solved by using the turbulence closure models described in chapter 2. The triangular orifice and the computational domain are shown in Figure 4.1.

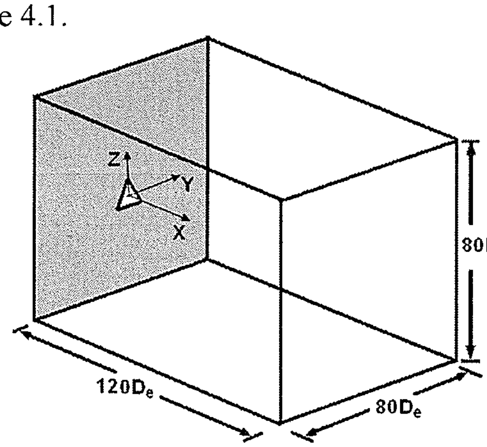

Figure 4.1: Schematic of the triangular orifice geometry and the computational domain

The test conditions are set as follows. The mean streamwise velocity at the center of the orifice exit plane is 61 m/s, which corresponds to a Reynolds number of 1.84×10^5 based on the orifice equivalent diameter (D_e = 45.3mm)*. This choice is based on the experimental data provided by Quinn [68]. Note that experimental data are available

* The equivalent diameter, D_e, is defined as $\pi/4D_e^2 = A$, where A is the surface area of the orifice.

starting from $x/D_e=0.5$ downstream of the orifice exit plane. Therefore, the experimental data at this nearest location to the nozzle exit are used as the inlet boundary conditions. The experimental data for the turbulence kinetic energy (k) at $x/H=0.5$ is used as the inlet boundary condition for k. In order to calculate the dissipation rate of the turbulence kinetic energy (ε) at the inlet of the computational domain, Eq. (3.1) is used. In this equation, l is the turbulence length scale which can be approximated as $0.33D_e$. This approximation is found to be realistic for free jet flows within the range of Reynolds number employed in the present study [152]. The computational domain is chosen to be long enough to ensure complete development of the flow; that is, up to $x/D_e=120$. In the lateral sides, i.e. y and z directions, the computational domain is $80De$ wide. At the outlet and at the four lateral planes, a zero gradient along the normal vector of the planes is assumed for all the variables. A two-layer-based, non-equilibrium wall function [148] is used near the wall. Details of the wall function used in the simulation of this flow case are presented in Appendix B. In the present work, the wall-adjacent cell's centroid is located at $y^+(=U_\tau y/\nu)\approx 45$.

The preliminary tests led to determine that the coarsest mesh which results in a converged solution is of the size $96\times78\times78$ in the axial (x) and lateral (y and z) directions, respectively. A medium size mesh is chosen to be of the size of $110\times88\times88$. A non-uniform mesh is made finer near the inlet and the axis. Grid independency is verified by using a finer mesh of the size of $152\times120\times120$. It is observed that the maximum difference between the results of the medium and the finest mesh sizes is 2.05%, which is found along the centerline. Therefore, in order to minimize the computational time, the medium mesh is used for all the simulations.

The commercial FLUENT software version 6.1.22, which is based on finite volume formulation, is employed to solve the governing equations. Details about the solution algorithm are reported in AppendixA. The PISO [149] method is applied for the pressure-velocity coupling. QUICK [150] scheme is used for the convection terms in all transport equations, and the PRESTO [41] method is used for the pressure discretization. The solution convergence is assumed when all of the residuals parameters* fall below 10^{-5}.

4.1.2 Results and Discussion

4.1.2.1 Mean velocity field

Figures 4.2 and 4.3 show the decay of the streamwise mean velocity along the jet centerline in the near-field and the entire field, up to $x/D_e=60$, respectively. Note that U_{max} in Figures 4.2 and 4.3 is the maximum of the streamwise mean velocity on the jet centerline. Figures 4.2(a) and 4.3(a) are the predictions of the eddy-viscosity models, while Figures 4.2(b) and 4.3(b) are the predictions of the Reynolds stress closures.

Measurement of the flowfield has been done by using a hot-wire anemometry system [68]. It was reported that the maximum uncertainty in the measurement of the streamwise mean velocity was approximately 1% [68].

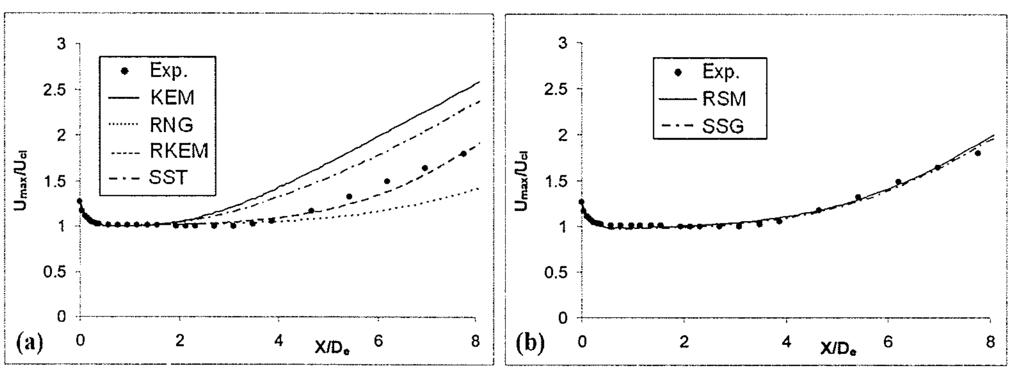

Figure 4.2: Streamwise mean velocity decay along the jet centerline in the near-field region; (a) Eddy-viscosity models, (b) Reynolds stress closures

* The definition of these parameters is reported in Appendix A.

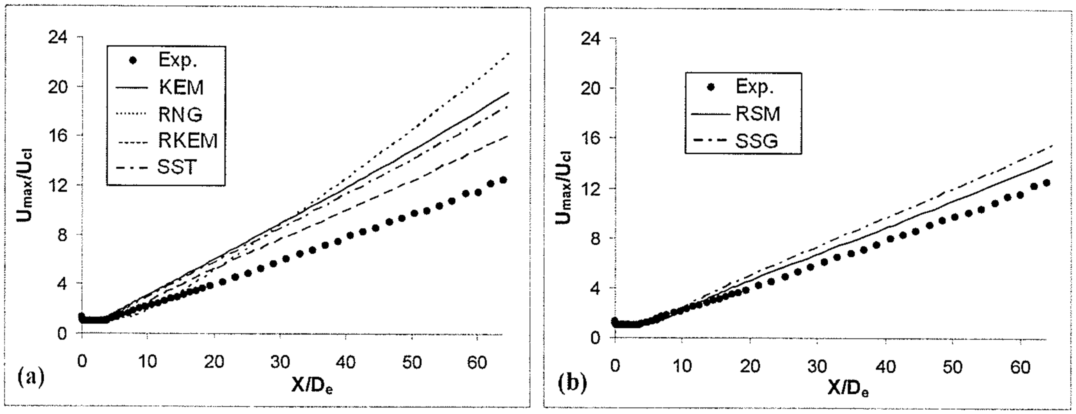

Figure 4.3: Streamwise mean velocity decay along the jet centerline; (a) Eddy-viscosity models, (b) Reynolds stress closures

The experimental data in Figure 4.2 shows that the U_{max}/U_{cl} value at the exit plane is greater than unity because of the *vena contracta* effect, which is associated with the sharp-edged orifices [68]. It is clear that all the closure models are able to capture the vena contracta, i.e. the initial acceleration of the flow. As shown in Figure 4.2(a), the *RKEM* predictions in the near-field region, i.e. approximately up to $x/D_e<8$, are very close to the experimental data and are comparable to those of the *RSM* and the *SSG* shown in Figure 4.2(b). In this region, the *KEM* shows the worst results. Among the eddy-viscosity models, the *RNG* shows the best predictions of the streamwise mean velocity decay along the jet centerline in the region $10<x/D_e<20$, as shown in Figure 4.3(a). On the other hand, in the region that extends from $x/D_e>30$, its results are far away from the experimental data. For example, it has about 75% error, when compared to the experimental data, at $x/D_e=50$. Overall, among the eddy-viscosity models, the *RKEM* shows the best prediction of the streamwise mean velocity decay along the jet centerline. However, its results are less accurate than those of the *RSM* and the *SSG* in the mid- and far-field. The *RSM* shows the most accurate results in predicting the decay of the streamwise mean velocity along the jet centerline, but it still slightly overpredicts the experimental data. For example, it shows 14% error at $x/D_e=50$.

The *KEM* and the *RNG*, in Figure 4.2, show the highest and the lowest decay rate of the streamwise velocity along the jet centerline in the near-field, respectively. This indicates that the *KEM* and the *RNG* predict the highest and the lowest mixing rate in the near-field, respectively.

The normalized streamwise mean velocity profiles in the central *x-y* and *x-z* planes at three typical axial locations are presented in Figures 4.4 and 4.5, respectively. In comparison with all the tested models, the *RSM* produces the best predictions of the streamwise mean velocity profiles. However, it is unable to capture accurately enough the top-hat feature (i.e. flatness) of the streamwise velocity profile in the very near-field near the centreline in the central *x-y* plane.

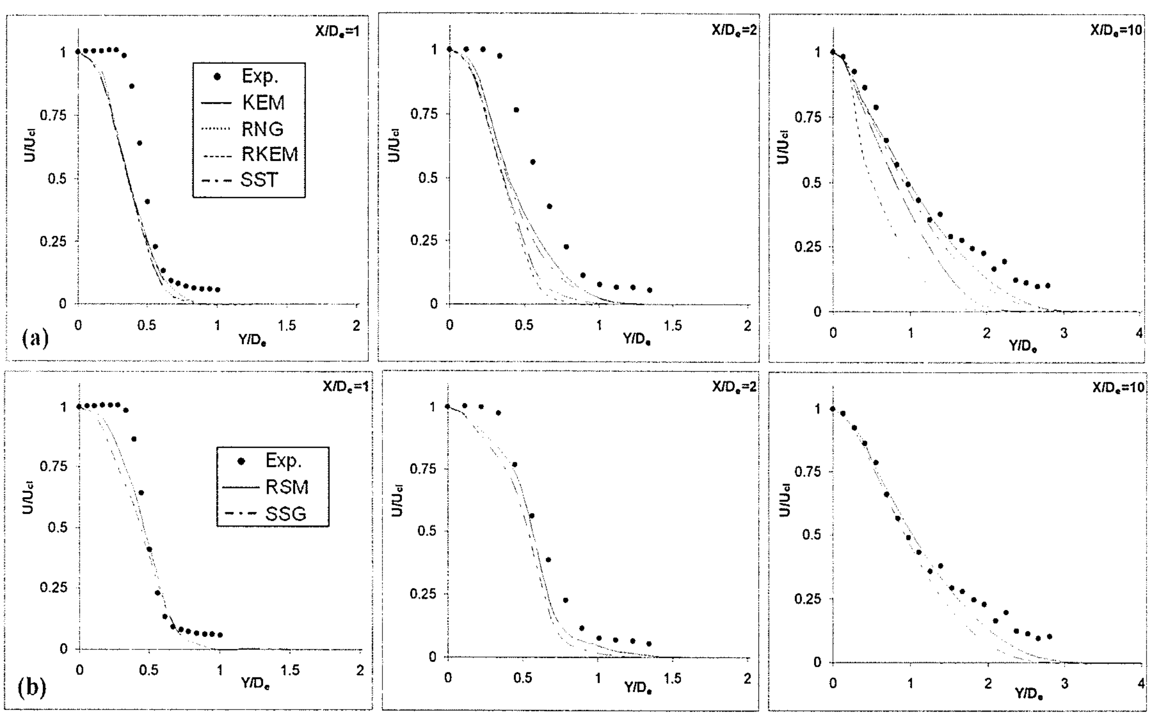

Figure 4.4: Normalized streamwise mean velocity profile in the central *x-y* plane; (a) Eddy-viscosity models, (b) Reynolds stress closures

Figures 4.4 and 4.5 show that among the eddy-viscosity models, the *KEM* and the *RNG* show the best and the worst results, respectively, in predicting the streamwise mean velocity profiles, however, the predictions of the *RKEM* and the *SST* are competetive. The performance of the *SSG* is better than those of the eddy-viscosity models. However, it is less accurate than that of the *RSM.*

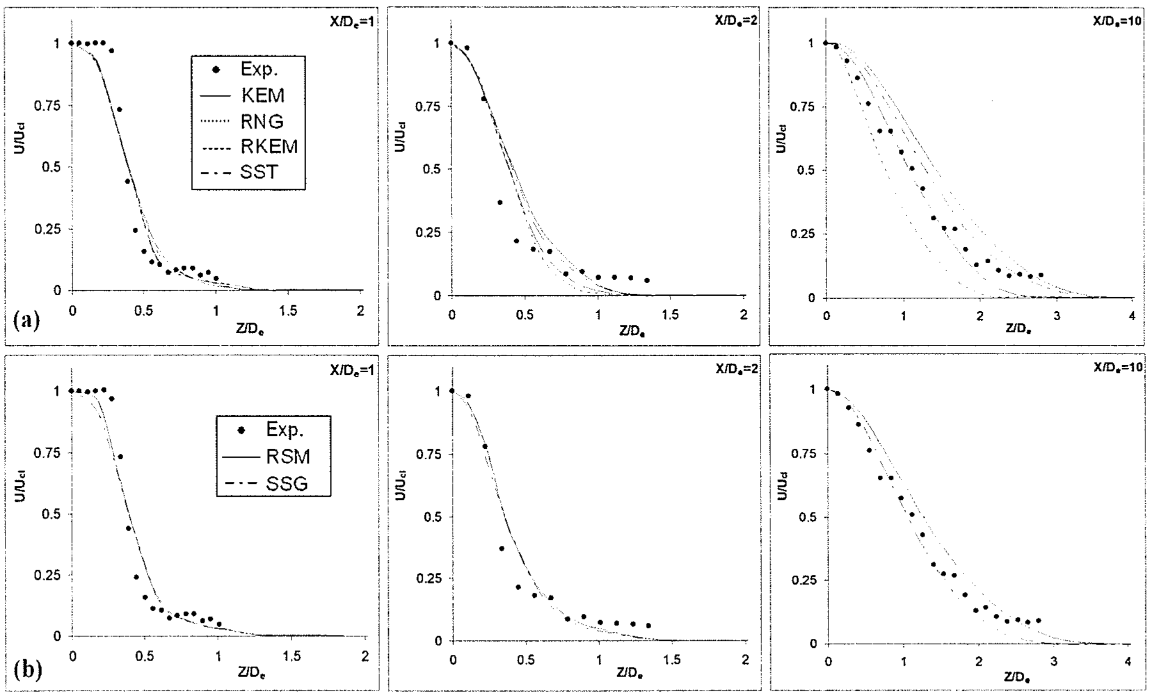

Figure 4.5: Normalized streamwise mean velocity profile in the central *x-z* plane; (a) Eddy-viscosity models, (b) Reynolds stress closures

The development of the jet half-velocity width (where $U/U_{cl}=0.5$) in the central *x-y* and *x-z* planes is presented in Figures 4.6 and 4.7, respectively. It was reported that because of the vena contracta effect, the jet half-velocity width decreases initially, and then increases with downstream distance triggered by the large-scale structures emanating from the flat sides of the triangular orifice [68].

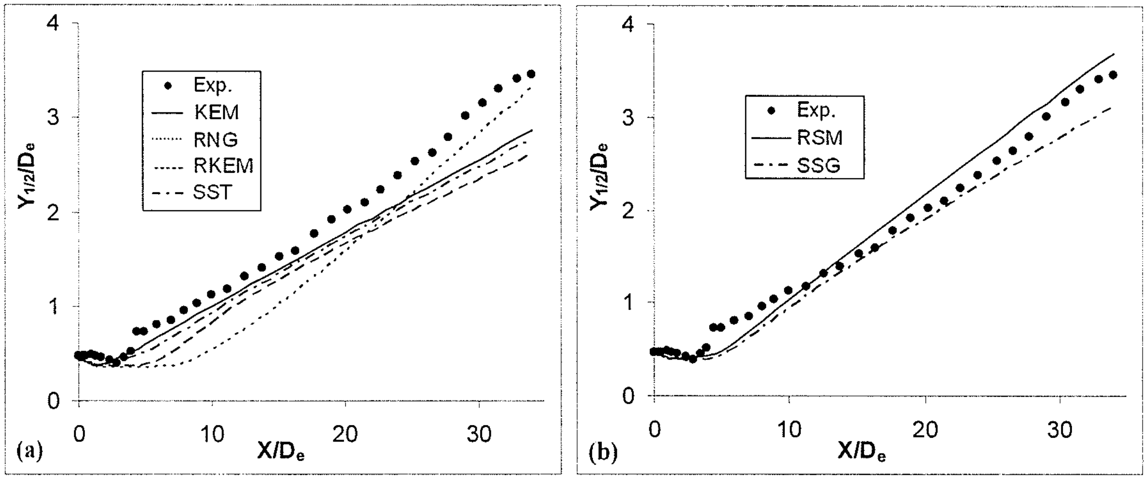

Figure 4.6: Development of the jet half-velocity width in the central *x-y* plane; (a) Eddy-viscosity models, (b) Reynolds stress closures

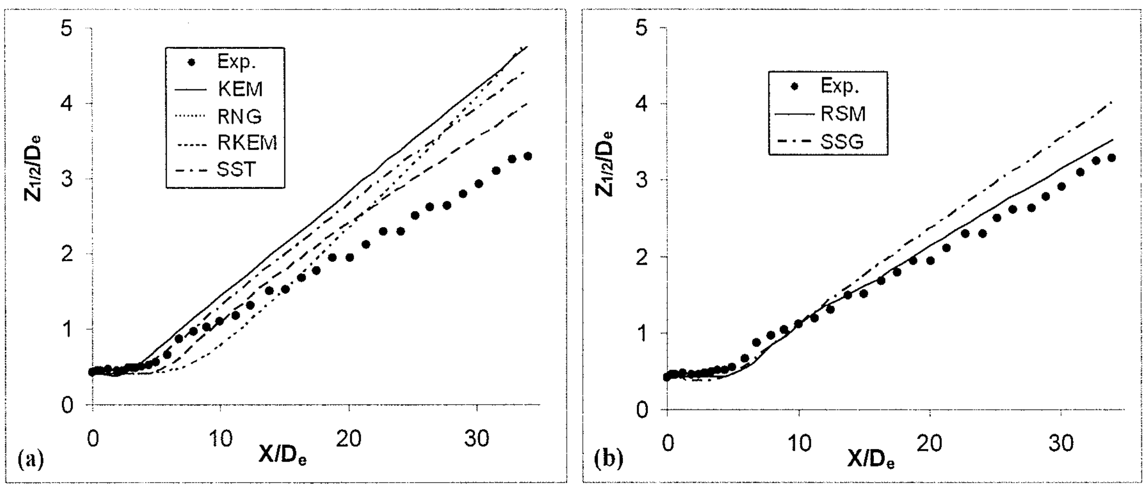

Figure 4.7: Development of the jet half-velocity width in the central *x-z* plane; (a) Eddy-viscosity models, (b) Reynolds stress closures

Comparing the performance of the eddy-viscosity models in predicting the development of the jet half-velocity width, it can be seen in Figures 4.6 and 4.7 that the *KEM* and the *RKEM* show the best prediction in the central *x-y* and *x-z* planes, respectively. These figures show that both the Reynolds stress models show better results than the eddy-viscosity models in predicting the $Y_{1/2}$ and $Z_{1/2}$. The *RSM* almost reproduces the experimental data.

Geometric mean of the jet half-velocity widths, defined as $B_e = (Y_{1/2} \times Z_{1/2})^{0.5}$, is shown in Figure 4.8. This quantity can be used to compare the predictions of different models, when the spread of the jet is considered.

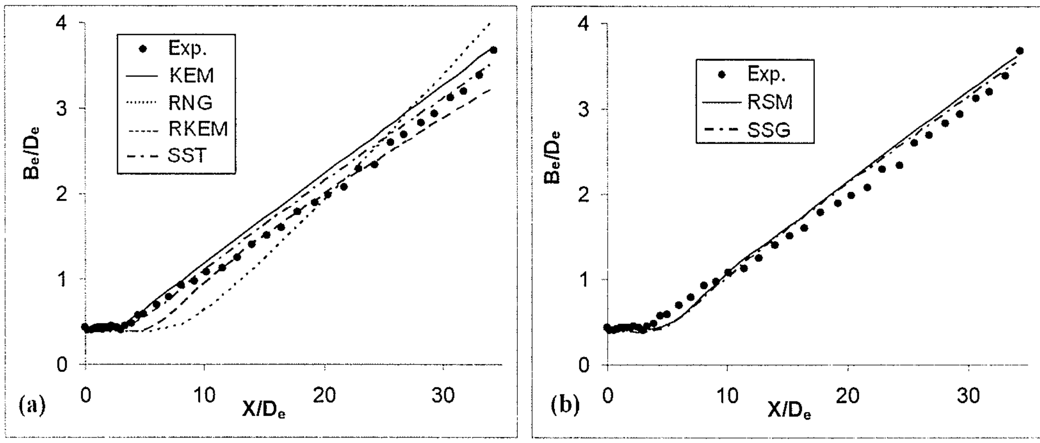

Figure 4.8: Geometric mean of the jet half-velocity widths; (a) Eddy-viscosity models, (b) Reynolds stress closures

Figure 4.8 shows clearly that the geometric mean of the jet half-velocity widths is well predicted by all the tested models, with exception of the *RNG* which shows a very slow spreading rate up to $x/D_e=20$, and then a fast spreading rate after this point. The *KEM* shows relatively the highest values of the geometric mean of the jet half-velocity widths in the region $x/D_e<25$. This points to a relatively faster mixing predicted by the *KEM* in the near-field compared to that of the other models. On the other hand, both the *SSG* and the *RSM* appear to reproduce the experimental data.

4.1.2.2. Turbulence quantities

Figure 4.9 shows the radial profiles of the normalized measured and predicted turbulence intensity components along the jet centerline.

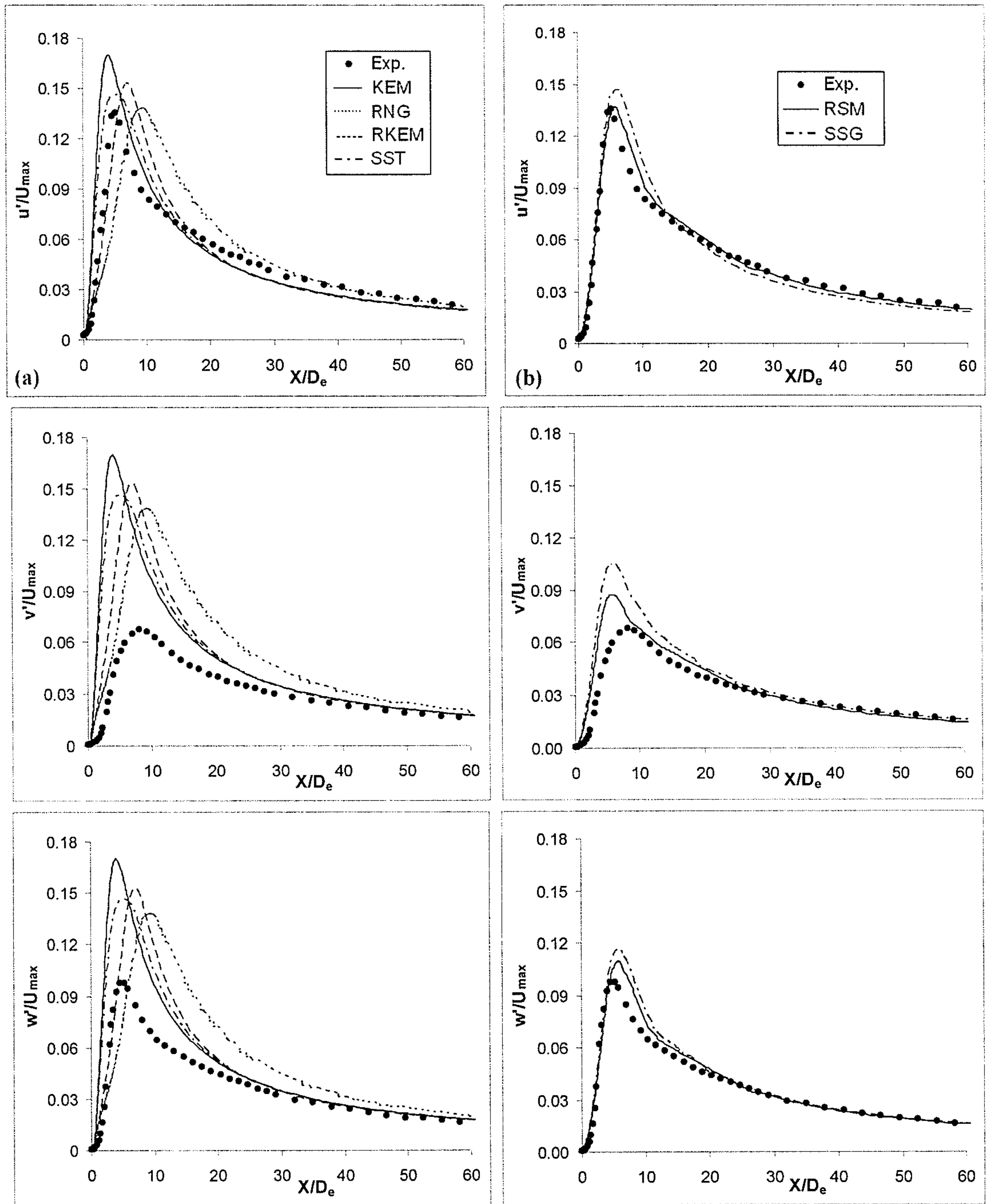

Figure 4.9: Evolution of the normalized turbulence intensity components along the jet centerline; (a) Eddy-viscosity models, (b) Reynolds stress closures

This figure reveals a steep initial increase of the three components of turbulence intensity. It was reported that this is because of the production of turbulence from the mean flow shear in the shear layers emanating from the flat sides of the triangular orifice and diffusion of the turbulence from the shear layers to the jet centerline [68]. The experimental data of the normalized u', v' and w' show a peak along the centerline. Although all the eddy-viscosity models appear to predict this peak, they overpredict widely its magnitude. Also, they are unable to predict the exact axial location of the peak. The predictions of the streamwise turbulence intensity, u', for which most of the eddy-viscosity models are able to approach the experimental data, apart from the *KEM* and the *RNG*, are acceptable. On the other hand, in the prediction of the spanwise, v', and the lateral, w', turbulence intensity components, the *RSM* and the *SSG* are in fair agreement with the experiment. The eddy-viscosity models are inadequate to predict the accurate magnitude of these two components, especially in the near- and mid-field regions where the flow is anisotropic. The *RSM* shows slightly more accurate predictions of the turbulence intensities than the *SSG*. For example, the peak magnitude of v' and w' is 29% and 12% overpredicted by the *RSM*, respectively, while the *SSG* overpredicts these quantities by as much as 55% and 19%.

4.2 Turbulent Free Jet Issuing from a Pipe with an Equilateral Triangular Collar

4.2.1 Problem Definition and Solution Procedure

The physical problem consists of a turbulent jet of air issuing from a pipe with a triangular collar. The circular nozzle and the triangular collar are shown schematically in Figure 4.10(a) and Figure 4.10(b) shows the computational domain. The length of the equilateral triangular collar, L_c, is twice the diameter of the circular nozzle (D = 15 mm) and its equivalent diameter is D_e = 23.15 mm. The expansion ratio (D_e/D) is 1.54.

The flow is assumed steady, incompressible and isothermal. The governing equations (Eqs. 2.1 and 2.2), are solved by using the commercial FLUENT software. The *k-ε* and the standard *RSM* turbulence models are employed to close the system of equations.

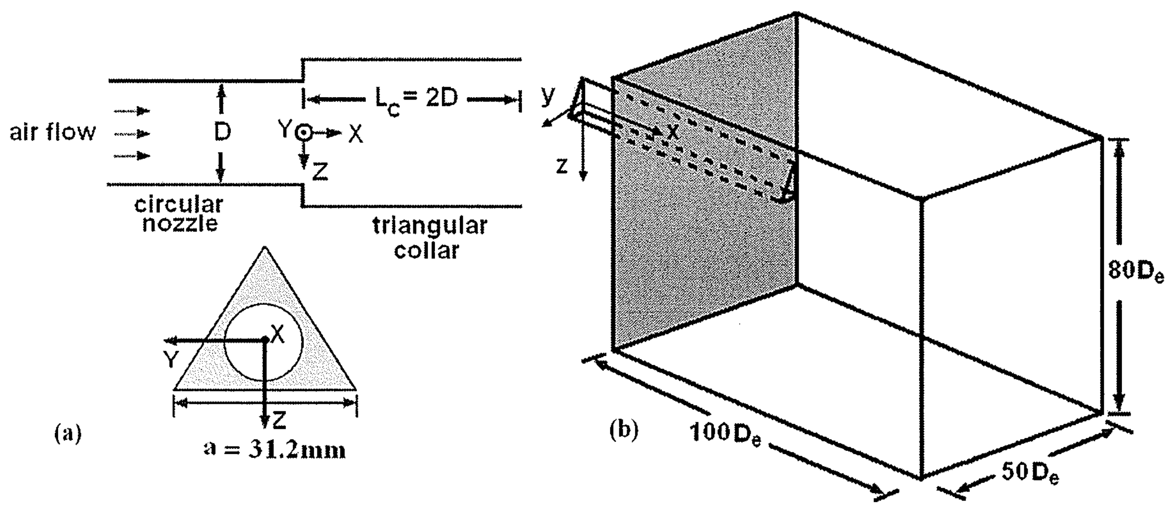

Figure 4.10: (a) Schematic of the circular nozzle with equilateral triangular collar; (b) Computational domain

Note that experimental data, reported by New et al. [137], are available starting from $x/D_e=0.33$ downstream of the circular nozzle exit plane. The experimental data at this nearest location to the nozzle exit are extrapolated to be used as the inlet boundary conditions at $x/D_e=0$. In order to calculate the dissipation rate of the turbulence kinetic energy (ε) at the inlet of the computational domain, Eq. (3.1) is used. The turbulence length scale, l, in this equation is approximated as $0.33D_e$ as mentioned previously, where D_e is the equivalent diameter of the triangular collar. The streamwise mean velocity at the center of the circular nozzle exit plane is taken to be 20 m/s, which corresponds to a Reynolds number of 2.0×10^4 based on the circular nozzle diameter. Because of the symmetry, only half of the geometry is simulated (positive y axis in Figure 4.10). The computational domain is chosen to be long enough to ensure complete development of the flow; that is, up to $x/D_e=100$. In the lateral sides, i.e. y and z directions, the computational domain is $50De$ and $80De$ wide, respectively. At the outlet as well as at the three lateral planes, a zero gradient along the normal vector of the planes is assumed for all the variables. Symmetry boundary condition, which assumes a zero normal gradient for all variables at a symmetry plane, is applied to the other lateral plane (i.e. $y=0$ plane) which is parallel to x-z plane. A two-layer-based, non-equilibrium wall function [148] is used near the walls of the triangular collar. Details of the non-equilibrium wall function are presented in Appendix B.

The numerical mesh in the cube after the collar in Figure 4.10 is chosen to be $120\times86\times120$ in the axial (x) and lateral (y and z) directions, respectively. A non-uniform mesh is made finer near the inlet and the axis. A uniform mesh of $26\times32\times22$ in the axial (x) and lateral (y and z) directions, respectively, is used in the collar. Grid independency is verified by using a $150\times118\times160$ mesh in the cube and a $36\times44\times30$ mesh in the collar. It is observed that the maximum difference between the results for the two mesh sizes is less than 1.81 %, which occurs along the centerline. Therefore the coarser mesh is used for all the simulations.

To solve the governing equations, the commercial FLUENT software version 6.1.22, which is based on finite volume formulation, is employed. The PISO [149] method is applied for the pressure-velocity coupling. QUICK [150] scheme is used for the convection terms in all transport equations, and the PRESTO [41] method is used for the pressure discretization. The solution convergence is assumed when all of the residuals parameters fall below 10^{-5}.

4.2.2 Results and Discussion

4.2.2.1 Mean velocity field

Figure 4.11 shows the decay of the streamwise mean velocity along the jet centerline in the region up to *x/D=20*. Note that U_e in Figure 4.11 is the streamwise mean velocity at the circular nozzle exit. The *KEM* shows acceptable predictions of the streamwise mean velocity decay along the jet centerline. However, its results are less accurate than those of the *RSM*. The *RSM* predictions are in fair agreement with their experimental counterparts.

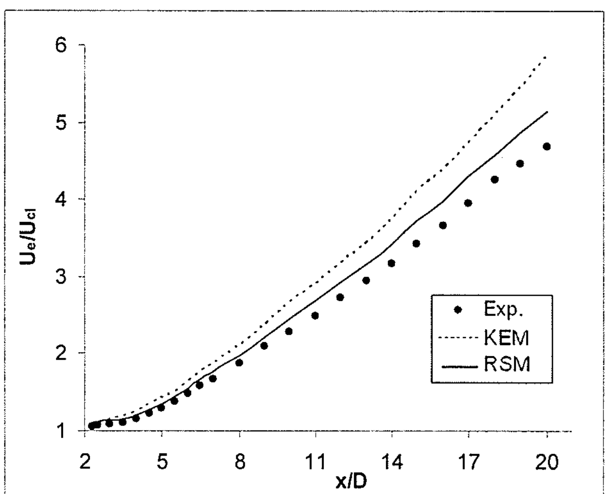

Figure 4.11: Streamwise mean velocity decay along the jet centerline

Measurement of the flowfield has been done by using a hot-wire anemometry system [137]. It was reported that the maximum uncertainty in the jet flow velocity metering was approximately 2% [137].

The development of the jet half-velocity width in the planes of minimum and maximum step-height is presented in Figures 4.12 and 4.13, respectively. Comparing the performance of the two tested models, again, the *RSM* shows far better predictions of $R_{1/2,min}$ and $R_{1/2,max}$ than the *KEM*. For example, at $x/D=15$, the jet half-velocity width in the planes of minimum step-height is 8% and 28% overpredicted by the *RSM*, and the *KEM*, respectively.

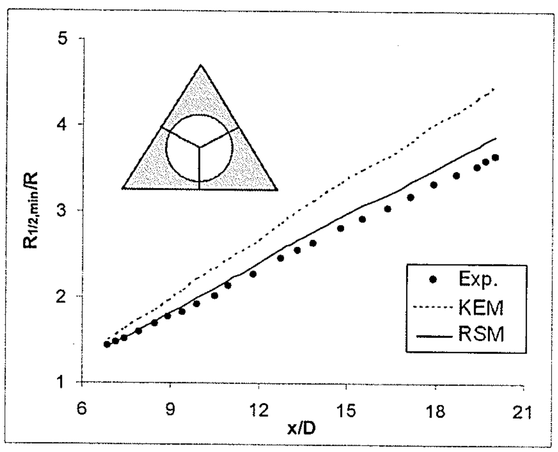

Figure 4.12: Development of jet half-velocity width in the planes of minimum step-height

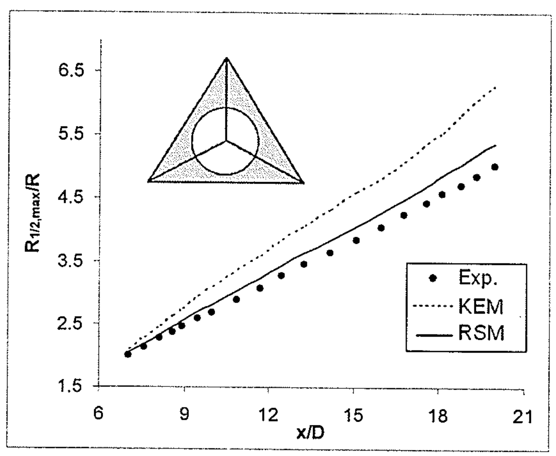

Figure 4.13: Development of jet half-velocity width in the planes of maximum step-height

Comparing Figures 4.12 and 4.13, one may note that for any given axial location, the jet half-velocity width in the plane of maximum step-height is higher than that in the plane of minimum step-height. It is clear that both models are capable of predicting this difference which is an indication of three-dimensionality of the flow. It is also interesting to notice that, in Figure 4.11, the *KEM* shows faster mean streamwise velocity decay along the jet centerline and exhibits higher values of the jet half-velocity width as shown in Figures 4.12-13. Similar to the results of the simulation of the triangular jet presented in the previous section, it is observed that the *KEM* predicts faster jet spreading.

4.2.2.2 Turbulence quantities

Figure 4.14 shows the radial profiles of the normalized measured and predicted streamwise turbulence intensity component along the jet centerline. Both tested models are able to predict the exact axial location of the turbulence intensity peak. However, the *KEM* overpredicts turbulence intensity values, which is an indication of a higher mixing rate, especially in the near-field. On the other hand, the streamwise turbulence intensity along the jet centerline is well predicted by the *RSM.*

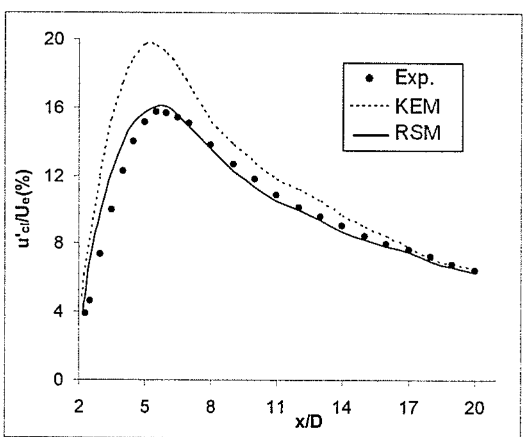

Figure 4.14: Evolution of the normalized streamwise turbulence intensity along the jet centerline

Chapter 5

CONCLUSIONS AND RECOMMENDATIONS

5.1 Conclusions

The following conclusions are drawn for each of the three flow cases simulated in the present thesis:

(A) Swirling jet in a can-combustor:

Simulation of turbulent swirling flows in an axisymmetric sudden expansion combustor has been performed for two different inlet swirl numbers (i.e. $S = 0.4$ and $S = 0.81$) in the same combustor geometry. The main conclusions are summarized below.

- In comparison with all the tested models, the standard *RSM* and the *SSG* produce the best predictions of the mean velocity profiles. The performance of the eddy-viscosity models in predicting the mean velocities is competetive. At low swirl numbers, both the *RSM* and the *SSG* predict reasonably accurate mean velocity profiles in comparison with their experimental counterparts. At high swirl numbers, however, these two models underpredict the profiles of the tangential mean velocity especially in the inner flow region.
- The CRZ in both flow configurations is predicted by all the tested models. Swirl intensity effect is significant in reducing the size of CRZ from four step heights, for $S=0.4$, to less than two-step heights, for $S=0.81$. It is found that all the employed turbulence models could predict the effect of swirl intensity on the axial location of the corner flow reattachment point. In the flow configuration with low swirl number, the predicted size of the CRZ by the *KEM* is the best in comparison with the experimental value. In the flow configuration with high swirl numbers,

S=0.81, the predicted size of the corner reverse flow region by all the models is in good agreement with the experimental data.

- It is found that all the models can predict the CTRZ in the strongly swirling flow, although with different sizes. But, in the weakly swirling flow, only the *RSM* and the *SSG* could predict the existence of the CTRZ in the flow field. In the weakly swirling flow, the predicted length (in the axial direction) of the CTRZ by the *RSM* and the *SSG* are around 40 percent shorter than that found experimentally, while they are 1.25 and 1.5 times wider (in the radial direction) than the measured width of the CTRZ. In the strongly swirling flow, it is found that both the *RSM* and the SSG predict reasonably accurate size of the CTRZ in comparison with the experimental value.
- Numerical predictions of the stress closures for the turbulence quantities are much more accurate than those obtained by using the eddy-viscosity models, especially in the near-field region where the flow is anisotropic. However, even the *RSM* and the *SSG* are inadequate for predicting the magnitude of the shear stresses especially in the mid-field whereas their trends are well captured. In the weakly swirling flow, among the eddy-viscosity models, the *RKEM* shows the most accurate predictions of the turbulence intensity components, while more accurate results of the Reynolds shear stresses can be obtained by employing the *KEM*. In the strongly swirling flow, the *RKEM* shows the best predictions of the turbulence quantities among the eddy-viscosity models.
- In summary, among the tested RANS turbulence models, the *SSG* model shows the most accurate results in predicting the main characteristics of swirling flow in

a can-combustor. However, its major handicap resides in its inability to capture accurately enough the flow characteristics near the centreline at high swirl intensities, as well as the magnitude of the Reynolds shear stresses in the near- and mid-field flow regions.

(B) Turbulent free jet issuing from an equilateral triangular orifice

Three-dimensional simulation of an equilateral triangular turbulent free jet has been performed for a Reynolds number of 1.84×10^5. The main conclusions are summarized as follows:

- All the tested models are able to capture the vena contracta effect. Among the eddy-viscosity models, the *RKEM* shows the best predictions of the streamwise mean velocity decay along the jet centerline. However, its results are less accurate than those of the *RSM* and the *SSG* in the jet's mid- and far-field. The *RSM* shows the best results in predicting this quantity.
- In comparison with all the tested models, the *RSM* produces the best predictions of the streamwise mean velocity profiles. Among the eddy-viscosity models, the *KEM* and the *RNG* show the best and the worst results, respectively, in predicting the streamwise mean velocity profiles. The predictions of the *RKEM* and the *SST* are competetive.
- Comparing the performance of the eddy-viscosity models in predicting the development of the jet half-velocity widths, it is found that the *KEM* and the *RKEM* show the best results in the central *x-y* and *x-z* planes, respectively. Again, the Reynolds stress models show much better results than do the eddy-viscosity models in predicting $Y_{1/2}$ and $Z_{1/2}$. The *KEM* and the *RNG* show the highest and

the lowest values of B_e in the region $x/D_e<20$, respectively. This is an indication of faster and slower mixing predicted by the *KEM* and the *RNG*, respectively.

- All the models, except the *KEM* and the *RNG*, are able to acceptably predict the streamwise local turbulence intensity. On the other hand, only the *RSM* and the *SSG* are capable of predicting reasonably well the experimental profiles of the spanwise and the lateral turbulence intensities.
- In summary, among the tested *RANS* turbulence models, the standard *RSM* shows the most accurate results in reproducing the experimental flowfield profiles of an equilateral triangular turbulent free jet. However, its only weakness is its inability to capture accurate enough the flatness of the streamwise mean velocity profile in the very near-field near the centreline of the central *x-y* plane.

(C) Turbulent free jet issuing from a circular nozzle with triangular collar

Three-dimensional simulation of a turbulent free jet issuing from a circular nozzle with triangular collar has been performed at a Reynolds number of 2.0×10^4. The trends seen in the combustor and the triangular orifice studies suggest that in these types of flow situations the standard *RSM* provides the best predictions in comparison with the experimental data. Therefore, for the jet issuing from a circular nozzle with triangular collar only the standard *RSM* and the standard *k-ε* model have been tested. The following conclusions are drawn:

- The *KEM* shows acceptable predictions of the streamwise mean velocity decay along the jet centerline. However, its results are less accurate than those of the *RSM*.

- The predictions of the jet half-velocity widths, i.e. $R_{1/2,min}$ and $R_{1/2,max}$, reveal that the *RSM* shows better results than do the *KEM*. It is also important to note that, for a given axial location, the jet half-velocity width in the plane of maximum step-height is higher than that in the plane of minimum step-height. Both models are able to capture this difference which is an indication of three-dimensionality of the flow.
- Both tested models are able to show the exact axial location of the turbulence intensity peak, but with different magnitudes. The *RSM* is much better and its predictions agree remarkably well with the measurements.
- As expected from the predictions of the *KEM* in the simulation of the jet issuing from a triangular orifice, the *KEM* predicts again a higher mixing rate, especially in the near-field of the jet issuing from a circular nozzle with triangular collar. On the other hand, the streamwise turbulence intensity along the jet centerline is well predicted by the *RSM* in comparison with the experiment.

In summary, it can be concluded that the standard Reynolds stress model (*RSM*) has the ability of predicting the overall flowfield features for all flow configurations studied in this thesis. However, its degree of accuracy can be different depending on the flow configurations being simulated. Finally, as a result of the present study, it can be concluded that the performance of the RANS turbulence models is problem-dependent and none of the models is expected to perform well for all flow configurations.

5.2 Recommendations for Further Work

The following recommendations are proposed for future work:

- For the circular jet with triangular collar, the effect of triangular collar size, i.e. equivalent diameter and length, on the flowfield can be investigated numerically.
- Swirling flows can be introduced into the non-circular geometries to study the flowfield of a swirling flow issuing from a non-circular geometry.
- The results of the present work show that the standard *RSM* is capable of accurately capturing the most important flow features in all the flow cases studied here. Therefore, this model is recommended for simulating turbulent flows issuing from asymmetric nozzles with or without sudden expansion to help interpreting the experimental data obtained in the **Energy and Combustion Laboratory** in the department of mechanical and manufacturing engineering at the University of Manitoba.

Appendix A

THE FLUENT SOLVER

To solve the governing equations of the flows described in chapters 3 and 4, the commercial software FLUENT, version 6.1.22, is used. In this code, finite volume formulation is employed. Details about the solver algorithms used by FLUENT are provided in [41], however, an overview of the methods used in the present study is provided below.

Both *segregated solver* and *coupled solver* are available in FLUENT. Depending on the selected method, FLUENT solves the governing integral equations for the conservation of mass and momentum, including the selected turbulence closure model equations. In both cases the domain is divided into discrete control volumes by using a computational grid. Then, the governing equations are integrated on the individual control volumes to construct algebraic equations for the discrete dependent variables (unknowns) such as velocities, pressure, etc. Finally, the discretized equations are linearized and the resultant linear equation system is solved to yield updated values of the dependent variables. The aforementioned two numerical methods employ a similar discretization process (finite-volume), but the approach used to linearize and solve the discretized equations is different (*Implicit* or *Explicit*). Details are provided below.

Segregated Solver

In the present work, the segregated solution method together with the implicit linearization method is used. Using the segregated solver, the governing equations are solved sequentially. Because the governing equations are non-linear and coupled, several iterations must be performed before a converged solution is obtained. The following diagram is an overview of the segregated solution method:

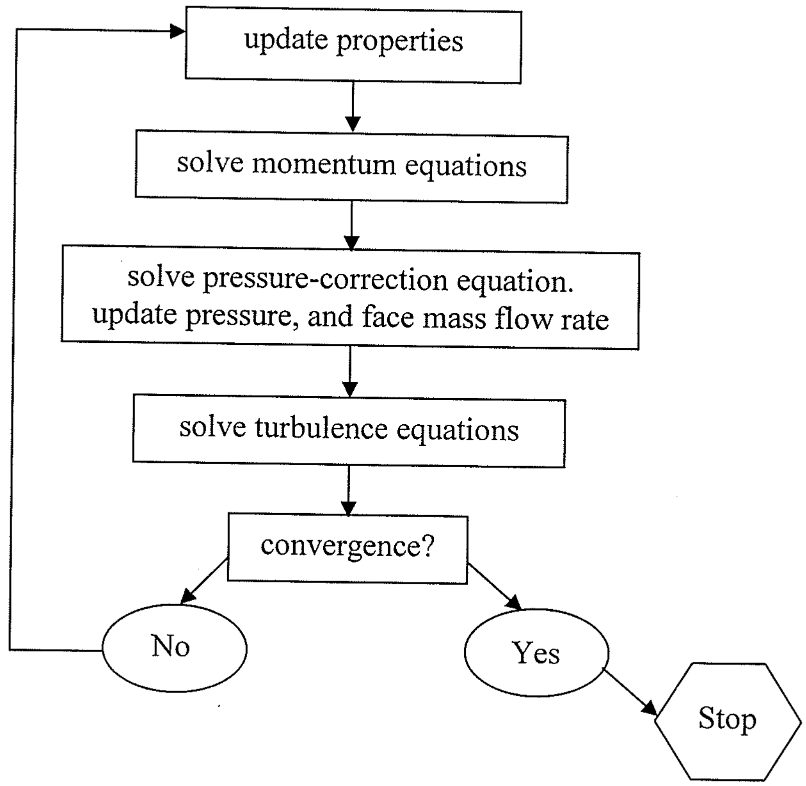

Figure A.1: Overview of the segregated solution method

Implicit Linearization

In the implicit linearization method, for a given variable, the unknown value in each cell is computed using a relation that includes both existing and unknown values from neighbouring cells. Therefore each unknown will appear in more than one equation in the system, and these equations must be solved simultaneously to give the unknown quantities.

Discretization

FLUENT uses a control-volume-based technique to convert the governing equations to algebraic equations that can be solved numerically. This method consists of integrating the governing equations about each control volume, yielding discrete equations that conserve each quantity on a control-volume basis. Discretization of the governing equations can be illustrated most easily by considering the steady-state conservation equation for transport of a scalar quantity Φ. This is demonstrated by the following equation written in integral form for an arbitrary control volume V as follows

$$\oint \rho\phi\vec{\upsilon}.d\vec{A} = \oint \Gamma_{\phi}\nabla_{\phi}.d\vec{A} + \int_{V} S_{\phi}dV \qquad \text{(A-1)}$$

where

ρ	=	density
$\vec{\upsilon}$	=	velocity vector
$\vec{A}$	=	surface area vector
Γ_{Φ}	=	diffusion coefficient for Φ
$\nabla\Phi$	=	gradient of Φ
S_{Φ}	=	source of Φ per unit volume

Eq. (A-1) is applied to each control volume, or cell, in the computational domain. The two-dimensional, triangular cell shown in Figure A.2 is an example of such a control volume.

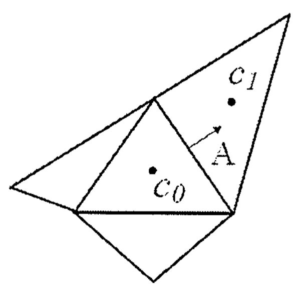

Figure A.2: Control volume used to illustrate the discretization of a transport equation

Discretization of Eq. (A-1) on a given cell yields

$$\sum_{f}^{N_{face}} \rho_f \vec{\upsilon}_f \phi_f.\vec{A}_f = \sum_{f}^{N_{face}} \Gamma_{\phi}(\nabla\Phi)_n.\vec{A}_f + S_{\phi}V \qquad \text{(A-2)}$$

where

f	=	any face in the computational domain
N_{faces}	=	number of faces enclosing cell
Φ_f	=	value of Φ convected through face f

$\rho_f \vec{v}_f . \vec{A}_f$	=	mass flux through the face
$\vec{A}_f$	=	area of face f
$(\nabla\Phi)_n$	=	magnitude of $\nabla\Phi$ normal to face f
V	=	cell volume

Each transport equation is discretized into algebraic form. For a given cell, p:

$$\frac{(\rho\phi_p)^{t+\Delta t} - (\rho\phi_p)^t}{\Delta t}\Delta V + \sum_{faces} \rho_f \phi_f V_f A_f = \sum_{faces} \Gamma_f (\nabla\phi)_{\perp,f} A_f + S_\phi \Delta V \qquad \text{(A-3)}$$

Discretized equations require information at cell centers and faces. Field data (material properties, velocities, etc.) are stored at cell centers. Face values can be expressed in terms of local and adjacent cell values. The discretized equation can be expressed simply as

$$a_p \phi_p + \sum_{nb} a_{nb} \phi_{nb} = b_p \qquad \text{(A-4)}$$

This equation is written for every control volume in domain resulting in a set of algebraic equations. The equation sets are solved iteratively. Coefficients a_p, a_{nb} depend upon the solution and are updated at each iteration. *Linearization* is removing coefficients' dependencies on Φ and *de-coupling* is removing coefficients' dependencies on other solution variables.

By default, FLUENT stores discrete values of the scalar Φ at the cell centers. Face values, Φ_f, which are required for the convection terms in Eq. (A-2) must be interpolated from the cell center values. To do this, an upwind scheme is used. Upwinding means that the face value Φ_f is derived from quantities in the cell upstream relative to the direction of the normal velocity v_n in Eq. (A-2). Several upwind schemes are available in FLUENT: first-order upwind, second-order upwind, power law, and QUICK. In the present study, the QUICK [150] scheme is used for the convection terms in all transport equations. The diffusion terms in Eq. (A-2) are central-differenced and are always second-order accurate.

For quadrilateral meshes (used in the second and third flow cases in this thesis) and hexahedral meshes (used in the first flow case in this thesis) the QUICK scheme is available in FLUENT for computing a higher-order value of the convected variable Φ at a face.

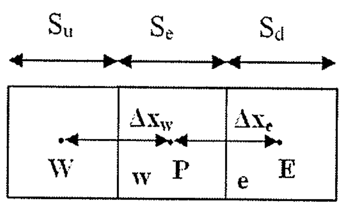

Figure A.3: One-dimensional control volume

QUICK scheme is based on a weighted average of second-order-upwind and central interpolations of the variable. For the face "*e*" in Figure A.3, if the flow is from left to right, such a value can be written as

$$\phi_e = \theta\left[\frac{S_d}{S_c + S_d}\phi_P + \frac{S_c}{S_c + S_d}\phi_E\right] + (1-\theta)\left[\frac{S_u + 2S_c}{S_u + S_c}\phi_P - \frac{S_c}{S_u + S_c}\phi_W\right] \tag{A-5}$$

$\theta=1$, $\theta=0$, and $\theta=1/8$ in the above equation result in a central second-order interpolation, a second-order upwind value, and the traditional QUICK scheme, respectively. The implementation in FLUENT uses a variable, solution-dependent value of θ, chosen so as to avoid introducing new solution extrema.

Discretization of the Momentum Equation

The discretization scheme described for a scalar quantity Φ is used to discretize the momentum equations. For example, the x-momentum equation can be obtained by setting $\Phi=u$ in Eq. (A-4)

$$a_p u = \sum a_{nb} u_{nb} + \sum p_f A \hat{i} + S \tag{A-6}$$

If the pressure field and face mass fluxes were known, Eq. (A-6) could be solved in the manner outlined above, and a velocity field obtained. However, the pressure field and face mass fluxes are not known a priori and must be obtained as a part of the solution. FLUENT uses a co-located scheme, whereby pressure and velocity are both stored at cell centers. However, Eq. (A-6) requires the value of the pressure at the face between cells c_0 and c_1, shown in Figure A.2. Therefore, an interpolation scheme is required to compute the face values of pressure from the cell values. In the present work, the PRESTO [41] method is used for the pressure discretization. The PRESTO (PREssure STaggering Option) scheme uses the discrete continuity balance for a "staggered" control volume about the face to compute the "staggered" (i.e., face) pressure. This procedure is similar in spirit to the staggered-grid schemes used with structured meshes.

Pressure-Velocity Coupling

The discrete continuity equation is achieved by integrating the steady-state continuity equation over the control volume in Figure A.2

$$\sum_{f}^{N_{faces}} J_f A_f = 0 \tag{A-7}$$

where J_f is the mass flux through face f.

In the sequential procedure of solving the momentum and continuity equations, the continuity equation is used as an equation for pressure. However, since density is not directly related to pressure in incompressible flows, pressure does not appear explicitly in Eq. (A-7). The SIMPLE family of algorithms [153] is used for introducing pressure into the continuity equation [41]. In other words, pressure-velocity coupling is achieved by deriving an equation for pressure from the discrete continuity equation. As mentioned before, *de-coupling* is removing coefficients' dependencies on other solution variables in their discretized equation (Eq. A-4). The SIMPLE, SIMPLEC, and PISO pressure-velocity coupling methods are available in FLUENT. In the present work, the PISO [149] method is applied for the pressure-velocity coupling. The Pressure-Implicit with Splitting of Operators (PISO) pressure-velocity coupling scheme, part of the SIMPLE family of algorithms, is based on the higher degree of the approximate relation between the corrections for pressure and velocity. Details of this method can be found in [41, 149].

Residuals

Transport equation for any given quantity, Φ, can be written as

$$a_p\phi_p + \sum_{nb} a_{nb}\phi_{nb} = b_p \tag{A-8}$$

At the start of each iteration, the above equality will not hold. The imbalance is called the residual, R_p, which is defined as follows

$$R_p = a_p\phi_p + \sum_{nb} a_{nb}\phi_{nb} - b_p \tag{A-9}$$

The monitored residuals are summed over all cells

$$R = \sum_{cells} | R_p | \tag{A-10}$$

The residual should become negligible as iterations increase. When all the residuals are less than the convergence criteria, the solution is converged.

Appendix B

WALL FUNCTION

A two-layer-based, non-equilibrium wall function [148] is used near the wall for all the flow cases studied in the present thesis. In this model, the Launder and Spalding's log-law [138] for mean velocity is sensitized to pressure-gradient effects and it is assumed that the wall-neighboring cells consist of a viscous sublayer and a fully turbulent layer [41].

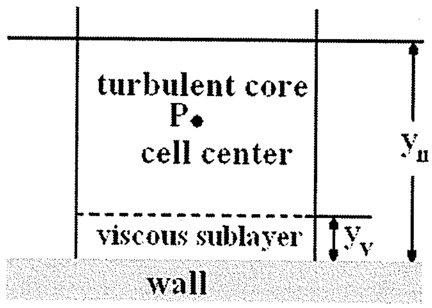

Figure B.1: Non-equilibrium wall function

The log-law for mean velocity sensitized to pressure gradients is:

$$\frac{\tilde{U}C_{\mu}^{1/4}k^{1/2}}{\tau_{\omega}/\rho}=\frac{1}{\kappa}\ln\left(E\frac{\rho C_{\mu}^{1/4}k^{1/2}y}{\mu}\right) \qquad \text{(B-1)}$$

where:

$$\tilde{U}=U-\frac{1}{2}\frac{dp}{dx}\left[\frac{y_v}{\rho\kappa\sqrt{k}}\ln\left(\frac{y}{y_v}\right)+\frac{y-y_v}{\rho\kappa\sqrt{k}}+\frac{y_v^2}{\mu}\right] \qquad \text{(B-2)}$$

In Eq. (B-1), E is an empirical constant, and k_p is turbulence kinetic energy at point p.

The following assumptions are made in non-equilibrium wall function [41]:

$$\tau_t=\begin{cases}0 & y<y_v\\ \tau_w & y>y_v\end{cases} \qquad k=\begin{cases}(\frac{y}{y_v})^2 k_P & y<y_v\\ k_P & y>y_v\end{cases} \qquad \varepsilon=\begin{cases}\frac{2\nu k}{y^2} & y<y_v\\ \frac{k^{3/2}}{C_l y} & y>y_v\end{cases} \qquad \text{(B-3)}$$

where $C_l = \kappa C_\mu^{-3/4}$ and y_v, the dimensional thickness of the viscous sublayer, is defined as:

$$y_v = \frac{\mu y_v^*}{\rho C_\mu^{1/4} k_P^{1/2}} \tag{B-4}$$

where $y_v^* = 11.225$

The wall-adjacent cell's centroid is located within the region $30 < y^+ < 100$.

REFERENCES

1. Launder, B.E. and Spalding, D.B. (1972) *Lectures in Mathematical Models of Turbulence*, London, UK: Academic Press.

2. Jones, W.P. and Launder, B.E. (1972) 'The prediction of laminarization with a two-equation model of turbulence', *International Journal of Heat and Mass Transfer*, Vol. 15, No. 2, pp.301-314.

3. Speziale, C.G. (1987) 'On nonlinear *k-l* and *k-ε* models of turbulence', *Journal of Fluid Mechanics*, Vol. 178, pp.459-475.

4. Chien, K.Y. (1982) 'Prediction of channel and boundary layer flows with a low-Reynolds-number turbulence model', *AIAA Journal*, Vol. 20, No. 1, pp.33-38.

5. Rodi, W. (1988) 'Recent developments in turbulence modeling', in Iwasa, Y., Tamai, N. and Wada, A. (Eds.): *Proceedings of the 3rd International Symposium on Refined Flow Modeling and Turbulence Measurements*, Tokyo, Japan.

6. Hogg, S. and Leschziner, M.A. (1989) 'Computation of highly swirling confined flow with a Reynolds stress turbulence model', *AIAA Journal*, Vol. 27, No. 1, pp.57-63.

7. Jones, W.P. and Pascau, A. (1989) 'Calculation of confined swirling flows with a second moment closure', *Journal of Fluids Engineering*, Vol. 111, No. 3, pp.248-255.

8. Sharif, M.A.R. and Wong, Y.K.E. (1995) 'Evaluation of the performance of three turbulence closure models in the prediction of confined swirling flows', *Computers and Fluids*, Vol. 24, No. 1, pp.81-100.

9. Chen, J.C. and Lin, C.A. (1999) 'Computations of strongly swirling flows with second-moment closures', *International Journal for Numerical Methods in Fluids*, Vol. 30, No. 5, pp.493-508.

10. Yaras, M.I. and Grosvenor, A.D. (2003) 'Evaluation of one- and two-equation low-Re turbulence models. Part I-Axisymmetric separating and swirling flows', *International Journal for Numerical Methods in Fluids*, Vol. 42, No. 12, pp.1293-1319.

11. Yang, X. and Ma, H. (2003) 'Computation of strongly swirling confined flows with cubic eddy-viscosity turbulence models', *International Journal for Numerical Methods in Fluids*, Vol. 43, No. 12, pp.1355-1370.

12. Nejad, A.S., Vanka, S.P., Favaloro, S.C., Samimy, M. and Langenfeld, C. (1989) 'Application of laser velocimetry for characterization of confined swirling flow', *Journal of Engineering for Gas Turbines and Power*, Vol. 111, No. 1, pp.36-45.

13. Weber, R., Visser, B.M. and Boysan, F. (1990) 'Assessment of turbulence modeling for engineering prediction of swirling vortices in the near burner zone', *International Journal of Heat and Fluid Flow*, Vol. 11, No. 3, pp.225-235.

14. Favaloro, S.C., Nejad, A.S. and Ahmed, S.A. (1991) 'Experimental and computational investigation of isothermal swirling flow in an axisymmetric dump combustor', *Journal of Propulsion and Power*, Vol. 7, No. 3, pp.348-356.

15. McGuirk, J.J. and Palma, J.M.L.M. (1993) 'The flow inside a model gas turbine combustor: Calculations', *Journal of Engineering for Gas Turbines and Power, Transactions of the ASME*, Vol. 115, No. 3, pp.594-602.

16. Zhu, J. and Shih, T.H. (1994) 'Computation of confined coflow jets with three turbulence models', *International Journal for Numerical Methods in Fluids*, Vol. 19, No. 10, pp.939-956.

17. Lin, C.A. and Lu, C.M. (1994) 'Modeling three-dimensional gas-turbine combustor model flow using second-moment closure', *AIAA Journal*, Vol. 32, No. 7, pp.1416-1422.

18. Tsai, J.H., Lin, C.A. and Lu, C.M. (1995) 'Modeling dump combustor flows with and without swirl at the inlet using Reynolds stress models', *International Journal of Numerical Methods for Heat and Fluid Flow*, Vol. 5, No. 7, pp.577-588.

19. Xia, J.L., Yadigaroglu, G., Liu, Y.S., Schmidli, J. and Smith, B.L. (1998) 'Numerical and experimental study of swirling flow in a model combustor', *International Journal of Heat and Mass Transfer*, Vol. 41, No. 11, pp.1485-1497.

20. Lei, Y., Zhang, J. and Zhou, L. (2000) 'Simulation of swirling turbulent flows of coaxial jets in a combustor', *Numerical Heat Transfer, Part A (Applications)*, Vol. 37, No. 2, pp.189-199.

21. Engdar, U. and Klingmann, J. (2002) 'Investigation of two-equation turbulence models applied to a confined axis-symmetric swirling flow', *ASME, Pressure Vessels and Piping Division (Publication) PVP*, Vol. 448, No. 2, pp.199-206.

22. Flohr, P., Schmitt, P. and Paschereit, C.O. (2002) 'Mixing field analysis of a gas turbine burner', *ASME, Fuels and Combustion Technologies Division (Publication) FACT*, pp.45-53.

23. Jakirlic, S., Hanjalic, K. and Tropea, C. (2002) 'Modeling rotating and swirling turbulent flows: A perpetual challenge', *AIAA Journal*, Vol. 40, No. 10, pp.1984-1996.

24. Wei, X., Zhang, J. and Zhou, L. (2004) 'A new algebraic mass flux model for simulating turbulent mixing in swirling flow', *Numerical Heat Transfer, Part B (Fundamentals)*, Vol. 45, No. 3, pp.283-300.

25. Zhang, J., Lei, Y. and Zhou, L. (2004) 'Simulation of coaxial jet interactions in a swirl combustor', *Combustion Science and Technology*, Vol. 176, No. 1, pp.23-43.

26. Huang, Y.N., Ma, H.Y. and Chu, H.J. (2006) 'Modeling turbulent swirling flows based on the algebraic two-equation (k-ε) approach', *International Journal for Numerical Methods in Fluids*, Vol. 51, No. 3, pp.285-304.

27. Habisreuther, P., Bender, C., Petsch, O., Buchner, H. and Bockhorn, H. (2006) 'Prediction of pressure oscillations in a premixed swirl combustor flow and comparison to measurements', *Flow, Turbulence and Combustion*, Vol. 77, No. 1-4, pp.147-160.

28. Tsao, J.M. and Lin, C.A. (1999) 'Reynolds stress modelling of jet and swirl interaction inside a gas turbine combustor', *International Journal for Numerical Methods in Fluids*, Vol. 29, No. 4, pp.451-464.

29. So, R.M., Ahmed, S.A. and Mongia, H.C. (1984) 'An experimental investigation of gas jets in confined swirling air flow', *NASA CR 3832*.

30. Bradshaw, P., Launder, B.E. and Lumley, J.L. (1996) 'Collaborative testing of turbulence models', *Journal of Fluids Engineering*, Vol. 118, No. 2, pp.243-247.

31. Launder, B.E., Priddin, C.H. and Sharma, B.I. (1977) 'The calculation of turbulent boundary layers on spinning and curved surfaces', *Journal of Fluids Engineering*, Vol. 99, No. 1, pp.231-239.

32. Chen, C.P. (1986) 'Multiple-scale turbulence model in confined swirling jet predictions', *AIAA Journal*, Vol. 24, No. 10, pp.1717-1719.

33. Smoot, L.D. and Smith, P.J. (1985) *Coal Combustion and Gasification*, NewYork, USA: Plenum Press.

34. Hwang, C.C., Zhu, G., Massoudi, M. and Ekmann, J.M. (1993) 'Comparison of the linear and the nonlinear k-ε turbulence models in combustors', *Journal of Fluids Engineering*, Vol. 115, No. 1, pp.93-102.

35. Kitoh, O. (1991) 'Experimental study of turbulent swirling flow in a straight pipe', *Journal of Fluid Mechanics*, Vol. 225, pp.445-479.

36. Yakhot, V., Orszag, S.A., Thangam, S., Gatski, T.B. and Speziale, C.G. (1992) 'Development of turbulence model for shear flows by a double expansion technique', *Physics of Fluids A (Fluid Dynamics)*, Vol. 4, No. 7, pp.1510-1520.

37. Orszag, S.A., Yakhot, V., Flannery, W.S., Boysan, F., Choudhury, D., Maruszewski, J. and Patel, B. (1993) 'Renormalization group modeling and turbulence simulations', *Proceedings of the International Conference on Near-Wall Turbulent Flows*, Tempe, AZ, USA, pp.1031-1046.

38. Papageorgakis, G.C. and Assanis, D.N. (1999) 'Comparison of linear and nonlinear RNG-based k-ε models for incompressible turbulent flows', *Numerical Heat Transfer, Part B (Fundamentals)*, Vol. 35, No. 1, pp.1-22.

39. Hanjalic, K. (1994) 'Advanced turbulence closure models: A view of current status and future prospects', *International Journal of Heat and Fluid Flow*, Vol. 15, No. 3, pp.178-203.

40. Shih, T.H., Liou, W.W., Shabbir, A., Yang, Z. and Zhu, J. (1995) 'A new k-ε eddy-viscosity model for high Reynolds number turbulent flows', *Computers and Fluids*, Vol. 24, No. 3, pp.227-238.

41. FLUENT User's Guide (2005), *Fluent Inc.*, Lebanon NH 03766, USA.

42. Menter, F.R. (1994) 'Two-equation eddy-viscosity turbulence models for engineering applications', *AIAA Journal*, Vol. 32, No. 8, pp.1598-1605.

43. Boysan, F. and Swithenbank, J. (1981) 'Numerical prediction of confined vortex flows', *Proceedings of the 2nd International Conference on Numerical Methods in Laminar and Turbulent Flow*, Venice, Italy, pp.425-437.

44. Fu, S., Huang, P.G., Launder, B.E. and Leschziner, M.A. (1988) 'A comparison of algebraic and differential second-moment closures for axisymmetric turbulent shear flows with and without swirl', *Journal of Fluids Engineering*, Vol. 110, No. 2, pp.216-221.

45. Zhang, J., Nieh, S. and Zhou, L. (1992) 'A new version of algebraic stress model for simulating strongly swirling turbulent flows', *Numerical Heat Transfer, Part B (Fundamentals)*, Vol. 22, No. 1, pp.49-62.

46. Zhang, J., Lu, H., Zhou, L. and Nieh, S. (1997) 'Simulation of annular swirling turbulent flows with a new algebraic Reynolds stress model', *Numerical Heat Transfer, Part B (Fundamentals)*, Vol. 31, No. 2, pp.235-249.

47. Launder, B.E., Reece, G.J. and Rodi, W. (1975) 'Progress in the development of a Reynolds-stress turbulence closure', *Journal of Fluid Mechanics*, Vol. 68, pp.537-566.

48. Hogg, S. and Leschziner, M.A. (1989) 'Second moment closure calculation of strongly swirling confined flow with large density gradients', *International Journal of Heat and Fluid Flow*, Vol. 10, No. 1, pp.16-27.

49. Ohtsuka, M. (1995) 'Numerical analysis of swirling non-reacting and reacting flows by the Reynolds stress differential method', *International Journal of Heat and Mass Transfer*, Vol. 38, No. 2, pp.331-337.

50. Lu, P. and Semiao, V. (2003) 'A new second-moment closure approach for turbulent swirling confined flows', *International Journal for Numerical Methods in Fluids*, Vol. 41, No. 2, pp.133-150.

51. Jones, L.N., Gaskeli, P.H., Thompson, H.M., Gu, X.J. and Emerson, D.R. (2005) 'Anisotropic, isothermal, turbulent swirling flow in a complex combustor geometry', *International Journal for Numerical Methods in Fluids*, Vol. 47, No. 10-11, pp.1053-1059.

52. Jawarneh, A.M. and Vatistas, G.H. (2006) 'Reynolds stress model in the prediction of confined turbulent swirling flows', *Journal of Fluids Engineering*, Vol. 128, No. 6, pp.1377-1382.

53. Palm, R., Grundmann, S., Weismuller, M., Saric, S., Jakirlic, S. and Tropea, C. (2006) 'Experimental characterization and modelling of inflow conditions for a gas turbine swirl combustor', *International Journal of Heat and Fluid Flow*, Vol. 27, No. 5, pp.924-936.

54. Launder, B.E. and Morse, A. (1979) 'Numerical prediction of axisymmetric free shear flows with a Reynolds stress turbulence closure', in Bradbury, L.J.S., Durst, F., Launder, B.E., Schmidt, F.W. and Whitelaw, J.H. (Eds.): *Turbulent Shear Flows*, Vol. 1, pp.279-294.

55. Lockwood, F.C. and Shen, B. (1994) 'Performance predictions of pulverized-coal flames of power station furnace and cement kiln types', *Proceedings of the Combustion Institute*, Vol. 25, pp.503-509.

56. Lu, P., Ye, T., Costa, M., Semiao, V. and Carvalho, M.G. (1999) 'Prediction with a second moment closure turbulence model and experiments of combined combustion of pulverized coal and propane in a semi-industrial combustor', *Proceedings of the 4th International Symposium on Coal Combustion*, Beijing, China, pp.356-367.

57. Hanjalic, K. (1999) 'Second-moment turbulence closure for CFD: Need and prospects', *International Journal of Computational Fluid Dynamics*, Vol. 12, pp.67-97.

58. Lumley, J.L. and Khajeh-Nouri, B.J. (1974) 'Computational modelling of turbulent transport', *Advances in Geophysics*, Vol. 18A, pp.169-192.

59. Speziale, C.G., Sarkar, S. and Gatski, T.B. (1991) 'Modelling the pressure-strain correlation of turbulence: An invariant dynamical systems approach', *Journal of Fluid Mechanics*, Vol. 227, pp.245-272.

60. Basara, B. and Younis, B.A. (1995) 'Assessment of the SSG pressure-strain model in two-dimensional turbulent separated flows', *Applied Scientific Research*, Vol. 55, No. 1, pp.39-61.

61. Younis, B.A., Gatski, T.B. and Speziale, C.G. (1996) 'Assessment of the SSG pressure-strain model in free turbulent jets with and without swirl', *Journal of Fluids Engineering*, Vol. 118, No. 4, pp.800-809.

62. Ahmed, S.A. and Nejad, A.S. (1992) 'Swirl effects on confined flows in axisymmetric geometries', *Journal of Propulsion and Power*, Vol. 8, No. 2, pp.339-345.

63. Ahmed, S.A. and Nejad, A.S. (1992) 'Velocity measurements in a research combustor - Part1: Isothermal swirling flow', *Experimental Thermal and Fluid Science*, Vol. 5, No. 2, pp.162-174.

64. Habib, M.A. and Whitelaw, J.H. (1980) 'Velocity characteristics of confined coaxial jets with and without swirl', *Journal of Fluids Engineering*, Vol. 102, No. 1, pp.47-53.

65. Baoyu, G., Langrish, T.A.G. and Fletcher, D.F. (2001) 'Simulation of turbulent swirl flow in an axisymmetric sudden expansion', *AIAA Journal*, Vol. 39, No. 1, pp.96-102.

66. Wang, P., Bai, X.S., Wessman, M. and Klingmann, J. (2004) 'Large eddy simulation and experimental studies of a confined turbulent swirling flow', *Physics of Fluids*, Vol. 16, No. 9, pp.3306-3324.

67. Ahmed, S.A., Al-Garni, A.Z. and Abidogun, K.B. (1999) 'The flowfield characteristics of a confined highly swirling turbulent flow', *Canadian Aeronautics and Space Journal*, Vol. 45, No. 4, pp.323-334.

68. Quinn, W.R. (2005) 'Near-field measurements in an equilateral triangular turbulent free jet', *AIAA Journal*, Vol. 43, No. 12, pp. 2574-2585.

69. Quinn, W.R. (2005) 'Measurements in the near flow field of an isosceles triangular turbulent free jet', Experiments in Fluids, Vol. 39, No. 1, pp. 111-126.

70. Schadow, K.C., Gutmark, E., Parr, D.M. and Wilson, K.J. (1988) 'Selective control of flow coherence in triangular jets', Experiments in Fluids, Vol. 6, No. 2, pp. 129-135.

71. Sforza, P.M., Steiger, M.H. and Trentacoste, N. (1966) 'Studies on three-dimensional viscous jets', *AIAA Journal*, Vol. 4, No. 5, pp. 800-806.

72. Gutmark, E., Schadow, K.C., Parr, D.M., Harris, C.K. and Wilson, K. J. (1985) 'The Mean and Turbulent Structure of Noncircular Jets', *AIAA Paper*, 10p.

73. Gutmark, E., Schadow, K.C., Parr, T.P., Hanson-Parr, D.M. and Wilson, K. J. (1989) 'Noncircular jets in combustion systems', *Experiments in Fluids*, Vol. 7, pp. 248-258.

74. Gutmark, E., Schadow, K.C. and Wilson, K.J. (1991) 'Subsonic and supersonic combustion using noncircular injectors', *Journal of Propulsion and Power*, Vol. 7, No. 2, pp. 240-249.

75. Quinn, W.R. (1990) 'Mean flow and turbulence measurements in a triangular turbulent free jet', *International Journal of Heat and Fluid Flow*, Vol. 11, No. 3, pp. 220-224.

76. Vandsburger, U. and Ding, C. (1995) 'Spatial modulation of a forced triangular jet', *Experiments in Fluids*, Vol. 18, No. 4, pp. 239-248.

77. Mi, J., Nathan, J. and Luxton, R.E. (2000) 'Centreline mixing characteristics of jets from nine differently shaped nozzles', *Experiments in Fluids*, Vol. 28, No. 1, pp. 93-94.

78. Quinn, W.R. (2005) 'Phase-averaged measurements in an isosceles triangular turbulent free jet', *Experiments in Fluids*, Vol. 39, pp. 941-943.

79. Mi, J., Deo, R.C. and Nathan, G.J. (2005) 'Characterization of turbulent jets from high-aspect-ratio rectangular nozzles', *Physics of Fluids*, Vol. 17, No. 6, pp. 068102:1-4.

80. Zaman, K.B.M.Q. (1999) 'Spreading characteristics of compressible jets from nozzles of various geometries', *Journal of Fluid Mechanics*, Vol. 383, pp. 197-228.

81. Zaman, K.B.M.Q. (1996) 'Axis switching and spreading of an asymmetric jet: the role of coherent structure dynamics', *Journal of Fluid Mechanics*, Vol. 316, pp. 1-27.

82. Quinn, W.R. (1995) 'Turbulent mixing in a free jet issuing from a low aspect ratio contoured rectangular nozzle', *Aeronautical Journal*, Vol. 99, No. 988, pp. 337-342.

83. Liu, H. and Wu, S. (1995) 'Enhanced mixing of 2D lobed nozzles', *Proceedings of the International Gas Turbine and Aeroengine Congress and Exposition*, ASME 95-GT–339.

84. Zaman, K.B.M.Q. (1995) 'Dynamics of large scale vortices in an asymmetric jet', *Proceedings of the 1995 ASME/JSME Fluids Engineering and Laser Anemometry Conference and Exhibition*, Vol. 214, High Speed Jet Flows, pp. 65-70.

85. Zaman, K.B.M.Q. (1995) 'Spreading characteristics and thrust of jets from asymmetric nozzles', *NASA Technical Memorandum*, No. 107132, pp. 1-19.

86. Quinn, W.R. (1994) 'Development of a large-aspect-ratio rectangular turbulent free jet', *AIAA Journal*, Vol. 32, No. 3, pp. 547-554.

87. Rice, E.J. and Raman, G. (1993) 'Supersonic jets from bevelled rectangular nozzles', *Proceedings of the ASME Winter Conference, 93-WA/NCA-26*, pp. 1-7.

88. Quinn, W.R. (1992) 'Turbulent free jet flows issuing from sharp-edged rectangular slots. The influence of slot aspect ratio', *Experimental Heat Transfer*, Vol. 5, No. 2, pp. 203-215.

89. Quinn, W.R. (1992) 'Streamwise evolution of a square jet cross section', *AIAA Journal*, Vol. 30, No. 12, pp. 2852-2857.

90. Grandmaison, E.W., Pollard, A. and Ng, S. (1991) 'Scalar mixing in a free, turbulent rectangular jet', *International Journal of Heat and Mass Transfer*, Vol. 34, No. 10, pp. 2653-2662.

91. Quinn, W.R. (1991) 'Effects of slot aspect ratio on turbulent free jet flows issuing from sharp-edged rectangular slots', *Proceedings of the World Conference on Experimental Heat Transfer, Fluid Mechanics, and Thermodynamics*, pp. 170-177.

92. Quinn, W.R. (1991) 'Passive near-field mixing enhancement in rectangular jet flows', *AIAA Journal*, Vol. 29, No. 4, pp. 515-519.

93. Gutmark, E., Schadow, K.C. and Wilson, K.J. (1989) 'Noncircular jet dynamics in supersonic combustion', *Journal of Propulsion and Power*, Vol. 5. No. 5, pp. 529-533.

94. Tsuchiya, Y., Horikoshi, C., Sato, T. and Takahashi, M. (1989) 'A study on the spread of rectangular jets. The mixing layer near the jet exit and visualization by the dye method', *JSME International Journal, Series II (Fluids Engineering, Heat Transfer, Power, Combustion, Thermophysical Properties)*, Vol. 32, No. 1, pp. 11-18.

95. Tsuchiya, Y., Horikoshi, C. and Sato, T. (1986) 'On the spread of rectangular jets', *Experiments in Fluids*, Vol. 4, No. 4, pp. 197-204.

96. Quinn, W.R., Pollard, A. and Marsters, G.F. (1985) 'Mean velocity and static pressure distributions in a three-dimensional turbulent free jet', *AIAA Journal*, Vol. 23, No. 6, pp. 971-973.

97. Quinn, W. R., Pollard, A. and Marsters, G. F. (1983) 'On "saddle-backed" velocity distributions in three-dimensional turbulent free jets', *Proceedings of the AIAA 16th Fluid and Plasma Dynamics Conference, Danvers, MA*, pp. 1677-1682.

98. Krothapalli, A., Baganoff, D. and Karamcheti, K. (1981) 'On the mixing of a rectangular jet', *Journal of Fluid Mechanics*, Vol. 107, pp. 201-220.

99. Sfeir, A.A. (1979) 'Investigation of three-dimensional turbulent rectangular jets', *AIAA Journal*, Vol. 17, No. 10, pp. 1055-1060.

100. Marsters, G.F. (1981) 'Spanwise velocity distributions in jets from rectangular slots', *AIAA Journal*, Vol. 19, No. 2, pp. 148-152.

101. Sfeir, A.A. (1976) 'The velocity and temperature fields of rectangular jets', *International Journal of Heat and Mass Transfer*, Vol. 19, No. 11, pp. 1289-1297.

102. Kambe, T. and Takao, T. (1971) 'Motion of distorted vortex rings', *Journal of the Physical Society of Japan*, Vol. 31, No. 2, pp. 591-599.

103. Trentacoste, N. and Sforza, P. (1967) 'Further Experimental Results for Three-Dimensional Free Jets', *AIAA Journal*, Vol 5, No 5, pp. 885-891.

104. Miller, R.S., Madnia, C.K. and Givi, P. (1995) 'Numerical simulation of non-circular jets', *Computers & Fluids*, Vol. 24, No. 1, pp. 1-25.

105. Berg, J.R., Ormiston, S.J. and Soliman, H.M. (2006) 'Prediction of the flow structure in a turbulent rectangular free jet', *International Communications in Heat and Mass Transfer*, Vol. 33, pp. 552-563.

106. de With, G. and Holdo, A.E. (2005) 'The use of turbulent inflow conditions for the modelling of a high aspect ratio jet', *Fluid Dynamics Research*, Vol. 37, No. 6, pp. 443-461.

107. Holdo, A.E. and de With, G. (2004) 'The use of turbulent inlet boundary conditions for the modelling of high aspect ratio free jets', *2004 ASME Heat Transfer/Fluids Engineering Summer Conference*, Vol. 2, pp. 1325-1331.

108. Rembold, B., Adams, N.A. and Kleiser, L. (2002) 'Direct numerical simulation of a transitional rectangular jet', *International Journal of Heat and Fluid Flow*, Vol. 23, No. 5, pp. 547-553.

109. Holdo, A.E. and Simpson, B.A.F. (2002) 'Simulations of high-aspect-ratio jets', *International Journal for Numerical Methods in Fluids*, Vol. 39, No. 4, pp. 343-359.

110. Wilson, W.M. and Imber, R.D. (2003) 'CFD analyses of compact, high aspect ratio ejectors', *Proceedings of the ASME Fluids Engineering Division Summer Meeting*, Vol. 1, pp. 7-13.

111. Jiang, X. and Luo, K.H. (2001) 'Direct numerical simulation of transitional noncircular buoyant reactive jets', *Theoretical and Computational Fluid Dynamics*, Vol. 15, No. 3, pp. 183-198.

112. Reddy, D.R., Steffen, C.J.Jr. and Zaman, K.B.M.Q. (1999) 'Computation of three-dimensional compressible flow from a rectangular nozzle with delta tabs', *Journal of Engineering for Gas Turbines and Power*, Vol. 121, No. 2, pp. 235-242.

113. Wilson, R.V. and Demuren, A.O. (1998) 'Numerical simulation of turbulent jets with rectangular cross-section', *Journal of Fluids Engineering*, Vol. 120, No. 2, pp. 285-290.

114. Grinstein, F.F. (1998) 'Vortex dynamics and transition to turbulence in low aspect-ratio rectangular free jets', *American Society of Mechanical Engineers, Fluids Engineering Division (Publication) FED*, FEDSM98-5307.

115. Reddy, D.R., Steffen, C.J.Jr. and Zaman, K.B.M.Q. (1998) 'Computation of 3-D compressible flow from a rectangular nozzle with delta tabs', *American Society of Mechanical Engineers, Proceedings of the 1997 International Gas Turbine & Aeroengine Congress & Exposition*, Paper 97-GT-257.

116. Zaman, K.B.M.Q., Steffen, C.J. and Reddy, D.R. (1997) 'Entrainment and spreading Characteristics of jets from asymmetric nozzles', *AIAA-97-1878*, Vol. 99, No. 2, pp. 1-12.

117. Wilson, R.V. and Demuren, A.O. (1996) 'Numerical simulation of turbulent jets with rectangular cross-section', *American Society of Mechanical Engineers, Fluids Engineering Division (Publication) FED*, Vol. 238, No. 3, pp. 121-127.

118. Grinstein, F.F. and DeVore, C.R. (1996) 'Dynamics of coherent structures and transition to turbulence in free square jets', *Physics of Fluids*, Vol. 8, No. 5, pp. 1237-1251.

119. Grinstein, F.F., Gutmark, E. and Parr, T. (1995) 'Near field dynamics of subsonic free square jets. A computational and experimental study', *Physics of Fluids*, Vol. 7, No. 6, pp. 1483-1497.

120. Grinstein, F.F. and Kailasanath, K. (1995) 'Three-dimensional numerical simulations of unsteady reactive square jets', *Combustion and Flame*, Vol. 100, No. 1-2, pp. 2-10.

121. Teshima, K. (1989) 'Three-dimensional structure of a supersonic free jet issuing from a rectangular orifice', *Collection of Technical Papers ISCFD NAGOYA*, pp. 1144-1149.

122. Quinn, W.R. and Militzer, J. (1988) 'Experimental and numerical study of a turbulent free square jet', *Physics of Fluids*, Vol. 31, No. 5, pp. 1017-1025.

123. McGuirk, J.J. and Rodi, W. (1979) 'The calculation of three-dimensional turbulent free jets', *Turbulent Shear Flows. I, University Park, PA, USA*, pp. 71-83.

124. Abdel-Hameed, H. and Bellan, J. (2002) 'Direct numerical simulations of two-phase laminar jet flows with different cross-section injection geometries', *Physics of Fluids*, Vol. 14, No. 10, pp. 3655-3674.

125. Imine, B., Abidat, M., Imine, O., Gazzah, H. and Gokalp, I. (2004) 'Study of turbulent variable density jets with different asymmetric geometries', *Proceedings of the 7th Biennial Conference on Engineering Systems Design and Analysis*, Vol. 1, pp. 505-511.

126. Gutmark, E.J. and Grinstein, F.F. (1999) 'Flow control with noncircular jets', *Annual Review of Fluid Mechanics*, Vol. 31, pp. 239-272.

127. Zaman, K.B.M.Q., Wang, F.Y., Georgiadis, N.J. Noise, turbulence, and thrust of subsonic freejets from lobed nozzles. *AIAA Journal*, v 41, n 3, 2003, pp. 398-407.

128. Hu, H., Saga, T., Kobayashi, T. and Taniguchi, N. (2001) 'A study on a lobed jet mixing flow by using stereoscopic particle image velocimetry technique', *Physics of Fluids*, Vol. 13, pp.3425-3441.

129. Ahuja, K.K. and Brown, W.H. (1989) 'Shear flow control by mechanical tabs', *AIAA* paper, No. 89-0994.

130. Zaman, K.B.M.Q., Reeder, M.F. and Samimy, M. (1994) 'Control of an axisymmetric jet using vortex generators', *Physics of Fluids*, Vol. 6, No. 2, pp. 778-793.

131. Zaman, K.B.M.Q. (1994) 'Effect of 'delta tabs' on mixing and axis switching in jets from asymmetric nozzles', *NASA Technical Memorandum*, No. 106450, pp. 1-20.

132. Zaman, K.B.M.Q., Samimy, M. and Reeder, M.F. (1991) 'Effect of tabs on the evolution of an axisymmetric jet', *NASA Technical Memorandum*, No. 104472, pp. 1-14.

133. Zaman, K.B.M.Q. and Raman, G. (1997) 'Reversal in spreading of a tabbed circular jet under controlled excitation', *Physics of Fluids*, Vol. 9, No. 12, pp. 3733-3741.

134. Husain, H.S. and Hussain. F. (1999) 'The Elliptic Whistler Jet', *Journal of Fluid Mechanics*, Vol. 397, pp. 23-44.

135. Lee, S.K., Lanspeary, P.V., Nathan, G.J., Kelso, R.M. and Mi, J. (2001) 'Preliminary study of partially confined oscillating triangular jets', *Proceedings of the 14th Australian Fluid Mechanics Conference*, Adelaide University, Australia.

136. Mi, J., Nathan, G.J. and Luxton, R.E. (2001) 'Mixing characteristics of a flapping jet from a self-exciting nozzle', *Flow, Turbulence and Combustion*, Vol. 67, pp. 1-23.

137. New, T.H., Tan, K.S. and Tsai, H.M. (2007) 'Effects of noncircular collars on an axisymmetric jet', *Physics of Fluids*, Vol. 19, No. 8, pp. 084104/1-14.

138. Launder, B.E. and Spalding, D.B. (1974) 'The numerical computation of turbulent flows', *Computer Methods in Applied Mechanics and Engineering*, Vol. 3, No. 2, pp.269-289.

139. Yakhot, V. and Orszag, S.A. (1986) 'Renormalization group analysis of turbulence: I. Basic theory', *Journal of Scientific Computing*, Vol. 1, No. 1, pp.3-51.

140. Choudhury, D. (1993) 'Introduction to the renormalization group method and turbulence modeling', *Fluent Inc. Technical Memorandum TM-107*, Lebanon NH 03766, USA.

141. Menter, F.R., Kuntz, M. and Langtry, R. (2003) 'Ten years of industrial experience with the SST turbulence model', *4th International Symposium on Turbulence, Heat and Mass Transfer*, pp.625-632.

142. Daly, B.J. and Harlow, F.H. (1970) 'Transport equations in turbulence', *Physics of Fluids*, Vol. 13, No. 11, pp.2634-2649.

143. Lien, F.S. and Leschziner, M.A. (1994) 'Assessment of turbulent transport models including non-linear RNG eddy-viscosity formulation and second-moment closure for flow over a backward-facing step', *Computers and Fluids*, Vol. 23, No. 8, pp.983-1004.

144. Gibson, M.M. and Launder, B.E. (1978) 'Ground effects on pressure fluctuations in the atmospheric boundary layer', *Journal of Fluid Mechanics*, Vol. 86, pp.491-511.

145. Fu, S., Launder, B.E. and Leschziner, M.A. (1987) 'Modeling strongly swirling recirculating jet flow with Reynolds-stress transport closures', *Proceedings of the 6th Symposium on Turbulent Shear Flows*, Toulouse, France, pp.17.6.1-17.6.6.

146. Launder, B.E. (1989) 'Second-moment closure and its use in modeling turbulent industrial flows', *International Journal for Numerical Methods in Fluids*, Vol. 9, No. 8, pp.963-985.

147. Launder, B.E. (1989) 'Second-moment closure: Present and future?', *International Journal of Heat and Fluid Flow*, Vol. 10, No. 4, pp.282-300.

148. Kim, S.E. and Choudhury, D. (1995) 'Near-wall treatment using wall functions sensitized to pressure gradient', *ASME, Fluids Engineering Division (FED), Separated and Complex Flows*, Vol. 217, pp.273-280.

149. Issa, R.I. (1986) 'Solution of the implicitly discretized fluid flow equations by operator-splitting', *Journal of Computational Physics*, Vol. 62, No. 1, pp.40-65.

150. Leonard, B.P. (1979) 'A stable and accurate convective modeling procedure based on quadratic upstream interpolation', *Computer Methods in Applied Mechanics and Engineering*, Vol. 19, No. 1, pp.59-98.

151. Lin, C.A. and Tsai, J.H. (1992) 'Computations of strongly swirling flows with second-moment closures', *16th National Conference on Theoretical and Applied Mechanics*, Keelung, Taiwan, pp.127-134.

152. Mahmud, T., Sangha, S.K., Costa, M. and Santos, A. (2007) 'Experimental and computational study of a lifted, non-premixed turbulent free jet flame', *Fuel*, Vol. 86, No. 5-6, pp. 793-806.

153. Patankar, S.V. (1980) *Numerical Heat Transfer and Fluid Flow*, Washington, USA: Hemisphere.